12-2019

Direct Numerical Simulations of Flame Propagation in Stratified Mixtures at Auto-ignitive Conditions Using Accelerated Computing

Swapnil Desai
University of Tennessee, sdesai9@vols.utk.edu

To the Graduate Council:

I am submitting herewith a dissertation written by Swapnil Desai entitled "Direct Numerical Simulations of Flame Propagation in Stratified Mixtures at Auto-ignitive Conditions Using Accelerated Computing." I have examined the final electronic copy of this dissertation for form and content and recommend that it be accepted in partial fulfillment of the requirements for the degree of Doctor of Philosophy, with a major in Energy Science and Engineering.

Ramanan Sankaran, Major Professor

We have read this dissertation and recommend its acceptance:

Derek Splitter, Charles Finney, Zhili Zhang

Accepted for the Council:

Dixie L. Thompson

Vice Provost and Dean of the Graduate School

(Original signatures are on file with official student records.)

Direct Numerical Simulations of Flame Propagation in Stratified Mixtures at Auto-ignitive Conditions Using Accelerated Computing

A Dissertation Presented for the

Doctor of Philosophy

Degree

The University of Tennessee, Knoxville

Swapnil Sanjaybhai Desai

December 2019

To my parents, Vasantmala and Sanjay, and my wife, Roshni, for their unconditional love, support and motivation. This endeavor could not have been possible without you guys!

Acknowledgments

I am greatly indebted to my advisor Dr. Ramanan Sankaran for his valuable guidance and supervision during my doctoral study. His involvement and enthusiasm in research has been a great motivation to me. During these years, he has always been reachable and readily available for any assistance, however trivial or time consuming it might have been. He is one of the main reasons that my doctoral study has been so enjoyable.

That my time at the University of Tennessee has been good is due in part to the excellent resources at UT and the nice ambiance of the Bredesen Center. I am very grateful to our collaborators at King Abdullah University of Science and Technology (KAUST), especially, Prof. Hong G. Im, Dr. Francisco E. Hernández Pérez, Dr. Minh Bau Luong, Mr. Wonsik Song and Ms. Yu Jeong Kim for a fruitful collaboration and as co-authors. A special thanks to Mr. Marvin Joshi, a junior in the Electrical and Computer Engineering department at the University of Tennessee for his assistance in the development of an isotropic turbulence generator.

I am grateful to Dr. Kalyana Gottiparthi, Dr. Vimal Ramanuj and Dr. Wenjun Ge in my research group for their cheerful company and hearty discussions. My thanks also go to the members of my thesis committee — Dr. Derek Splitter, Dr. Zhili Zhang and Dr. Charles Finney for providing many valuable comments that improved the contents of this dissertation. This work was financially supported by the following agencies:

1. Bredesen Center's Energy Science and Engineering Fellowship

2. Clean Combustion Research Center (CCRC), King Abdullah University of Science and Technology (KAUST)

3. Joint Institute for Computational Sciences (JICS), an Institute of the University of Tennessee, Knoxville and Oak Ridge National Laboratory (ORNL)

4. The Oak Ridge Leadership Computing Facility (OLCF) and the Compute Data and Environment for Science (CADES) at ORNL, supported by the Office of Science of the U.S. Department of Energy under Contract No. DE-AC05-00OR22725

5. U.S. Department of Energy (DOE) Office of Energy Efficiency and Renewable Energy (EERE) Vehicle Technologies Office (VTO)

Abstract

Direct numerical simulation (DNS) of auto-ignition under turbulent conditions has played a very important role in improving the fundamental understanding and advancement of combustion technologies for practical applications. However, very little is known of the nature of combustion in a reactive fuel/air mixture that is conducive to both spontaneous ignition and premixed deflagration. As such, characterizing the precise nature of combustion and the relevant propagation speed remains a challenge. This study attempts to address these questions by performing fully resolved numerical simulations of preheated fuel/air mixtures at elevated pressures using a newly developed DNS code called KAUST Adaptive Reactive Flows Solver (KARFS). Unlike a periodic box setup that has been used in most of the previous DNS studies, an inflow-outflow configuration representing a statistically stationary reaction front has been employed to understand the unsteady flame dynamics at auto-ignitive conditions.

The first part of the dissertation is devoted to a discussion on parametric mapping of propagation speeds of auto-ignitive dimethyl-ether/air as well as dimethyl-ether/methane/air mixtures at elevated pressures under the influence of monochromatic thermal and composition/reactivity stratification using a one-dimensional, statistically stationary configuration. Thereafter, the implementation and effectiveness of Weighted Essentially Non-Oscillatory (WENO) schemes in performing DNS of turbulent reacting flows is demonstrated with various non-trivial model problems. In addition, the scalability and performance portability of KARFS is presented on heterogeneous (Central Processing Unit, CPU + Graphics Processing Unit, GPU) system architectures. Finally, as a more extensive parametric quantification of the effects of thermal and composition stratification on turbulent flame

propagation, results from DNS of a turbulent premixed flame in an auto-ignitive dimethyl-ether/air mixture conducted at elevated pressure are presented and discussed. The outcomes of this dissertation are expected to provide a fundamental understanding of the combustion mode transition and relevant propagation speeds in modern engines utilizing mixed-mode combustion.

Table of Contents

List of Tables

List of Figures

Chapter 1

Introduction

Currently, more than a billion vehicles are in use across the world, around 95% of which are equipped with either gasoline or diesel internal combustion (IC) engines. Even by 2050, the percentage share of such vehicles is expected to remain more than 70% [2]. These engines burn vast quantities of fossil fuels. Indeed, 76% of 86 million barrels of crude oil that we consume every day are used in IC engines [3]. These consumption needs are certainly going to increase as even more economic development takes place worldwide in the near future. Another issue associated with the massive usage of fossil fuels is that of the accompanying emissions of pollutants, including nitrogen oxides (NO_x) and particulates (soot), in addition to the production of carbon dioxide (CO_2). Pollutant emissions have raised serious environmental and health concerns. For example, the world's annual production of 37 billion tons of CO_2 contributes to green house gases (GHG), which could lead to climate change with unpredictable and irreversible consequences [2]. This has led to more stringent emissions regulations that are continually being tightened further.

In response, various advanced combustion concepts have emerged which hold the promise of simultaneously improving engine efficiency, reducing harmful emissions of NO_x and soot while allowing utilization of renewable fuels. The combustion concepts that are being pursued are quite different from the traditional spark ignition (SI) or compression ignition (CI) based engines. These combustion strategies can be generally lumped into the category of dilute, premixed compression ignition (PCI) combustion.

1.1 Premixed compression ignition

Ignition and combustion in PCI occur at conditions that are on the fringes of the traditional operating regimes of IC engines. Due to highly dilute operation in PCI, combustion temperatures are lowered. As a result, the high activation energy required for NO_x formation is not reached. Heat-transfer losses are also found to be reduced due to lower combustion temperatures, and an efficiency gain of up to 10 % has been demonstrated in heavy-duty engines [4]. The high level of pre-combustion mixing associated with these combustion modes also reduces the rich regions and avoids soot formation.

Over the last decade, various experimental and numerical studies [5–13] have demonstrated that PCI combustion strategies often involve mixed modes of combustion due to the presense of a highly reactive premixed charge. In such cases, flames and auto-ignition processes are simultaneously contributing to the overall process of combustion and heat release. There is currently only a limited fundamental understanding of the nature of combustion in an auto-ignitive fuel/air mixture that is conducive to both spontaneous ignition and diffusion driven flame propagation (deflagration) such as that observed in PCI. The speed at which turbulent flames propagate is a fundamental parameter in many combustion applications, such as IC engines and gas turbines. Flame speeds influence knocking events in IC engines and play an important role in their performance and emissions. In SI engines, a lower combustion rate increases the combustion duration and moves it away from being a constant-volume combustion process, thereby reducing the thermal efficiency. On the other hand, a higher combustion rate allows a near constant-volume combustion process, at a risk of engine knock, at high load conditions. Similarly, a critical parameter in CI engines is the lift-off length (LOL) which affects the mixing and pollutant formation processes [14]. The prediction of the LOL depends upon the underlying method of flame stabilization i.e. auto-ignition or flame propagation. Since PCI concepts combine the principles of SI and CI engines, an accurate prediction of front propagation speeds at PCI engine-relevant conditions is of fundamental importance.

Traditionally, the deflagrative flame speed is evaluated as an eigenvalue for a freely propagating laminar flame in an infinite domain [15], wherein the mixture is presumed to be

non-reactive at far upstream. The flame speed is an inherent property of the mixture state and is independent of the domain size or the location of the flame. If the upstream mixture is not reactive, diffusion of heat and radicals from the reaction layer to the upstream preheat layer is necessary for sustained propagation. However, if the upstream mixture is nearly at auto-igniting conditions, as often encountered in IC engines, the front speed is no longer an eigenvalue and depends on various system parameters, such as the flame position relative to the end wall. In this case, the ignition delay of the mixture coupled with the residence time ahead of the front determines the propagation speed of the flame. As such, the dependence of propagation speed on the evolution of a mixture's state during its residence time within the system is critical in describing the mixed mode combustion characteristics. This sensitivity of the laminar flame solutions to the domain size has been observed in a recent study [16], but the subject has not been extensively investigated.

In a pioneering study, Zel'dovich [17] identified the regimes of a reaction front propagating through a non-uniform reactive mixture. Of particular relevance to modern IC engines utilizing mixed modes of combustion are: (i) spontaneous propagation, in which gradients of ignition delay time drive the propagation and (ii) premixed deflagration, in which conduction and diffusion play a major role in propagation. Subsequently, a number of studies [8, 18–21] attempted to provide a practical and meticulous way to identify the various front propagation regimes. Identifying the effects of these two regimes on the propagation speeds of the emerging fronts is of fundamental interest for high-fidelity modeling of modern IC engines utilizing mixed-mode combustion.

Fundamental numerical simulations that can enunciate the nature and characteristics of flame propagation in stratified reactive mixtures are key to improving and applying the appropriate combustion models in device scale simulations. Considering the importance and needs of PCI engine modeling, the objectives of the present numerical study are two folds. First, an attempt is made to accurately predict the propagation speeds of an auto-ignitive fuel/air mixture that is conducive to both spontaneous ignition and diffusion driven flame propagation, under conditions relevant to PCI concepts. This will help identify the parameters which have the strongest influence on propagation speeds and how they may be adjusted to achieve the desired objectives. Secondly, it can be used to provide better

sub-models for large scale simulations to accurately predict the front propagation speed and the nature of combustion.

1.2 Direct numerical simulation and the era of accelerated computing

Direct numerical simulation (DNS) of turbulent reacting flows is a first principle approach for turbulent combustion simulations that does not require closure models for turbulence physics and therefore independent of the statistical and numerical assumptions that underlie such closure models [22]. DNS of reacting flows in canonical flow configurations such as triply periodic cube domains and fully three-dimensional spatially developing jet configurations have been used to study turbulence-combustion interaction in reactive mixtures [19, 23]. Since DNS resolves all of the relevant flow scales up to the smallest dissipative scales, it becomes prohibitively expensive to simulate large scale flow motion up to device scales. However, smaller canonical geometries have been within the reach of DNS for several years now. Newer developments in high performance computing (HPC) have allowed an increase in the range of length scales simulated, providing more realism in the turbulence physics, along with simultaneously increasing the chemical complexity, allowing the simulation of fuels and intermediates that are better surrogates of transportation fuels.

One of the primary objectives of DNS is to capture the turbulent flow physics as accurately as possible without introducing numerical distortion that would cause the turbulence energy cascade to be incorrect. Low dissipation and higher-order accuracy in time have become essential for the numerical methods used in the DNS. Higher order centered finite difference schemes, such as the eighth order accurate scheme [24] along with higher order accurate Runge–Kutta time integration schemes [25] have been very successful in enabling DNS with near-spectral like solution accuracy while also allowing efficient and affordable computations of large problems. Since the central difference scheme lacks the numerical dissipation needed to ensure stability, it is also customary to use a filter operator, such as the tenth order accurate explicit filter by Kennedy and Carpenter [24]. Such a

combination of higher order accurate central difference schemes along with explicit filtering has proven to be well suited and sufficient for DNS of low speed turbulent combustion when the combustion fronts are sufficiently resolved on the numerical grid. Therefore, direct numerical simulations (DNS) of reaction fronts relevant to PCI engine conditions are performed here.

Success in the general application of Computational Fluid Dynamics (CFD) and affiliated techniques such as DNS is largely dependent on achieving an optimal balance between multi-scale fidelity, multi-physics detail and the overall computational cost. In that regard, recent advances in computational architectures offer both potential and challenges. Dramatic speed-ups can be potentially achieved across platforms using state-of-the-art multi-core central processing units (CPUs) and graphics processing units (GPUs). The challenge, however, is actually attaining this potential through development of new parallel programming models that can be used to efficiently port various algorithms and the related code kernels to these new heterogeneous architectures. A major challenge in utilizing heterogeneous resources is the diversity of devices on different machines, which provide widely varying performance characteristics. A program or algorithm optimized for one architecture may not run as well on the next generation of processors or on a device from a different vendor. A program or algorithm optimized for GPU execution is often very different from one optimized for CPU execution. The relative performance of CPUs and GPUs also varies between machines. On one machine, a specific portion of a computation may run best on the CPU, while on another machine it may run best on the GPU. In some cases, it is best to balance the workload between the CPU and the GPU; in other cases, it may be best to execute an algorithm on a device where it runs more slowly but closer to where its output is needed, in order to avoid expensive data transfer operations. It is not uncommon for large application codes to have several different implementations, with each one optimized for a different architecture. This software development approach leads to a code maintainability issue: every new change to the code needs to be implemented in all versions of the code. Performance portability of a single code base, therefore, has become a critical issue: parallel code needs to execute correctly and remain performant on machines with different architectures, operating systems, and software libraries.

Several groups have published their efforts for accelerating the flow solvers used for multi-component reacting flow calculations using GPUs. The most common approach is to select the most time consuming and compute-intensive kernels and offload them to the GPUs for accelerated solution [26]. In the case of combustion solvers, the chemical reaction kinetics was the predominant kernel that was offloaded to the GPUs. Spafford and co-workers [27] were the first to use this approach to offload the chemical kinetics evaluation to a GPU using the CUDA programming model and thereby accelerate a DNS solver for turbulent combustion. Their approach was to use grid-level parallelism for acceleration by computing the reaction kinetics across the large number of grid points in parallel on the GPU. In contrast, Shi et al. [28], utilized the parallelism available in the reaction network itself to simultaneously calculate all the reaction rates for a single kinetic system. They observed a considerable speedup for large chemical reaction mechanisms (>1000 species), but could not obtain any acceleration for smaller mechanisms (<100 species). The performance of implicit integration schemes for stiff chemical kinetics against the speedups obtained for explicit integration has also been measured by Stone et al. [29]. More recently, Niemeyer et al. [30] used fully explicit and stabilized explicit methods for accelerating chemical kinetics with low to moderate levels of stiffness. In these studies, it was found that the potential for acceleration of chemical kinetics through GPUs is large when explicit integration is feasible. But in the presence of stiffness, the performance on GPUs was highly susceptible to thread divergence due to varying levels of stiffness across the multiple states.

The DNS solver — KARFS (KAUST Adaptive Reacting Flows Solver) used in the present study was first introduced in [31], showcasing its application in multi-dimensional turbulent reacting flow simulations. KARFS is a modern DNS code developed in C++ using modern parallel programming patterns, distributed memory parallelism through message passing interface (MPI) and portable on-node parallelism with the Kokkos (Greek: granule) C++ programming model [32, 33]. KARFS has performance-portable capabilities for multi- and many-core heterogeneous platforms, which is instrumental to meet emerging demands of exa-scale computing machines. The employed Kokkos framework allows KARFS to straightforwardly utilize the same source code on CPUs and GPUs while maintaining performance comparable to the code that is optimally tuned to either processing unit.

Standard C++ programming practices have been used for both on- and off-node parallelism. This has been the main motivation for choosing the Kokkos programming model, in which all kernel launches on a target device and all memory copies between memory spaces are asynchronous by default. With further development of Kokkos to allow multiple stream/task parallelism, it will be possible to schedule multiple streams of tasks to hide latencies. It is expected to be the most portable programming model for future HPC application. Current choices for asynchronous execution or data management requires vendor specific extensions to the standard programming languages. Furthermore, they require compiler extensions through Pragmas that are not widely supported by all open source compilers. Other available runtime systems cannot currently inter-operate with Kokkos-type programming abstractions. The future versions of KARFS will track the task parallelism model being developed in Kokkos.

1.3 Dimethyl-ether as an alternative fuel

The two major fuels that had been developed and widely used along with the development of the IC engines and the automotive industries over the past century are gasoline and diesel. The combustion of gasoline fuel typically undergoes flame propagation after an initial spark event igniting the homogeneous air/fuel mixture in SI engines, while the combustion of diesel fuel is driven by the auto-ignition of the fuel exposed to high-temperature gas, heated by compression in CI engines. Despite the long history of a steady supply chain and the determined position of gasoline and diesel as conventional automotive fuels in the market, the search for alternative fuels gradually started to emerge in the 1980s [34]. Alternative fuels can be defined as those other than conventional gasoline and diesel fuels, covering a wide variety in terms of final forms and manufacturing sources. For example, ethanol fuel is considered an alternative for SI engines, regardless of its original source from either conventional crude oil or any renewable biomass. The alternative fuels defined by the Energy Policy Act (EPAct) also cover a vast amount of non-conventional fuels, including alcohols such as ethanol (including blends with gasoline over 85%); natural gas and liquefied fuels domestically derived from natural gas; liquefied petroleum gas (LPG); coal-derived liquid

fuels (coal to liquid); hydrogen (H_2); biodiesel (B100); fuels, other than alcohol, derived from biological materials; and fuel that is markedly non-petroleum that yields substantial energy security and environmental benefits. The significance of using alternative fuels can be attributed to the following aspects: (1) pursuing energy sustainability through the extended usage of those alternative fuels derived from renewable energy sources and mitigating the concerns of limited fossil fuel energy; (2) improving engine efficiency and engine-out emissions with the aid of superior physical or chemical properties of alternative fuels compared to those of conventional fuels; (3) relieving the unbalanced usage of conventional petroleum-based fossil fuels. At the same time, some of the common critical considerations for alternative fuels for both CI and SI engines are:

- Combustion properties (chemical properties, such as octane and cetane number);
- Physical properties (spray or mixture formation for combustion, and engine operability over a wide range of temperatures and load conditions);
- Lower heating value (LHV).
- Compatibility (including approval by engine and vehicle manufacturers and costs)
- Manufacturing cost and infrastructures

The combustion properties directly determine whether the given alternative fuels are suitable for engine operation. The physical properties are also important, as they determine the formation of combustible mixture. The octane number determines the knock resistance of a given fuel, and it is a decisive factor that determines whether the given alternative fuel is applicable to SI combustion or not. On the other hand, the cetane number strongly determines the ignition quality of the fuel, and it is a decisive factor for whether a given fuel is applicable to CI engine application. The LHV determines the effectiveness of the fuel as an energy carrier. The comparable level of LHV to conventional fuels is preferred, otherwise penalties in fuel consumption may become problematic. Material compatibility with current engine hardware of fuel-suppply infrastructure is important for the penetration of alternative fuels into the market. Otherwise, a great amount of additional cost would need to be expanded for hardware modifications.

Dimethyl-ether (DME) has been used for decades as an aerosol propellant in the personal care industry. It has gained attention as a clean alternative fuel to LPG, diesel and gasoline, with physical properties very similar to those of LPG [35]. It offers remarkable potential not only as an automotive fuel, but also for electric power generation, and in domestic applications such as heating and cooking. DME, which also is expected to be produced from biomass resources in the future, is attractive as a solution for energy sustainability and environmental problems. DME can be derived from many sources, including fossil fuels (natural gas and coal) and renewable materials (biomass, waste and agricultural products). Two methods exist for producing DME as a fuel in large quantity with relatively low cost. The methods include (1) a two-step process (indirect method) of adding a dehydration step to the latter part of industrial methanol processing, and (2) a one-step process (direct method) of synthesizing DME directly from synthesis gas (H_2, CO). Some recent developments in the synthesis methods of DME, conventional processes and innovative technologies in reactor design, and employed catalysts have allowed the efficient production of DME [36]. Overall, the production amount is small, at about 150,000 tons worldwide [35]. Although the well-to-tank (WTT) efficiency for DME is low, due to the remotely located gas sites and wasted heat from fuel production, the overall well-to-wheel (WTW) efficiency is generally comparable to that of LPG and CNG fueled vehicles, ranging around 18% – 19% (while that for diesel fuel is 25.7%) [36]. The WTW CO_2 emissions (including all CO_2 from production to combustion) for fossil fuel derived DME are also comparable to those of diesel and CNG fuel, while the DME derived from bio-feedstock is nearly 1/5 that of petroleum-based or conventional diesel fuel.

DME is in gas phase at standard temperature and pressure. However, it changes to liquid when subjected to modest pressure (> 6 MPa) and/or cooling. This easy liquefaction makes DME easy to transport and store. This and other properties, including high oxygen content, and lack of sulfur or other noxious compounds, make DME a versatile and promising solution in the mixture of clean renewable and low-carbon fuels under consideration worldwide. The cetane number of DME is higher than that of diesel, which makes it a promising alternative fuel for CI engines. The spray structure of DME has also been categorized with respect to three different ambient pressure conditions, namely below saturated vapor pressure of DME

(or at atmospheric condition), beyond critical pressure of DME, and finally, in between these pressure ranges [36].

The spray development characteristics of DME and diesel was investigated by Yu et al. [37]. The spray was injected into atmospheric conditions with an injection pressure of 55 MPa for both fuels. It was found that the DME vapor appeared prior to a gushing liquid phase. Afterward, DME rapidly spread in both the longitudinal and axial directions, breaking up into small droplets, while the diesel spray maintained a narrow edge of the spray boundary, with longer elapsed time for break-up. The superior break-up process along with the fast evaporation of the fuel resulted in enhanced atomization. The results of spray velocity and the droplet Sauter Mean Diameter (SMD) distribution measurements through phase Doppler particle analyzer (PDPA) supported the better atomization observed for DME [38]. But, the low LHV of DME ($\approx$ 27.6 MJ/kg) yields performance penalties and greater fuel consumption on a mass basis, compared to that of conventional diesel ($\approx$ 42.5 MJ/kg). Moreover, low lubrication of DME [37] may result in malfunction of sophisticated fuel injection equipment (FIE) such as common-rail direct injection system (CRDI) in diesel engines. Nevertheless, DME has several advantages over diesel in terms pollutant formation. The potential of smokeless combustion with DME fuel was demonstrated in the early 1990s [39]. The soot formed in DME combustion is near zero, due to its oxygen content of 35% and lack of carbon-–carbon (C–C) bonds [40]. Even though from a physical property point of view, its superior evaporation characteristics can also enhance mixture formation with the surrounding air and contribute to smoke reduction (similar to that for LPG), from a chemical perspective, the absence of C–C bond has been regarded as the dominant reason for low smoke emission. This implies that DME-fueled engines can virtually eliminate particulate emissions and potentially negate the need for costly diesel particulate filters. The shorter ignition delay of DME, which contributed to a lesser amount of pre-mixed burn phase, was one of the reasons for lowered NO_x emission with DME, compared to that with diesel [41]. The higher specific heat capacity of the DME, in addition to the slower rate of energy release due to the lower LHV than that of diesel, can contribute to the lowered peak adiabatic flame temperature and lesser amount of NO_x formation compared to that of diesel. It has a cetane

number of 55, larger than the cetane number for diesel (between 44 and 53) which indicates its superior autoignition properties.

Yamada et al. [42] elucidated the chemical mechanism of DME oxidation by using an externally motored single-cylinder piston engine. It was shown using in situ laser-induced fluorescence that formaldehyde forms rapidly during the first-stage ignition process, corresponding to cool flame ignition, and subsequently disappears during the second-stage of thermal ignition. This is consistent with the detailed chemical mechanism of DME oxidation by Curran et al. [43] and Zhao et al. [44]. Yamada et al. [45] also experimentally investigated the transition from cool flame to thermal explosion in DME-fired HCCI engines. They concluded that the mechanism during this transition process can be qualitatively explained using the thermal explosion theory, whereby the rate-determining reaction is H_2O_2 decomposition, assuming that the heat release in this period is caused by partial oxidation of fuel and intermediate species. Moreover, they clearly showed that DME autoignition can be partitioned into three distinct ignition stages, each attributed to a different chemical reaction pathway. The first stage corresponds to the conventional cool ignition (negative-temperature coefficient regime) controlled by DME fuel-specific chemistry. The key-intermediate in this low-temperature ignition process was found to be methoxymethyl-peroxy ($CH_3OCH_2O_2$) [42, 44]. The second stage is controlled by H_2O_2 thermal dissociation, and the final stage corresponds to high temperature ignition of hydrogen controlled by the well-known branching-termination reaction pair:

$$H + O_2 \rightarrow O + OH \tag{1.1}$$

$$H + O_2 + M \rightarrow HO_2 + M \tag{1.2}$$

The three-staged DME auto-ignition has also been experimentally observed by Oshibe et al. [46]. Since, negative temperature coefficient (NTC) chemistry is of significant importance in IC engine combustion, it is critical to investigate flame dynamics in the presence of NTC chemistry. DME also happens to be one of the simplest fuel molecules that exhibits multi-stage ignition and NTC behavior. A non-stiff, reduced chemical model for DME

oxidation [23] consisting of 30 species with 175 reactions and an additional 9 species identified as global quasi-steady state species has also been systematically developed from a detailed DME model [44]. Previous studies [47–49] have demonstrated that the detailed DME model [44] is able to accurately reproduce the flame speeds and ignition delay times of DME/air, CH_4/air and DME/CH_4/air mixtures for a wide range of operating conditions. As such, it is particularly well suited for performing DNS studies due to its efficient application without causing a heavy demand in compute time.

1.4 Challenges to simulate premixed compression ignition

Despite their advantages, PCI concepts face challenges of the difficult combustion control and narrow operating ranges [11]. The presence of multiple combustion modes in PCI engines presents additional challenges in controlling the pressure rise rate and ignition timing, particularly under high-load conditions. Several strategies have been proposed to mitigate these problems and gain more control over the ignition process. Two of the most promising ones are temperature and mixture stratification. Thermal stratification has the effect of spreading out the heat release by sequentially igniting zones with decreasing temperature, if combustion phasing is kept constant. Mixture stratification also has the effect of spreading out the heat release while improving combustion efficiency at low loads by producing higher equivalence ratios locally that burn hotter and more completely. Hence, performing DNS of PCI concepts under stratified conditions that are representative of real operating conditions is of paramount importance.

Meanwhile, the spatial profile of a propagating reaction front is determined by the transport rate of heat and radicals between the reaction zone and the upstream mixture. The thickness of a typical transport-driven flame front is determined by the molecular or turbulent diffusivity, in the case of laminar and turbulent flames, respectively. However, a spontaneous ignition front, often encountered in PCI, is not limited by the transport rates. The thickness of a spontaneous ignition front is determined primarily by the gradients in

reactivity of the upstream mixture, and the effects of transport rate are secondary. When a spontaneous ignition front encounters an adverse gradient in reactivity, it can turn into a sharp contact discontinuity between the unreacted and reacted mixtures, with steep gradients in density, temperature and composition. Such a contact discontinuity is distinct from a detonation, since there is no large pressure jump between the unburned and burned mixtures while propagation remains subsonic. It can eventually develop into a detonation wherein combustion is initiated suddenly and propagates extremely rapidly, giving rise to a shock wave. The presence of such discontinuities may render the central difference schemes that are commonly used in DNS solvers cost prohibitive due to very fine grid resolution requirements or ineffective in capturing the underlying physics altogether. As such, the relevance of shock-capturing schemes as an essential ingredient of the DNS solver is emphasized.

Furthermore, turbulent premixed flames play a major role in modern combustion devices such as internal combustion engines and gas turbine combustors. The main effect of turbulence on combustion is to increase the combustion rate. Experimentalists have known for a long time that changing the turbulence level before starting combustion in a vessel may change the time needed for total combustion and, accordingly the turbulent flame speed. As such, an accurate prediction of turbulent flame propagation speeds under PCI engine relevant conditions is required for a better physical understanding and to develop engineering models for design and optimization.

Majority of combustion in PCI concepts occurs via compression ignition at constant pressure. In a periodic domain, pressure continuously rises as the simulation progresses. As such, the effects of compression heating on the propagation speed of emerging reaction fronts can not be isolated. On the other hand, an inflow-outflow configuration, which has been adopted in the present study, can be kept at constant pressure and statistically stationary. This, in turn, allows simulations to be run continuously until substantial flame statistics are obtained. In the following subsections, the aforementioned factors affecting PCI combustion and related aspects that are yet to be answered are briefly discussed.

1.4.1 Thermal stratification

Some degree of temperature stratification naturally occurs in engines due to heat loss at cylinder walls. This has also been experimentally demonstrated by previous studies including the one by Dronniou et al. [50]. Temperature maps obtained along the horizontal mid-plane as well as the vertical plane of the engine cylinder showed that pockets of stratified temperature fields are formed towards the end of compression stroke as well as during the initial stages of expansion stroke. Based on the observations, the authors reported a characteristic spatial scale of $5 - 11$ mm which is similar to the top dead center (TDC) clearance of 8 mm. They also indicated that the spatial distribution of thermal non-uniformities showed no consistent pattern from cycle to cycle. Rather, the distributions were random, suggesting a turbulent nature to the flow structures producing them. Apart from the natural occuring thermal stratification, there may be additional thermal stratification if exhaust gas recirculation (EGR) is employed to dilute and preheat the fuel/air mixture. This is due to incomplete mixing between the hot EGR and relatively cooler fresh charge [51]. Recently, Lawler et al. [52] investigated the effect of direct water injection on heat release in engines using PCI. It was found that water injection retards combustion due to the latent heat of vaporization and reduces the heat release rate by local evaporative cooling. The proposed thermal stratification strategy of direct water injection was found to extend the load range by more than 350%.

While there has been a significant amount of studies on the transition from ignition to deflagration [53] as well as from deflagration to end-gas auto-ignition and detonation [18, 54, 55], few studies are found on the transition from deflagration to spontaneous propagation and its subsequent effect on the propagation speed of the emanating fronts. A recent study [56] investigated the flame dynamics at auto-ignitive conditions under the influence of oscillating inlet velocities. It was observed that transition between a multibrachial autoignition front and a tribrachial flame occurs periodically, albeit with hysteresis, due to the finite induction time for autoignition. However, the effect of thermal stratification which is often observed to occur in IC engines [57] was not considered in their study. As demonstrated in [50], heat transfer through cylinder walls and imperfect mixing with the residuals results in pockets

of stratified temperature fields within the combustion chamber. It still remains unclear how the different length scales of such pockets affect a transition in the combustion mode of the emerging reaction fronts. Meanwhile, many practical fuels at typical engine conditions exhibit either a coupled low-temperature and high-temperature double flame or a single high temperature flame. Such contrasting flame structures merit further investigation into their individual response to the inherent thermal stratification present in IC engines. Moreover, a large class of hydrocarbon fuels also exhibit NTC behavior where the ignition delay time is a non-monotonic function of temperature. As a result, an accurate prediction of relevant front propagation speeds in the NTC regime under the influence of thermal stratification is also of primary significance.

1.4.2 Mixture and reactivity stratification

Direct injection spark ignition (DISI) engine is a prime example wherein mixture stratification is employed to provide higher thermal efficiency than a conventional engine with port fuel injection. The combustion process in a DISI engine is a combination of homogeneous and stratified charge combustion. Homogeneous charge is used for heavy accelerations where fuel is injected during the intake stroke to provide near-stoichiometric mixtures for combustion. For light loads and cruising conditions, a stratified charge is used, which consists of pockets of combustible mixture within a larger volume of fuel-lean mixture. The combustible mixture layer is concentrated around the spark plug. On the other hand, for controlling combustion phasing and heat release rate in dual fuel PCI strategies such as Reactivity Controlled Compression Ignition (RCCI), in-cylinder blending of two fuels with different autoignition characteristics is employed. Multi-cylinder work by Curran et al. [43] has demonstrated that brake thermal efficiencies of RCCI are competitive or higher than production conventional diesel combustion, while achieving extremely low engine-out emissions, without the need for NO_x and soot after treatment. Additionally, Splitter et al. [58] demonstrated that full-load RCCI at 1800 revolutions per minute (RPM) was possible with gasoline and diesel fuel in a single-cylinder heavy-duty engine with a compression ratio of 12.

The multi-fuel combustion process involves introduction of a low-reactivity fuel through port or early injection to create a well-mixed charge of the low-reactivity fuel, air and

recirculated exhaust gases. The high-reactivity fuel is later injected close to TDC using single or multiple injections directly into the combustion chamber [59, 60]. The sequential direct injection of the high-reactivity fuel results in pockets of stratified composition fields in the combustion chamber. Bhagatwala et al. [9] performed DNS of inhomogeneous auto-ignition of a primary reference fuel (PRF) mixture consisting of n-heptane and iso-octane under the effect of compression heating. Both deflagration and spontaneous ignition fronts were observed to co-exist, however it was found that higher n-heptane concentration provided a greater degree of flame propagation, whereas lower n-heptane concentration resulted in more spontaneous ignition fronts. Yet, it still remains unclear how the different stratification length scales would affect the propagation speed and the combustion mode of the emerging reaction fronts. Contrary to the competing effects of temperature and equivalence ratio distributions, the equivalence ratio and fuel-reactivity distributions are complementary. That is, neglecting inhomogeneities in the background low-reactivity fuel distribution, the regions with the largest high-reactivity fuel concentrations have both the highest equivalence ratios and the highest fuel reactivity. Hence, further investigation into flame dynamics under equivalence ratio/fuel reactivity stratification may unravel more interesting flame dynamics.

1.4.3 Turbulence

Turbulent combustion is routinely encountered in most practical combustion systems such as rockets, IC engines, aircraft engines, industrial burners and furnaces etc. On the contrary, laminar combustion applications are almost limited to candles, lighters and some domestic furnaces. Turbulent combustion results from the two-way interaction of chemistry and turbulence. In a turbulent premixed flame, the flame front interacts with turbulent eddies which may have speeds of the order of tens of m/s and sizes ranging from a few millimeters to a few meters. This interaction may enhance the chemical reaction but also, in extreme cases, completely inhibit it, leading to flame quenching. Most studies of turbulent combustion are concerned with the effects of turbulence on the flame front. However, the flame also modifies the turbulent flow field. When a flame interacts with a turbulent flow, turbulence is modified by combustion because of the strong flow accelerations through the flame front induced by heat release, and because of the large changes in kinematic viscosity associated with

temperature changes. This mechanism may generate turbulence, called "flame-generated turbulence" or damp it (relaminarization due to combustion).

There has been a number of studies of turbulent premixed flames in which the role of turbulent intensity on flame burning velocities and flame structures has been the major focus (e.g. [61–68] and references therein). The effects of pressure [69, 70], Lewis number [71], preferential diffusion [72], turbulent flame geometry [73], equivalence ratio [74] and unburned temperature [62] on turbulent flame propagation have also been examined. All these studies employed a turbulent flame regime diagram called the Borghi diagram to provide insightful information for different flame regimes [75]. This diagram defines the boundaries between wrinkled, corrugated, thin reaction zone and distributed reaction zone flames based on the ratio of turbulence scales to characteristic flame scales. However, these turbulent flame studies as well as the Borghi diagram have been based on the assumption of a chemically frozen flow ahead of the flame. These studies also neglected the effect of low temperature chemistry (LTC) for transportation fuels at elevated temperatures and pressures [54, 76, 77].

Recently, the effect of LTC on turbulent flame speed was investigated experimentally [78, 79]. At a constant turbulence intensity, a significant increase in turbulent flame speed was observed as the mixture underwent first-stage ignition. This increase was attributed to an increase in the laminar flame speed and a decrease in fuel Lewis number. Four different turbulent combustion regimes were identified based on the competition of the ignition, flow and flame time scales. These experimental investigations provided initial evidence of non-unique turbulent flame regimes and turbulent flame speeds of fuels exhibiting LTC. Subsequently, DNS of cool and hot flames propagating in a mixture that has undergone first stage ignition have been recently carried out by Savard et al. [80]. In their study, the increase in turbulent flame speed was again attributed to the increase in laminar flame speed, as opposed to turbulence-LTC interaction. With reference to cool flames, it was found that the reaction zone structure approaches that of the reference laminar flame and the normalized turbulent flame speed was found to be comparable to that of hot flames. While this study provided significant insights into the role of LTC in turbulent flame propagation, the effects of thermal or composition stratification were not considered. Moreover, under the chosen conditions, there was a large separation between first-stage and second-stage ignition delay

times such that cool flames and hot flames were isolated from one another. As such, a coupled low-temperature and high-temperature double flame which has been shown to exist under engine relevant conditions [54, 81, 82] was not considered.

Depending on the fuel injection timing, exhaust gas recirculation and the amount of wall heat loss, different correlations may occur between temperature (T) and equivalence ratio (ϕ) prior to major heat release event. Essentially, it is plausible to think of two limiting scenarios: 1) early start of injection may result in largely uncorrelated T and ϕ fields mostly due to turbulence mixing and wall heat loss; and 2) late start of fuel injection may result in negatively correlated T and ϕ fields, mostly due to evaporative cooling. Insufficient mixing between hot residual gas and the fresh charge can also result in a negatively correlated T and ϕ fields. Due to the presence of turbulence, large-scale stratification of charge leads to small-scale inhomogeneities in both temperature and fuel mass fraction. Additionally, the various combustion devices utilize large hydrocarbon fuels such as diesel and jet fuels which have a strong LTC behavior. As such, not only turbulence, but fuel chemistry and molecular transport are also expected to play an important role in affecting turbulent combustion. The mode as well as speed of a reaction front under such conditions still remains unclear and needs to be investigated further.

1.4.4 Shocks and contact discontinuities

Compressible reacting flows such as those encountered in PCI may display sharp spatial variation related to shocks, contact discontinuities or reactive zones embedded within relatively smooth regions. Therefore, numerical methods for compressible turbulent flows require robust shock capturing, as well as minimal dissipation and dispersion errors. Resolving the shock thickness is impractical for the DNS of turbulence, as the mean free path is typically orders of magnitude smaller than that of the Kolmogorov length scale [83].

Weighted Essentially Non-Oscillatory (WENO) schemes [84] are a class of numerical methods that have been shown to be capable of capturing discontinuities in compressible flows, while also being suitable for DNS. WENO schemes obtain a numerical approximation to the advective fluxes in the governing equation using a weighted sum of fluxes computed using multiple candidate stencils. The weights are determined by adapting to the presence

of discontinuities such that the solution tends to approach high accuracy and low dissipation in smooth regions of the flow. WENO schemes are considerably more expensive than regular central-difference schemes due to the need to evaluate the same flux functions from multiple candidate stencils [85]. However, the numerical method is suitable for implementation in finite-difference codes using stencil operations very similar to the central-difference schemes. Also, the usual advantages of DNS using finite-difference schemes such as parallelism and scalability carries over to the WENO schemes as well. While the WENO schemes are well established, their actual implementations into the reacting-flow DNS on multiple GPU architectures along with a thorough performance assessment have not been reported in the past. A simple implementation methodology of WENO schemes into reacting-flow DNS solver is expected to be particularly useful to CFD application developers implementing the WENO scheme for the first time.

1.5 Objectives

In light of the discussion presented above, several key questions in the field are addressed in this dissertation. First, what is the effect of different scales of thermal stratification on the propagation speed of reaction fronts in modern IC engines utilizing mixed modes of combustion? Second, how differently does an auto-ignitive binary-fuel flame respond to different scales of composition stratification compared to an auto-ignitive single-fuel flame? Third, how effective are the WENO schemes in performing DNS of turbulent flame propagation in stratified mixtures at auto-ignitive conditions? Finally, how does the propagation speed of turbulent flames evolve in an auto-ignitive fuel/air mixture evolve under the influence of thermal and composition stratification? The following specific objectives are designed to answer these key questions.

1.5.1 Objective I - Effects of thermal stratification on flame propagation at auto-ignitive conditions

Using a 1-D statistically stationary planar configuration,

- Explain the dependence of steady propagation speed of an auto-ignitive dimethyl-ether (DME)/air mixture to its level of upstream reactivity and auto-ignition delay time.
- Provide a parametric mapping of propagation speeds of an auto-ignitive DME/air mixture with/without multi-stage ignition under monochromatic thermal stratification at various time scales.
- Examine the effects of different time scales of monochromatic thermal stratification on low-temperature chemistry (LTC) and high-temperature chemistry (HTC).
- Quantify the transition of combustion modes under such conditions.

This will be discussed in chapter 2.

1.5.2 Objective II - Effects of composition and reactivity stratification on flame propagation at auto-ignitive conditions

Using a 1-D statistically stationary planar configuration,

- Provide a parametric mapping of propagation speed of an auto-ignitive methane (CH_4) blended dimethyl-ether (DME)/air mixture with/without multi-stage ignition under monochromatic DME composition stratification at different time scales.
- Determine the influence of varying DME/CH_4 blending ratio in the binary fuel blend on the dynamic flame response.
- Examine the effects of different time scales of monochromatic DME composition stratification on low-temperature chemistry (LTC) and high-temperature chemistry (HTC).
- Quantify the transition of combustion mode under such conditions.

This will be discussed in chapter 3.

1.5.3 Objective III - Showcasing the importance of WENO schemes in DNS solvers

- Present the implementation and validation of high-order WENO schemes in KARFS.
- Investigate the performance characteristics of KARFS by adopting various types of parallelism strategies.
- Demonstrate execution of KARFS on heterogeneous architectures.

This will be discussed in chapter 4.

1.5.4 Objective IV - Effects of thermal and composition stratification on turbulent flame propagation at auto-ignitive conditions

Using a 2-D statistically stationary planar configuration,

- Explain the influence of different stratification length scales and T-ϕ correlations on the structure of a multi-staged turbulent premixed DME/air flame at auto-ignitive conditions under an identical turbulent intensity.
- Obtain statistical measures of the influence of turbulence and upstream reactivity on the global burning velocity of the flame by determining the individual contributions of flame wrinkling (A') and the enhancement of burning rate per unit surface area (I_0) to the overall burning rate.
- Elucidate the effects of stratification/turbulence length scales on the combustion mode of the mean turbulent flame front.

This will be discussed in chapter 5. Finally, Chapter 6 summarizes the main contributions and insights from this work and provides recommendations for future study. The original contributions presented in this dissertation have also been reported/are to be reported in the following journal publications:

Chapter 2: **S. Desai**, R. Sankaran and H.G Im, "Unsteady deflagration speed of an auto-ignitive dimethyl-ether (DME)/air mixture at stratified conditions", Proceedings of the Combustion Institute 37 (4): 4717 – 4727, 2019 [77]

The author's primary contributions to this paper include (i) development of the problem into a research aim, (ii) identification of the parameter space to be investigated, (iii) all of the gathering and reviewing of literature, (iv) performing numerical simulations and analyzing the results, (v) all of the writing.

Chapter 3: **S. Desai**, R. Sankaran and H.G. Im, "Auto-ignitive deflagration speed of methane (CH_4) blended dimethyl-ether (DME)/air mixtures at stratified conditions", Combustion and Flame, 211: 377 – 391, 2020 [86]

The author's primary contributions to this paper include (i) development of the problem into a research aim, (ii) identification of the parameter space to be investigated, (iii) all of the gathering and reviewing of literature, (iv) performing numerical simulations and analyzing the results, (v) all of the writing.

Chapter 4: **S. Desai**, Y. J. Kim, W. Song, M. B. Luong, F. E. H. Pérez, R. Sankaran, and H. G. Im, "Direct numerical simulations of reacting flows with shock waves and stiff chemistry using many-core/GPU acceleration", Computers and Fluids, 2019 (Under review).

The author's primary contributions to this paper include (i) development of the problem into a research aim, (ii) identification of the need to conduct the investigation, (iii) all of the gathering and reviewing of literature, (iv) implementing and validating the WENO schemes as well as carrying out the performance analysis of the code on heterogeneous architectures, (v) pulling various contributions into a single paper and (vi) majority of the writing.

Chapter 5: **S. Desai**, R. Sankaran and H.G. Im, "Direct numerical simulation of auto-ignitive turbulent flames in a stratified dimethyl-ether (DME)/air mixture", Combustion and Flame, 2019 (Submitted).

The author's primary contributions to this paper include (i) development of the problem into a research aim, (ii) identification of the parameter space to be investigated, (iii) all of the gathering and reviewing of literature, (iv) performing numerical simulations and analyzing the results, (v) all of the writing.

Since DNS does not utilize any closure model except the chemistry model, the major source of uncertainties in the obtained results arise due to the employed combustion model itself. As such, the uncertainties associated with the results presented here are directly linked to the inherent uncertainties in the utilized chemical mechanism that have been outlined in [44, 87]. Meanwhile, the uncertainties in obtained results associated with the grid sizes, time-step sizes and the imposed boundary conditions have been mitigated by performing grid size and time-step size dependency studies as well as verifying the implementation of the imposed boundary conditions using the methodology adopted in [88, 89].

Chapter 2

Effects of thermal stratification on flame propagation at auto-ignitive conditions

In this chapter, the propagation speed of an auto-ignitive dimethyl-ether (DME)/air mixture at elevated pressures and subjected to monochromatic temperature oscillations is computationally evaluated in a one-dimensional, statistically stationary configuration using fully resolved numerical simulations with reduced kinetics and transport. Two sets of conditions with temperatures within and slightly above the negative temperature coefficient (NTC) regime are simulated to investigate the fundamental aspects of auto-ignition and flame propagation along with the transition from auto-ignitive deflagration to spontaneous propagation regimes under thermal stratification. A displacement speed budget analysis is also carried out to elucidate the underlying combustion modes that are responsible for such a variation in flame response. The temporal temperature fluctuations imposed on a stationary front corresponds to an IC engine combustion condition in which the reaction front propagates into a pocket of stratified temperature field of a given size. One-dimensional parametric simulations are conducted, and the results are systematically analyzed.

2.1 Numerical procedure and initial conditions

Fully resolved numerical simulations are conducted using KARFS (KAUST Adaptive Reacting Flow Solver), that solves the compressible Navier-Stokes, continuity, species and energy equations (See Appendix A). Spatial derivatives are approximated with an eighth-order finite-difference operator [24] along with a tenth-order explicit filter and solution is advanced in time with a six-stage fourth-order Runge-Kutta method [25]. A reduced DME chemical mechanism [23] consisting of 30 species and 175 reactions with 9 species identified as global quasi-steady state species is employed.

One-dimensional simulations are conducted for two canonical cases: T800 and T1060 with different mean unburnt mixture temperatures, $T_0 = 800$ K and $T_0 = 1060$ K. As can be seen in Figure 2.1, between 780 K and 960 K, the ignition mechanism leads to increased delay time with increasing initial temperature. This is the so-called negative temperature coefficient (NTC) regime. Hence, $T_0 = 800$ K in case T800 is within whereas $T_0 = 1060$ K is outside this NTC regime. In each case, the mixture equivalence ratio $\phi = 0.4$ and the pressure $P_0 = 20$ atm. To avoid large pressure waves within the domain, non-reflective boundary conditions are imposed at the inlet and the outlet as described in [88]. Due to open boundaries, the

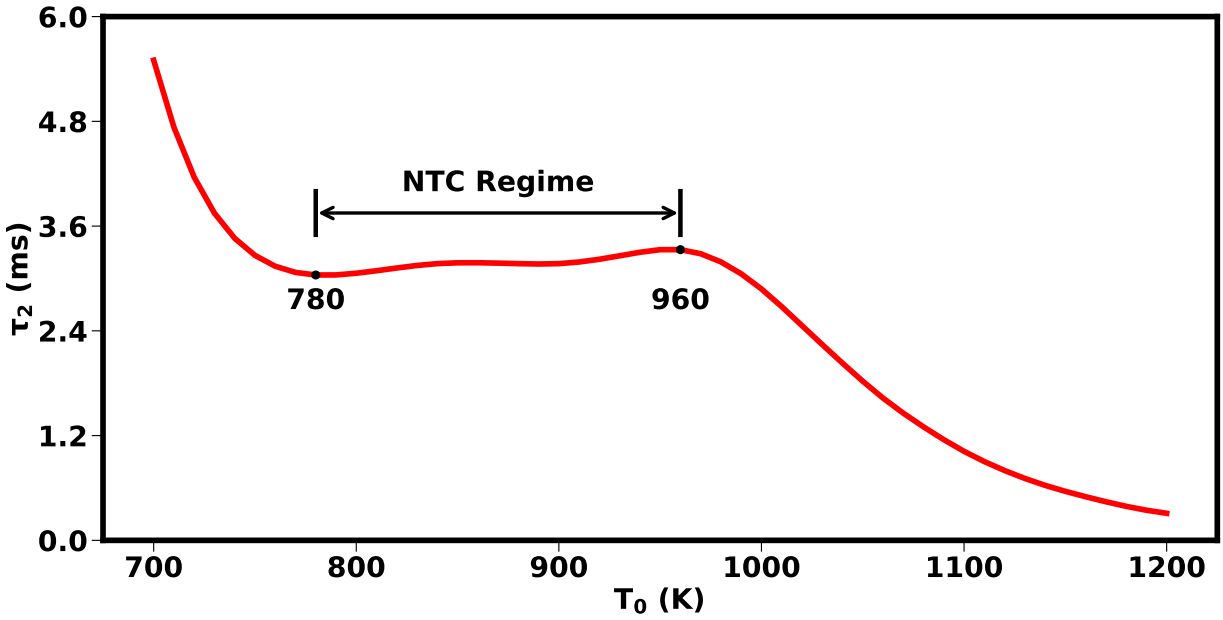

Figure 2.1: Change of ignition delay (τ_2) with the unburnt temperature (T_0) for DME/air mixture at $\phi = 0.4$ and $P = 20$ atm.

thermodynamic pressure remains constant, thereby allowing a statistically stationary limit cycle behaviour to be produced for the unsteady cases. The various physical and numerical parameters used in the present study are listed in Table 2.1. Here, S is the global steady propagation speed, L is the domain length and Δx is the uniform grid resolution. In each case, Δx corresponds to a minimum of 8 grid points across the thinnest radical reaction rate layers (i.e. CH_3O in case T800 and C_2H_2 in case T1060) in the combustion front.

The initial temporal and spatial temperature profiles in the respective cases are as shown in Figure 2.2. τ_1 and τ_2 correspond to the first- and second-stage ignition delay times which have been measured at the points of peak heat release for that respective stage. Similarly, the spatial location from the inlet at which peak heat release occurs in the cool flame and the hot flame is denoted by λ_1 and λ_2 respectively. The overall rise in temperature in each case is around 950 K.

For each case, a series of steady solutions are computed by varying λ_2, for which the correct inflow velocity i.e. S is determined as an eigenvalue using Cantera [1]. Selected steady solutions obtained from Cantera with a fixed inflow velocity are then used to initialize the unsteady simulations where the inlet temperature T_{Inlet} is varied in time as:

$$T_{\text{Inlet}}(t) = T_0 + A \sin\left(\frac{2\pi t}{\tau_0}\right) \tag{2.1}$$

where τ_0 is the time period and A is the amplitude. For case T800, calculations are carried out with thermal stratification at six different time scales i.e. $\tau_0 = \frac{\tau_1}{2}, \tau_1, 2\tau_1, \frac{\tau_2}{2}, \tau_2, 2\tau_2$. For case T1060, calculations are carried out with thermal stratification at three different time scales i.e. $\tau_0 = \frac{\tau_2}{2}, \tau_2, 2\tau_2$. The temporal variation in temperature at the inlet translates into pockets of stratified temperature field due to flow advection. The frequency of oscillation along with the inlet flow velocity determines the characteristic length scale of stratification, which is of the same order as recently observed in an optical IC engine [90]. For the majority

Table 2.1: Physical and numerical parameters used in the two cases

Case	τ_1 (ms)	τ_2 (ms)	λ_1 (mm)	λ_2 (mm)	S (m/s)	L (mm)	Δx (μm)
T800	**0.48**	**3.06**	**1.51**	**13.47**	**3.72**	**40**	**18**
T1060	**-**	**1.63**	**-**	**10.45**	**6.35**	**20**	**6**

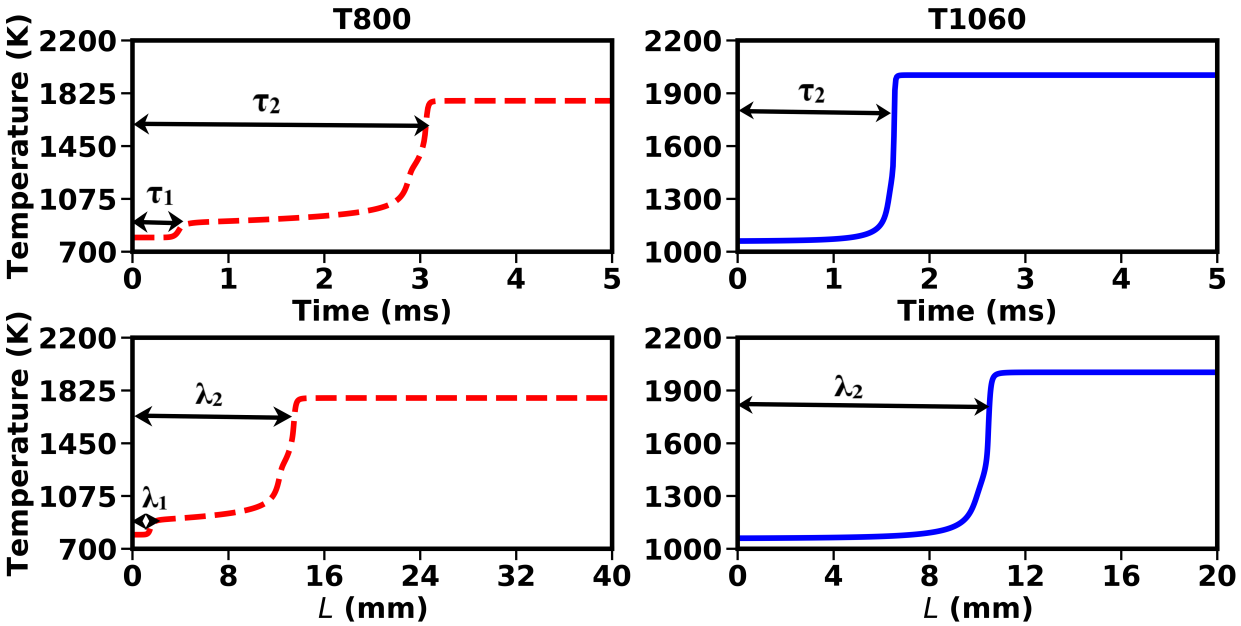

Figure 2.2: Initial temporal and spatial temperature profiles for the two cases

of τ_0 in each case, A is chosen so as to obtain a temperature variation of around 100 K at the flame base, which has been defined as the spatial location where 5% of the unburned fuel mass is consumed. However, to ensure numerical stability and avoid flame blow-off, A is set at a lower value for $\tau_0 > 2\tau_1$ in case T800 which resulted in a temperature variation of around 40 K at the flame base. Nevertheless, the resulting root-mean-square temperature fluctuations at the flame base are comparable to typical values reported in IC engines [91]. Although both temperature and composition fluctuations play an important role in IC engine combustion, only the effects of temperature fluctuations are considered here because, if the initial temperature of the mixture is near or above the NTC regime, large composition fluctuations have been found to be equivalent to large temperature fluctuations [92].

2.2 The steady flame behavior

The dependence of steady propagation speed of an auto-ignitive deflagration front on its level of upstream reactivity is shown in Figure 2.3. In each case, for a given λ_2, S is computed as an eigenvalue in Cantera [1]. S at points F1 and F3 respectively represents the lowest global propagation speed in each case for which a stable steady solution is computed without

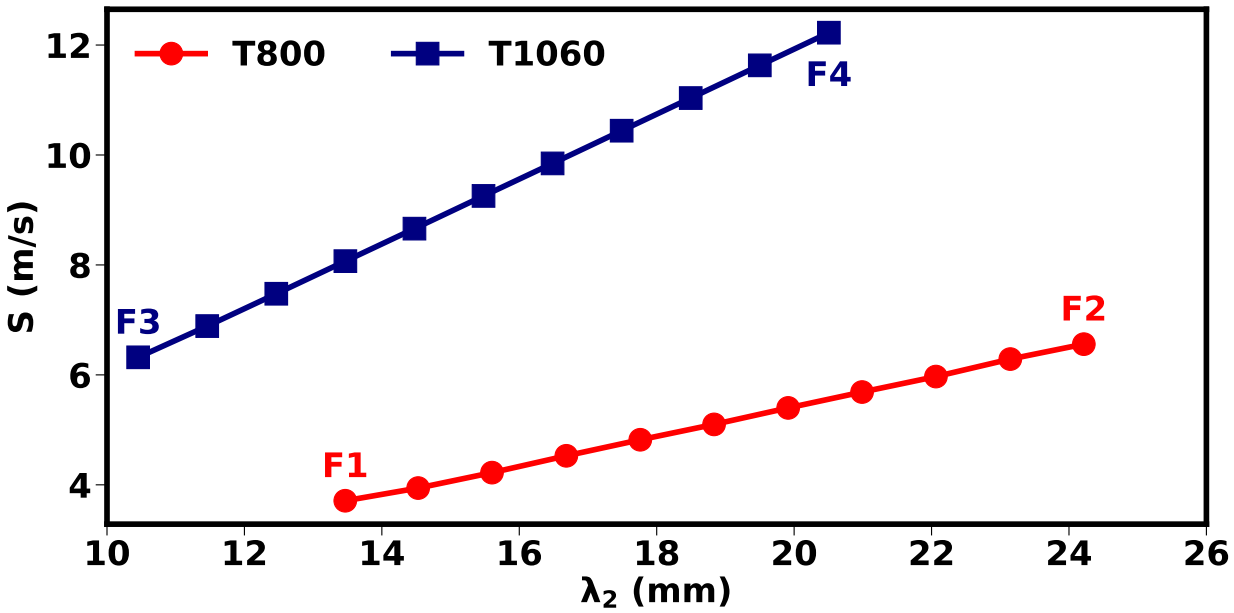

Figure 2.3: Dependence of S on λ_2

any numerical artifacts arising from the inflow boundary conditions. As the respective front position is moved further downstream, at F2 and F4, S rises linearly due to the increased chemical activity in the upstream reactant mixture before it enters the front. Quantitatively, S rises at a faster rate in case T1060. A smaller τ_2 in case T1060 results in a smaller characteristic residence time α_2. Here, $\alpha = \int_0^{\lambda} \frac{1}{\mathrm{u(x)}} \mathrm{dx}$, where u(x) is the local flow velocity. As a result, the reaction front at F3 takes considerably less time to enter the spontaneous propagation regime compared to that at F1, thereby leading to a faster rise in S with λ_2 in case T1060.

For distinguishing the combustion modes of reaction fronts at F1 (or F3) and F2 (or F4), a transport budget analysis [93] in terms of O_2 is performed as shown in Figure 2.4. At each point, it is seen that the reaction term is significantly higher than the diffusion term. This is because the mixture upstream of the front is highly preheated and hence already immensely reactive. Nonetheless, in each case, the diffusion term is not negligible at either of the points but is rather found to gradually decrease from F1 (or F3) to F2 (or F4). Hence, it can be deduced that diffusive transport plays a role in accelerating the combustion front even when the mode of propagation is nearly spontaneous. This deviation between the relative magnitudes of reaction and diffusion terms under the diffusive limit was also observed in [94]

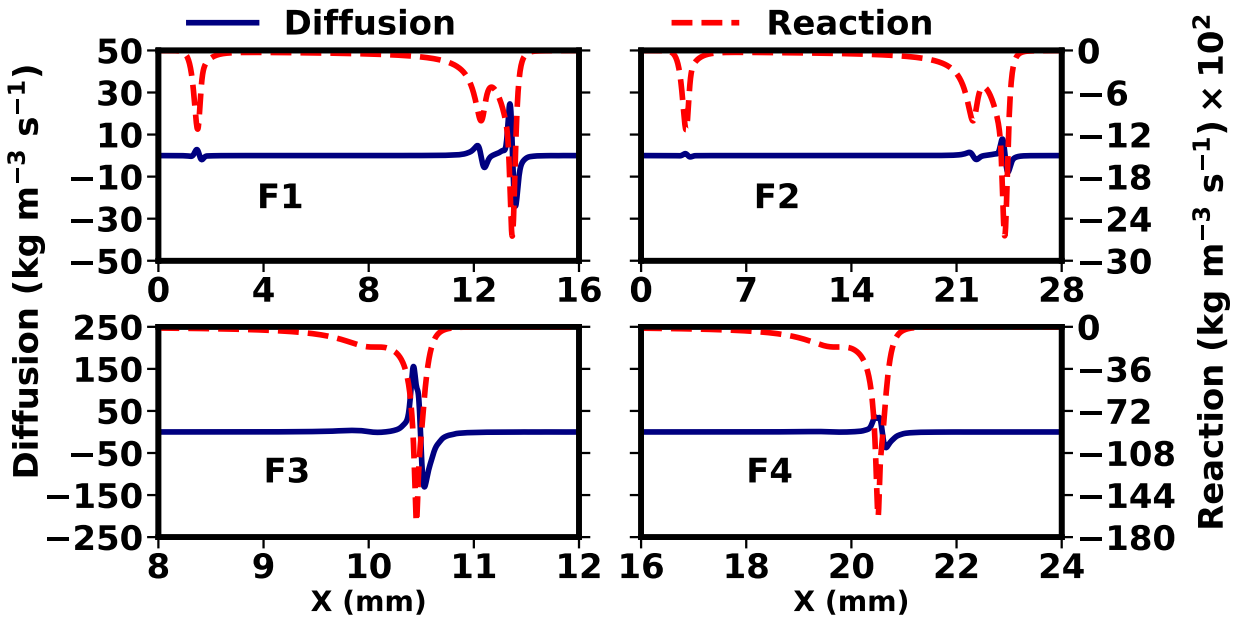

Figure 2.4: Transport budget analysis in terms of O_2 at the respective points. In each sub-figure, the y-axis on the left shows the magnitude of diffusion (solid line) while the one on the right shows the magnitude of reaction (dotted line).

wherein the absolute value of reaction term was found to be 5 times that of the diffusion term. It is also consistent with the observations in [21] where it was found that the transition from deflagration to spontaneous propagation occurs very gradually and usually requires an order of magnitude increase in the inlet velocity.

By definition, spontaneous front propagation is a sequential auto-ignition independent of transport. Therefore, another indication that the spontaneous propagation mode has been reached is that the characteristic residence time is constant across different propagation speeds, irrespective of length scales, $\mathrm{d}\alpha/\mathrm{d}S = 0$. Figure 2.5 shows the behavior of $\mathrm{d}\alpha/\mathrm{d}S$ as a function of λ_2 for the two cases. In each case, α_1 and α_2 approach a constant value as λ_2 increases. This further confirms that the fronts at either F1 or F3 have not yet entirely transitioned to the spontaneous propagation regime. It also demonstrates that the escalation in S with λ_2 is caused by the increasing effect of spontaneous ignition in the upstream mixture. Based on the regime diagram presented in [21], the fronts at F1 and F3 can be considered to be in the auto-ignition assisted deflagration regime where diffusion has non-negligible contribution to the overall front propagation. The variation in $\mathrm{d}\alpha/\mathrm{d}S$ with

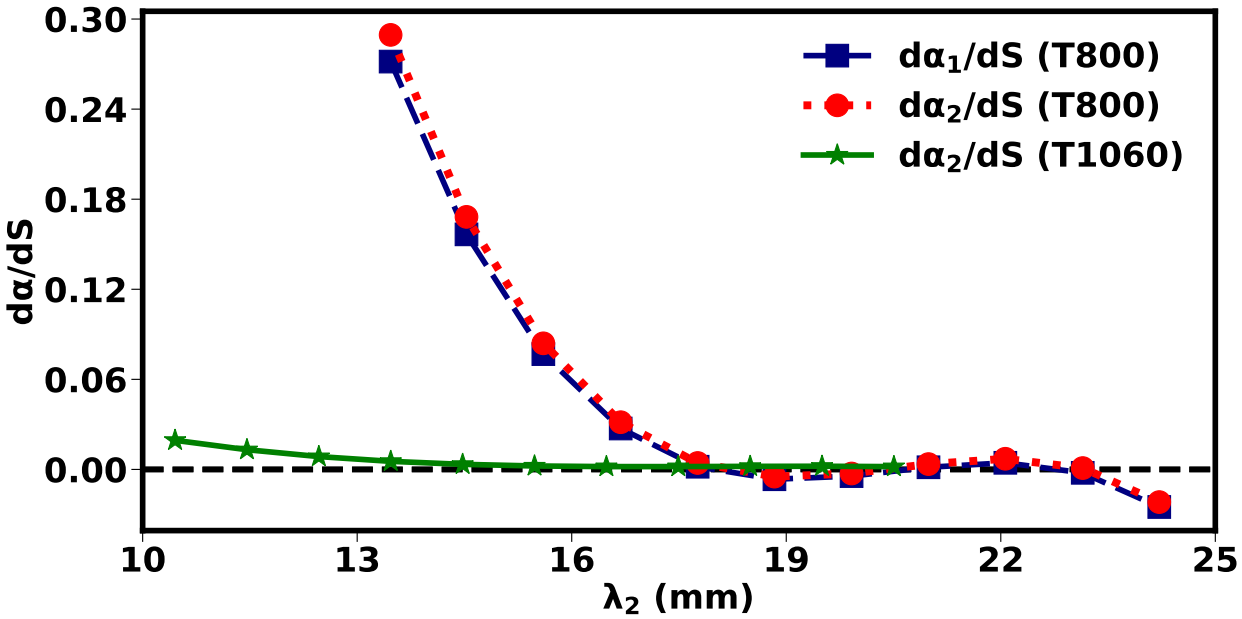

Figure 2.5: Variation in characteristic residence times as a function of λ_2

λ_2 presented in Figure 2.5 also resembles the change in $\mathrm{d}\lambda_2/\mathrm{d}S$ with S that was observed in [21] when a reaction front was in this particular regime.

2.3 Response to unsteady temperature fluctuations

In this section, the flame response to oscillatory temperature fluctuations is presented. Here, the reaction fronts at F1 and F3 whose initial temporal and spatial temperature profiles are depicted in Figure 2.2 have been used as an initial condition for the respective cases. Since the investigation of flame response to the very near upstream conditions is of more practical importance, the instantaneous temperature at the flame base T_b, defined as the spatial location where 5% of the unburned fuel mass has been consumed, is reported for analysis. For the fronts at F1 and F3, T_b is computed to be 830 K and 1097 K, respectively. The spatial location of flame base X_b at F1 and F3 is evaluated to be 1.6 mm and 8.27 mm, respectively. Since the limit-cycle behavior of T_b to T_Inlet is sinusoidal, the presentation of flame response to T_b is consistent with its response to T_Inlet.

Figure 2.6 presents the unsteady global propagation speed S_c as a function of T_b for case T800, after a limit cycle is reached. Here, S_c is defined based on the consumption of oxygen

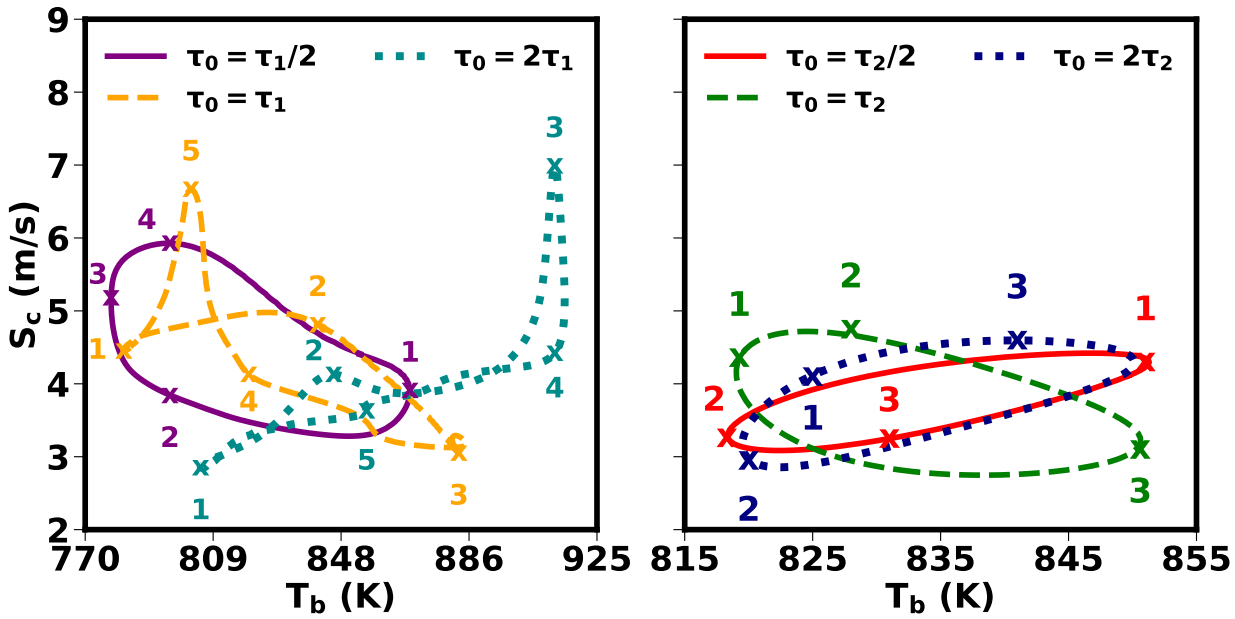

Figure 2.6: S_c as a function of T_b for case T800

as:

$$S_c = -\frac{1}{\rho_u(Y_{O_2,u} - Y_{O_2,b})} \int_0^L \dot{\omega}_{O_2} \, dx \tag{2.2}$$

where ρ_u is the unburned gas density, $Y_{O_2,u}$ and $Y_{O_2,b}$ is the mass fraction of oxygen in the unburned and burned gas, respectively, and $\dot{\omega}_{O_2}$ is the oxygen reaction rate. The left and right figures respectively show the responses to fast and slow oscillations. For each case, numbers denote the temporal progression during the oscillatory cycle. The flame is clearly found to be responsive to all the imposed time scales, showing an overall elliptical shape of the dynamical response. Moreover, the dynamic response is not harmonic but rather hysteretic as has been previously observed in [56, 95]. As notable exceptions, though, the flame response at τ_1 and $2\tau_1$ deviates from an elliptical path to show a complex behavior with a sharp peak. With a further increase in τ_0, the flame is observed to revert to an elliptical path.

A similar analysis is also conducted for case T1060, and the results are shown in Figure 2.7. As before, numbers denote the temporal progression of each limit cycle. Analogous to the previous case, the flame is found to respond to all the imposed time scales with hysteresis. T_b in this case is noticed to remain mostly unaffected by τ_0. The limit cycle again exhibits an intricate shape with peaks and then recovers the elliptical shape as

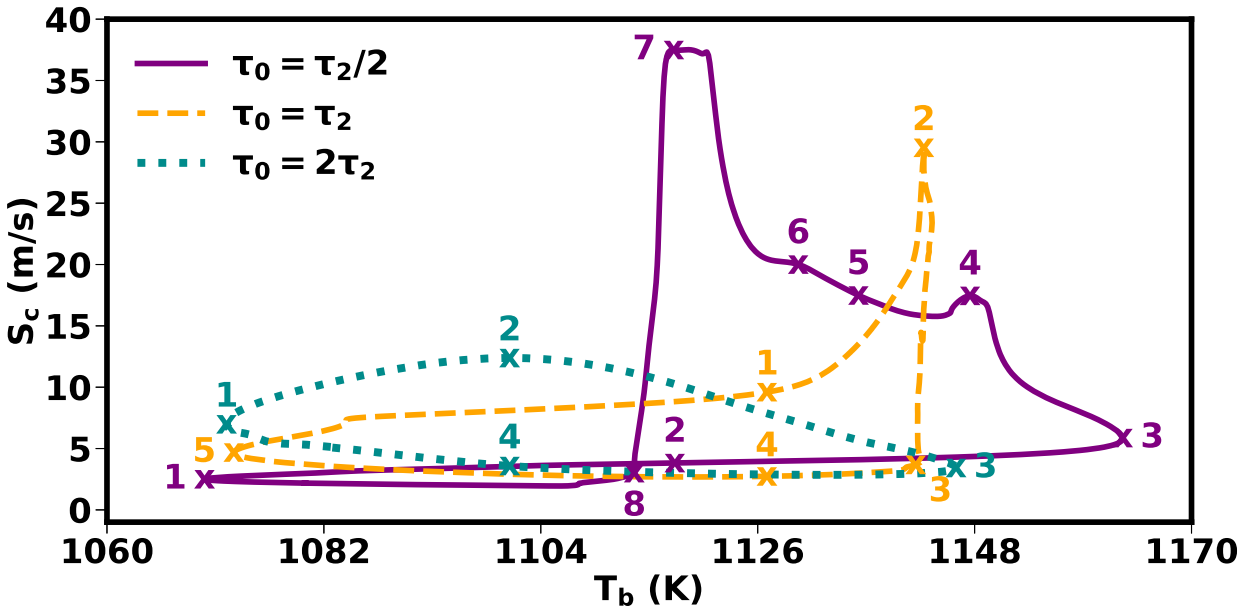

Figure 2.7: S_c as a function of T_b for case T1060

τ_0 is increased. The main difference with respect to case T800 is a very high peak value of instantaneous S_c, as has been observed at $\frac{\tau_2}{2}$ and τ_2 respectively.

Unlike case T1060, T_b in case T800 is found to be highly sensitive to τ_0, specifically when $\tau_0 \leq 2\tau_1$. This is due to the presence of low temperature chemistry (LTC) in case T800 and its distinct response to a given τ_0. Figure 2.8 depicts the variation in various flame parameters over a given limit cycle in case T800. Here, $\beta = t/\tau_0$ represents the fraction of a complete limit cycle. The observed change in X_b compared to T_b is lower at $\tau_1/2$ than at $2\tau_1$. From the computed values of X_b and λ_1 in case T800, it is found that 5% of the unburned fuel mass consumption occurs during the first-stage of ignition involving LTC. As a result, the sensitivity of T_b and X_b to τ_0 in case T800 is directly affected by the response of LTC to a given τ_0. The variation in cumulative reaction rate of LTC radical species $CH_3OCH_2O_2$ [21], $\dot{\Omega}_{CH_3OCH_2O_2}$, with β shows that LTC response is dependent on τ_0. Here, $\dot{\Omega}_k = \int_0^L \dot{\omega}_k \, dx$ where $\dot{\omega}_k$ is the reaction rate of species k. Contrary to the observation at $2\tau_1$, there is a sudden consumption of $CH_3OCH_2O_2$ radical at $\tau_1/2$ which subsequently leads to a lower variation in X_b. These findings show that, unlike [56] wherein LTC was found to be decoupled from flow dynamics due to significantly smaller oscillation frequencies employed, it (i.e. LTC) interacts with the flow dynamics and shows varying response to a given τ_0.

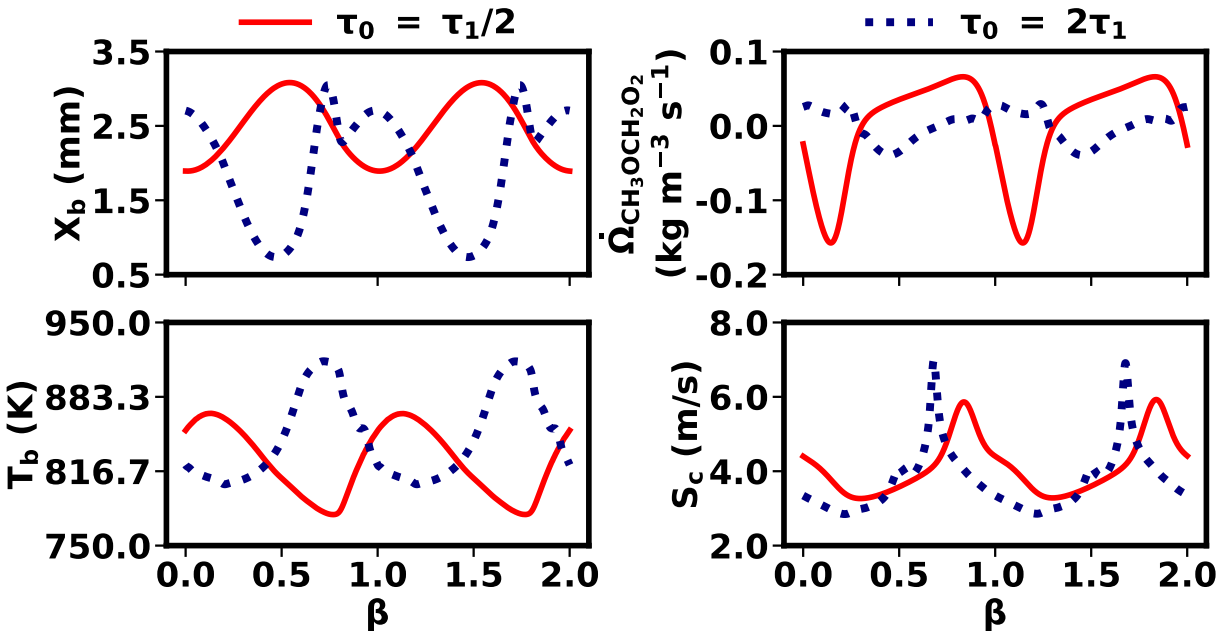

Figure 2.8: Change in X_b, T_b, $\dot{\Omega}_{CH_3OCH_2O_2}$ and S_c with β for a given τ_0 in case T800

Moreover, the sudden rise in S_c at specific τ_0 in each case is attributed to the increase in cumulative reaction rate of high-temperature chemistry (HTC) radical species OH [21], $\dot{\Omega}_{OH}$, as shown in Figure 2.9. It is seen that, in each case, the peak in $\dot{\Omega}_{OH}$ coincides with the corresponding peak in S_c. Besides, the variation in $\dot{\Omega}_{OH}$ and hence S_c with β is relatively abrupt at $2\tau_1$ and $\tau_2/2$ in cases T800 and T1060 respectively. These findings demonstrate that HTC is mainly responsible for the sharp rise in S_c at specific τ_0 in each case. It is also found that unlike LTC, HTC in case T800 becomes increasingly more active with an increase in τ_0. Due to a considerably larger amount of OH production at $\tau_2/2$ in case T1060, instantaneous S_c is significantly higher. It can also be noticed from Figures 2.8 and 2.9 that a phase lag between S_c and T_b coupled with sudden inflation in instantaneous S_c is responsible for hysteresis and tilting of the dynamic flame response.

2.4 Identification of combustion modes

In Figure 2.6, S_c has been used in as a better metric to represent the global propagation speed of a reaction front having characteristics of auto-ignition or deflagration. In contrast, density weighted displacement speed, S_d, is more appropriate in analyzing the individual

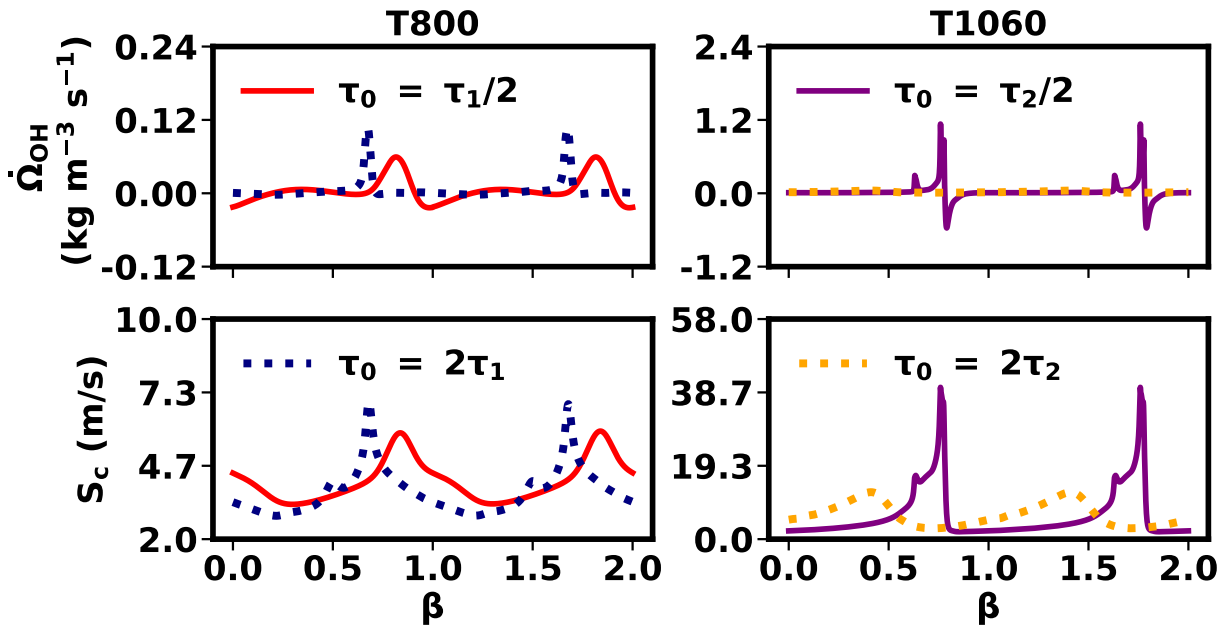

Figure 2.9: Change in $\dot{\Omega}_{\mathrm{OH}}$ and S_{c} with β for a given τ_0 in each case

contributions of diffusion and reaction terms on the net propagation, which is not possible with S_{c}. Hence, a displacement speed budget analysis is performed for quantifying the nature of the combustion mode. S_{d} is defined by the movement of a scalar iso-surface that corresponds to the reaction front. For a given surface of a species, the density-weighted displacement speed is defined as [96]:

$$S_{\mathrm{d}} = \frac{1}{\rho_{\mathrm{u}}|\nabla Y_{\mathrm{k}}|}(-\dot{\omega}_{\mathrm{k}} - \nabla \cdot (\rho D Y_{\mathrm{k}})) \tag{2.3}$$

where ρ is the density, $\dot{\omega}_k$ is the reaction rate of species k, and D is the species diffusivity. The first term on the right hand side is due to reaction, $S_{\mathrm{d,r}}$ $(= \frac{-\dot{\omega}_{\mathrm{k}}}{\rho_{\mathrm{u}}|\nabla Y_{\mathrm{k}}|})$, while the second term is due to diffusion, $S_{\mathrm{d,d}}$ $(= \frac{-\nabla\cdot(\rho D Y_{\mathrm{k}})}{\rho_{\mathrm{u}}|\nabla Y_{\mathrm{k}}|})$. For the present study, the instantaneous displacement speed is computed at the spatial location where 90% of the initial oxygen mass is consumed. The steady and unsteady displacement speed results based on the chosen iso-surface guarantee that analysis is always performed within the main heat-release zone.

As shown in Figure 2.10, the S_{d} budget analysis is carried out for the smaller time scales $(\tau_0 = \tau_1, 2\tau_1)$ in case T800 for understanding the underlying combustion modes that lead to sharp peaks in S_{c}. The time points 1 to 5 indicated in Figure 2.6 are also shown on top

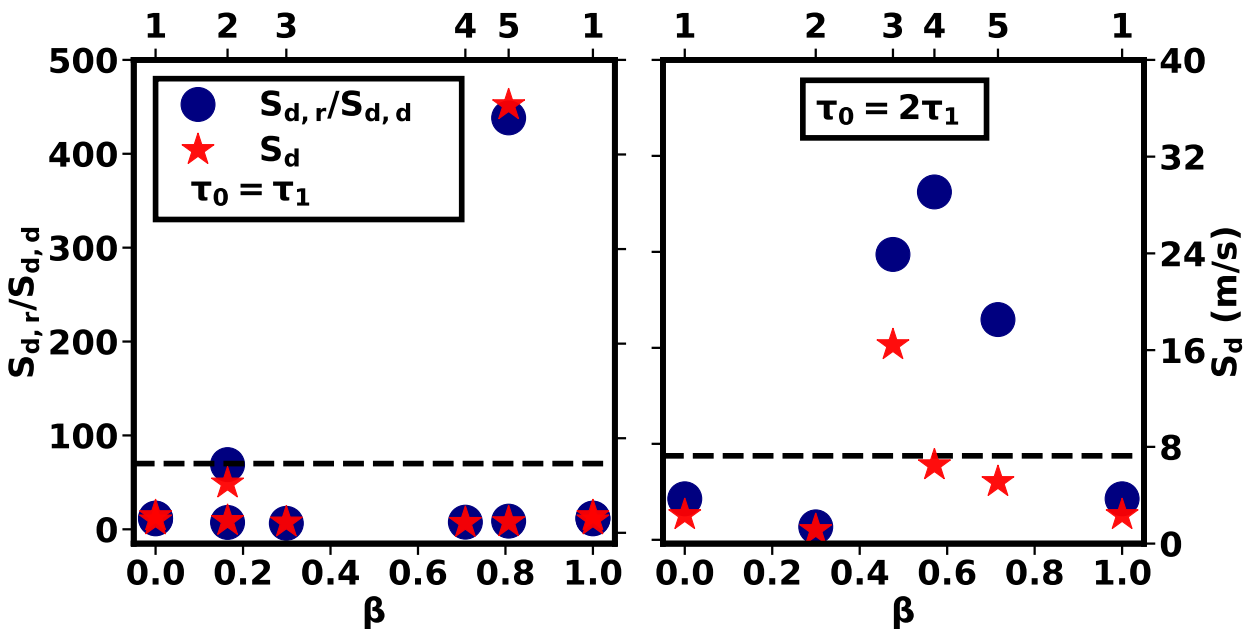

Figure 2.10: S_d budget for the hot flame in case T800. In each sub-figure, the y-axis on the left shows the ratio $S_{\mathrm{d,r}}/S_{\mathrm{d,d}}$ (blue circles) while the one on the right shows total S_d (red stars). Dotted line indicates the threshold $S_{\mathrm{d,r}}/S_{\mathrm{d,d}}$ as evaluated at point F1 in Figure 2.3.

of the x-axis. Apart from the absolute value of S_d, the values of the ratio $S_{\mathrm{d,r}}/S_{\mathrm{d,d}}$ at the individual time points are also depicted. For differentiating deflagration from spontaneous propagation, a threshold value of $S_{\mathrm{d,r}}/S_{\mathrm{d,d}} = 70$ and 20, as evaluated at points F1 and F3 in Figure 2.3, is used in cases T800 and T1060, respectively. It is evident that for each τ_0, the front undergoes a periodic transition from deflagration ($S_{\mathrm{d,r}}/S_{\mathrm{d,d}} < 70$) to spontaneous propagation ($S_{\mathrm{d,r}}/S_{\mathrm{d,d}} > 70$). Unlike the limit cycle at $2\tau_1$, multiple fronts with distinct combustion modes and S_d are observed to coëxist at $\beta = 0.16$ and 0.81, respectively. These findings suggest that the observed rise in instantaneous S_c at τ_1 and $2\tau_1$ is attributed to different phenomena. For all the points from 1 to 5 at τ_1 and $2\tau_1$, the temperature at the spatial location of the chosen iso-surface $T_{\mathrm{O_2},90\%} \approx 2\ T_\mathrm{b}$. Besides, based on the values of β for the limit cycle at τ_1, the time taken (Δt) by the reaction front to transition from deflagration at point 4 to spontaneous propagation at point 5 is ≈ 48 μs. In contrast, at $2\tau_1$, Δt between points 2 and 3 is ≈ 173 μs. This result indicates that there is a sudden increase in S_c at τ_1 and is attributed to the momentary coëxistence of two fronts having different combustion modes, whereas there is a relatively gradual rise in S_c at $2\tau_1$ and is a consequence of the transition of a deflagration to spontaneous propagation regime. It can

therefore be concluded that when the fuel/air mixture with a two-stage ignition is within the NTC regime and $\tau_0 = \tau_1$, there is a sudden increase in the propagation speed wherein a significant amount of reactants are consumed within a very short time. No such abrupt rise in the front propagation speed is observed when $\tau_0 = \tau_2$. This is also partly due to a lower amplitude A. It should be noted that unlike S_c, S_d is calculated locally. As a result, the relative difference in magnitudes of S_c and S_d is dependent on the spatial location of the iso-surface used for computing S_d. Moreover, since multiple fronts with distinct S_d are observed to coëxist at specific τ_0 in each case, the limit cycles have not been presented in terms of S_d.

An identical S_d budget analysis is also performed for the cool flame in case T800 for the smaller time scales ($\tau_0 = \tau_1, 2\tau_1$) to understand the evolution of combustion modes in the cool flame during a given limit cycle. The S_d budget analysis for the cool flame is performed at the spatial location where 5% of the initial oxygen mass is consumed so as to ensure that the chosen iso-surface is always located in the heat-release zone of the cool flame. Based on the transport budget analysis as shown in Figure 2.4, it is found that the cool flame at point F1 is predominantly in the spontaneous propagation regime with negligible contribution from diffusion. This observation is further confirmed from the S_d budget analysis as shown in Figure 2.11. For consistency, $S_{d,r}/S_{d,d} = 70$ is used as the threshold for differentiating auto-ignitive deflagration from spontaneous propagation. As before, numbers 1 to 5 on top of the x-axis denote the temporal progression of the limit cycle. Unlike the observations for the high-temperature flame, two separate cool flames are never observed to co-exist at any point on the chosen limit cycles. Yet, the cool flame is seen to periodically transition from spontaneous propagation to deflagration. Unlike the high-temperature flame, peak instantaneous S_d of the cool flame at a given τ_0 is significantly lower and occurs much earlier during the limit cycle.

In order to justify the validity of the chosen iso-surface in accurately identifying the multiple fronts with distinct combustion modes, the spatial evolution of temperature for the limit cycle at τ_1 in case T800 is shown in Figure 2.12 as a representative case. At point 1, two separate deflagration fronts — one arising due to pre-ignition and the other being the initial flame itself exist simultaneously. At point 2, the initial front now enters the

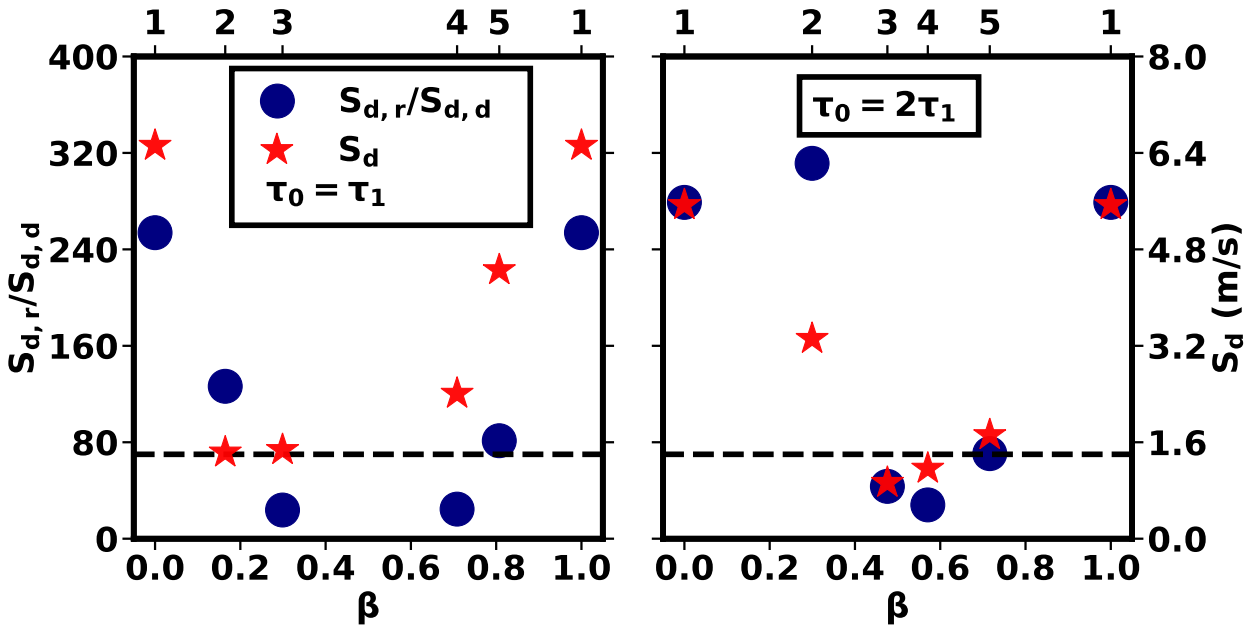

Figure 2.11: S_{d} budget for the cool flame in case T800. In each sub-figure, the y-axis on the left shows the ratio $S_{\mathrm{d,r}}/S_{\mathrm{d,d}}$ (blue circles) while the one on the right shows total S_{d} (red stars). Dotted line indicates the threshold $S_{\mathrm{d,r}}/S_{\mathrm{d,d}}$, as evaluated at point F1 in Figure 2.3.

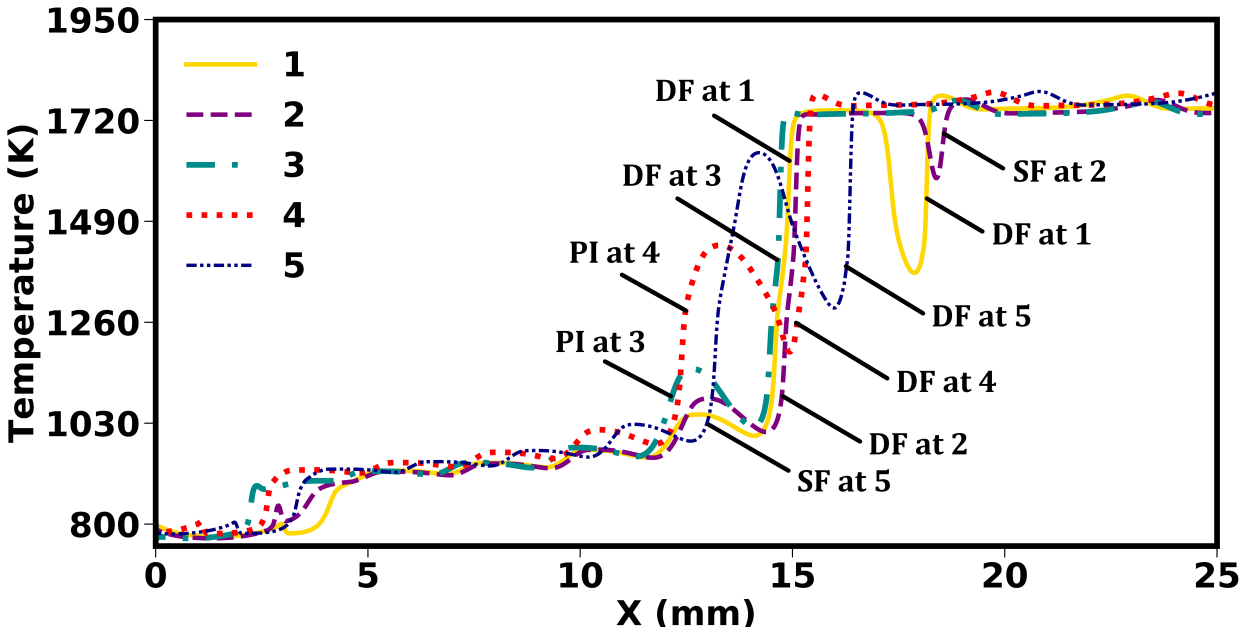

Figure 2.12: Spatial evolution of temperature for $\tau_0 = \tau_1$ in case T800. DF = Deflagration Front, SF = Spontaneous Propagation Front, PI = Pre-ignition.

spontaneous regime while the upstream front is still in the deflagration regime. These two fronts merge at point 3 to form a single deflagration front while the auto-ignition chemistry in the upstream mixture begins to develop. There is no change in the combustion mode of the front at point 4, but pre-ignition in the upstream mixture is on the verge of developing into a separate front. The observed pre-ignition in the upstream mixture finally matures into a spontaneous propagation front ahead of the deflagration front at point 5. Finally, the spontaneous propagation front at point 5 reverts back to the deflagration regime at point 1. As a result, two separate deflagration fronts co-exist at point 1, and the cycle repeats.

A S_{d} budget analysis for the hot flame, identical to case T800, is also performed for case T1060. From Figure 2.13, it is seen that at $\frac{\tau_2}{2}$, multiple fronts with distinct combustion modes and S_{d} co-exist between $\beta = 0.56$ and 0.64. On the other hand, at τ_2, multiple combustion fronts are not observed at any point on the limit-cycle, and the front is observed to undergo a cyclic transition from deflagration to spontaneous propagation. It can be deduced that for an identical amplitude of thermal stratification, when the fuel/air mixture with a single-stage ignition is outside the NTC regime, the propensity of pre-ignition in the upstream mixture to successfully develop into a spontaneous ignition front ahead of

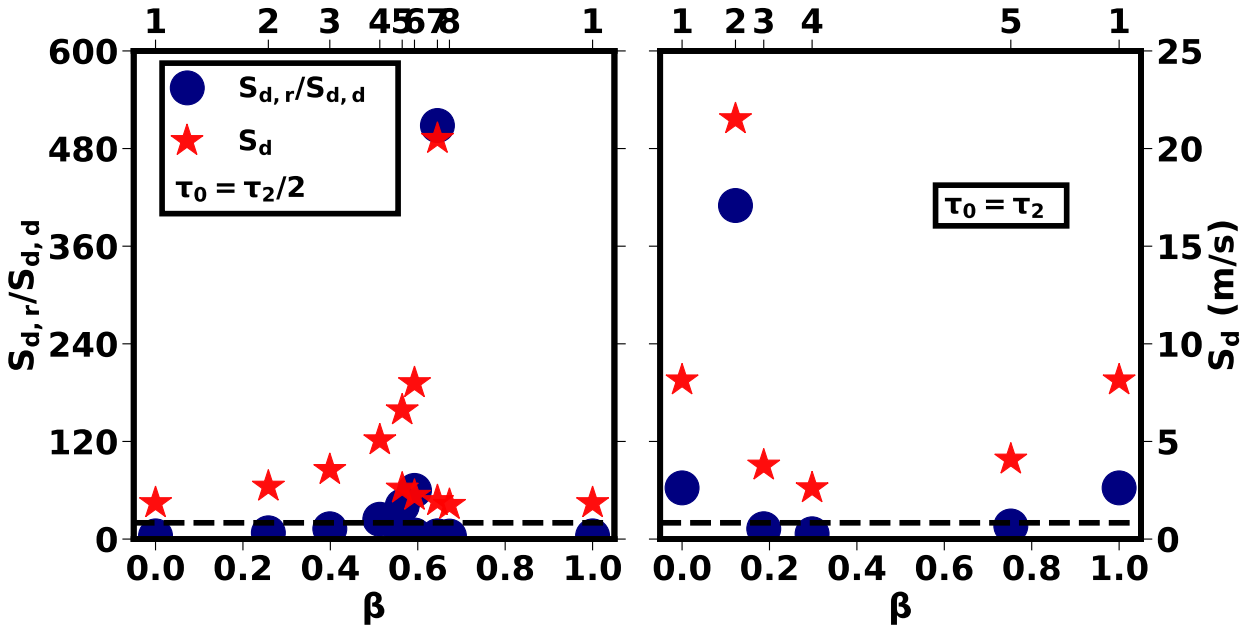

Figure 2.13: S_{d} budget for case T1060. In each sub-figure, the y-axis on the left shows the ratio $S_{\mathrm{d,r}}/S_{\mathrm{d,d}}$ (blue circles) while the one on the right shows total S_{d} (red stars). The dotted line indicates the threshold $S_{\mathrm{d,r}}/S_{\mathrm{d,d}}$, as evaluated at point F3 in Figure 2.3.

deflagration front diminishes with an increase in τ_0. For all the points from 1 to 8 at $\tau_2/2$ and from 1 to 5 at τ_2, $T_{\mathrm{O_2},90\%} \approx 1.7\ T_\mathrm{b}$. In addition, based on the values of β, Δt between points 3 and 4 at $\frac{\tau_2}{2}$ is $\approx 88\ \mu$s while at τ_2, Δt between points 5 and 1 is $\approx 400\ \mu$s. Hence, compared to case T800, there is no abrupt rise in the front propagation speed in case T1060, even when $\tau_0 = \tau_2$. Nonetheless, the total duration for which the spontaneous propagation front exists between points 3 and 8 at $\frac{\tau_2}{2}$ is $\approx 216\ \mu$s. Within the same time, multiple combustion fronts are found to co-exist momentarily between points 5 and 7 for $\approx 72\ \mu$s. Similarly, the spontaneous propagation front between points 5 and 3 at τ_2 exists for $\approx 700\ \mu$s. This duration of existence of spontaneous propagation front is considerably longer than that observed in case T800 at either τ_1 or $2\tau_1$. Therefore, it can be concluded that the relative duration of existence of a spontaneous propagation front in the presence/absence of an additional reaction front caused by pre-ignition in the upstream mixture significantly affects the overall front propagation speed.

2.5 Concluding remarks

The characteristics of auto-ignition, auto-ignitive deflagration and spontaneous propagation in a thermally stratified mixture are studied for a DME/air mixture using mean unburnt temperatures within and slightly above the NTC regime. Steady solutions for front propagation showed that the propagation speed scales proportionally to the level of upstream reactivity. As the characteristic residence time approaches the auto-ignition time scale, the deflagration front transitions to a spontaneous combustion regime with higher speeds. It is also found that the rise in propagation speed is faster for mixtures with a smaller ignition delay.

Results from unsteady simulations with imposed harmonic temperature oscillations show that the instantaneous propagation speed, S_c, is highly responsive to the stratification time scales representing the first- and second-stage homogeneous auto-ignition delay times. Consequently, there is a cyclic transition of the reaction front from auto-ignitive deflagration to spontaneous propagation. In the NTC regime, a sudden increase is observed in the instantaneous S_c of a coupled low-temperature and high-temperature double flame when

the stratification time scale approaches the first-stage homogeneous auto-ignition delay. It is found that this is caused due to the momentary coëxistence of deflagration and spontaneously propagating fronts. No such rapid rise is observed in the instantaneous S_c of a single high temperature flame outside the NTC regime, even when multiple fronts are found to co-exist simultaneously. However, the spontaneously propagating front lasts for a longer duration in this case. As a result, the peak instantaneous S_c of a single high-temperature flame outside the NTC regime is found to be substantially higher. Moreover, in each case, the peaks in instantaneous S_c coincide with the corresponding peaks in the cumulative reaction rate of OH radical which indicates that HTC is mainly responsible for the observed rise in instantaneous S_c. Additionally, based on the variation in the cumulative reaction rate of $CH_3OCH_2O_2$ radical in the NTC regime, it is found that LTC interacts with flow dynamics at sufficiently smaller time scales and becomes decoupled at larger time scales, similar to the observations in [56].

The present study demonstrates that the combustion behavior under modern IC engine conditions may exhibit intricate interplay between deflagration, auto-ignition, and spontaneous propagation modes, and the level of complexity depends on the length/time scales of fluctuations in temperature and composition within the reactant mixture, which affect the time scales of the flame-ignition interaction.

Chapter 3

Effects of composition and reactivity stratification on flame propagation at auto-ignitive conditions

In this chapter, front propagation speeds from fully resolved unsteady, one dimensional simulations with dimethyl-ether (DME)/methane (CH_4)/air mixtures under PCI engine-relevant conditions are presented using reduced kinetics and transport. Different time scales of monochromatic inhomogeneities in DME concentration with varying DME/CH_4 blending ratios are simulated to unravel the fundamental aspects of auto-ignition and flame propagation under the influence of reactivity stratification. To understand the influence of different stratification time scales on the flame-ignition interaction, two sets of conditions are simulated such that low-temperature chemistry is present in only one of them. The intrinsic effects of stratification time scales on the low-temperature chemistry and the high-temperature chemistry are further examined to assess the flame-ignition interaction. A displacement speed analysis is also carried out to elucidate the underlying combustion modes that are responsible for such a variation in flame response. In the present study, the binary fuel blend of dimethyl-ether (DME)/methane (CH_4) is selected as a model problem, since DME is one of the simplest fuel molecules that exhibits two-stage ignition, a characteristic exhibited by many practical hydrocarbon fuels. DME blended with CH_4, the main component of natural gas with its high anti-knock quality, has been shown to extend

the high-load limit of RCCI combustion [97]. Besides, stratification is imposed only in DME concentration since the low-reactivity fuel (i.e. CH_4) is typically premixed whereas the high-reactivity fuel (i.e. DME) is direct-injected in RCCI engines. As a result, CH_4 distribution is nearly uniform throughout the combustion chamber. The direct-injected DME then causes a distribution of the overall equivalence ratio ϕ_{overall}, defined in section 3.1, together with the uniform CH_4 distribution. The stratification of direct-injected, high-reactivity fuel (i.e. DME) in RCCI engines is controlled by adjusting the start-of-injection timing [12]. The large scale spatial stratification is represented by temporal fluctuations in DME concentration as the flame propagates into a stratified DME concentration field of a given length scale. One-dimensional parametric simulations are conducted, and the results are analyzed.

3.1 Numerical procedure and initial conditions

Fully resolved numerical simulations are performed using KARFS (KAUST Adaptive Reacting Flow Solver) [31] which solves the compressible Navier-Stokes, continuity, species and energy equations (see Appendix A). Spatial derivatives are approximated with an eighth-order finite-difference operator [24] along with a tenth-order explicit filter. Solution is advanced in time with a six-stage fourth-order Runge-Kutta method [25] using a constant time step size of 5 nanoseconds. A reduced DME chemical mechanism [23] consisting of 30 species and 175 reactions and an additional 9 species identified as global quasi-steady state species is used in the present study. Previous studies [47–49] have demonstrated that the detailed DME model [44] is able to accurately reproduce the flame speeds and ignition delay times of DME/air, CH_4/air and DME/CH_4/air mixtures for a wide range of operating conditions. For the blending ratios of DME/CH_4 that have been used in the present study, the relative difference between the steady propagation speed and the two homogeneous ignition delay times obtained using both the detailed and the reduced mechanism is found to be less than 4%.

For the binary fuel blend, the blending ratio c is defined as:

$$c = \frac{Y_{CH_4}}{Y_{DME} + Y_{CH_4}} \tag{3.1}$$

To investigate the effects of blending ratio, c, and stratification time scale, τ_0, on the front propagation speed, one-dimensional simulations are conducted for two different mean unburned temperature conditions at T_0=800 and 1000 K, denoted as LT (low temperature) and HT (high temperature) cases. For each temperature condition, three blending ratios of 0, 25, and 37.5 % are considered. Details of the important numerical and physical quantities for the six cases under study are summarized in Table 3.1. Case labels with prefix LT represent the cases involving both low-temperature chemistry (LTC) and high-temperature chemistry (HTC) whereas those with prefix HT represent cases involving only HTC. Number in each of the case labels indicates the % blending ratio. S is the steady propagation speed and L is the corresponding domain length. T_b indicates the burned gas temperature in each case. At the present unburned conditions, the difference in the equilibrium gas temperature under constant enthalpy and pressure for a pure CH_4/air mixture (c=1) and a pure DME/air mixture (c=0) is found to be only 70 K as the heat of combustion of CH_4 and DME are comparable. As a result, there is no substantial effect of the different blending ratios on the burned gas temperature. In each case, the uniform grid resolution $\triangle$x corresponds to a minimum of 12 grid points across the thinnest species reaction rate layer (CH_3O in cases with LTC and C_2H_2 in cases without LTC) in the combustion front. The mean pressure is set at 40 atm in all cases.

For the six cases considered, the baseline calculations are carried out as follows. Constant-pressure homogeneous ignition calculations were made to identify the characteristic ignition-delay times. Figure 3.1(a) shows the temporal evolution of temperature. Clearly, most of the cases show multi-stage ignition, which is notably different than two-stage heat release typically reported for stoichiometric fuel/air mixtures. The three-staged DME auto-ignition has also been previously reported by Oshibe et al. [46]. Moroever, in a recent study by

Table 3.1: Physical and numerical parameters used in LTC and HTC cases

Case	τ_1 (ms)	τ_2 (ms)	λ_1 (mm)	λ_2 (mm)	S (m/s)	T_b (K)	L (mm)	c	$\triangle$x (μm)	ϕ_{DME}	$\phi_{\mathrm{CH_4}}$	ϕ_{overall}
LT0	**0.37**	**1.18**	**0.69**	**2.98**	**2**	**1770**	**8**	**0**	**3.4**	**0.4**	**0**	**0.4**
LT25	**0.39**	**2.13**	**0.68**	**5.61**	**2**	**1753**	**10**	**0.25**	**5.3**	**0.3**	**0.1**	**0.4**
LT37.5	**0.41**	**3.34**	**0.7**	**8.95**	**2**	**1745**	**20**	**0.375**	**7**	**0.25**	**0.15**	**0.4**
HT0	**-**	**1.05**	**-**	**2.20**	**2**	**1950**	**5**	**0**	**2.15**	**0.4**	**0**	**0.4**
HT25	**-**	**1.46**	**-**	**3.13**	**2**	**1933**	**6**	**0.25**	**2.17**	**0.3**	**0.1**	**0.4**
HT37.5	**-**	**1.84**	**-**	**4.00**	**2**	**1924**	**10**	**0.375**	**2.25**	**0.25**	**0.15**	**0.4**

Sarathy et al. [98], lean n-heptane/air mixtures were also found to exhibit three-stage heat release at high pressures and low-to-intermediate temperatures. Hence, the observed multi-stage ignition is not an artifact of the kinetic model employed herein. Note that in most of the LT cases, second- and main-stage ignition delay times are of the same order as opposed to first and main. Similarly, in cases HT25 and HT37.5, there is a negligible difference between the second- and main-stage ignition delay times. Meanwhile, intermediate (i.e. second-stage) ignition is visibly absent from case HT0. It is also seen that the LT cases involve low-temperature ignition (during which the rise in temperature is the smallest) whereas the HT cases do not. In the present study, the first- and main-stage ignition delay times are denoted as τ_1 and τ_2, respectively, defined based on the instants of maximum heat release. Figure 3.1(b), on the other hand, shows the final steady flame solutions obtained from Cantera [1], where $S = 2$ m/s and λ_1 and λ_2 denote the locations of the cool and hot flames, defined based on the spatial location of maximum heat release. Again, the low-temperature ignition is observed for all LT cases. Note that, as c is increased, τ_2 and λ_2 increase considerably due to the lower reactivity of methane, whereas τ_1 and λ_1 remain mostly unaffected, as they are inherent properties of DME. In Figure 3.1(c), the spatial temperature distributions in the respective cases as depicted in Figure 3.1(b) are transformed to temporal evolution (dotted lines) by the operator:

$$t(X) = \int_0^X dx/u(x) \tag{3.2}$$

where $u(x)$ is the local flow velocity. Comparison with the homogeneous ignition (solid lines) results presented in Figure 3.1(a) indicate that transport should have little effect on the front propagation in all the respective cases since both the temporal profiles overlap each other as previously demonstrated in Ref. [99]. However, a transport budget analysis presented in section 3.2 indicates that diffusion has a non-negligible contribution to front propagation.

Additionally, sensitivity analysis of first- and main-stage ignition delays to temperature was carried out using constant-pressure, adiabatic kinetic simulations for determining the most dominant reactions at each stage. Reactions with a negative sensitivity to temperature

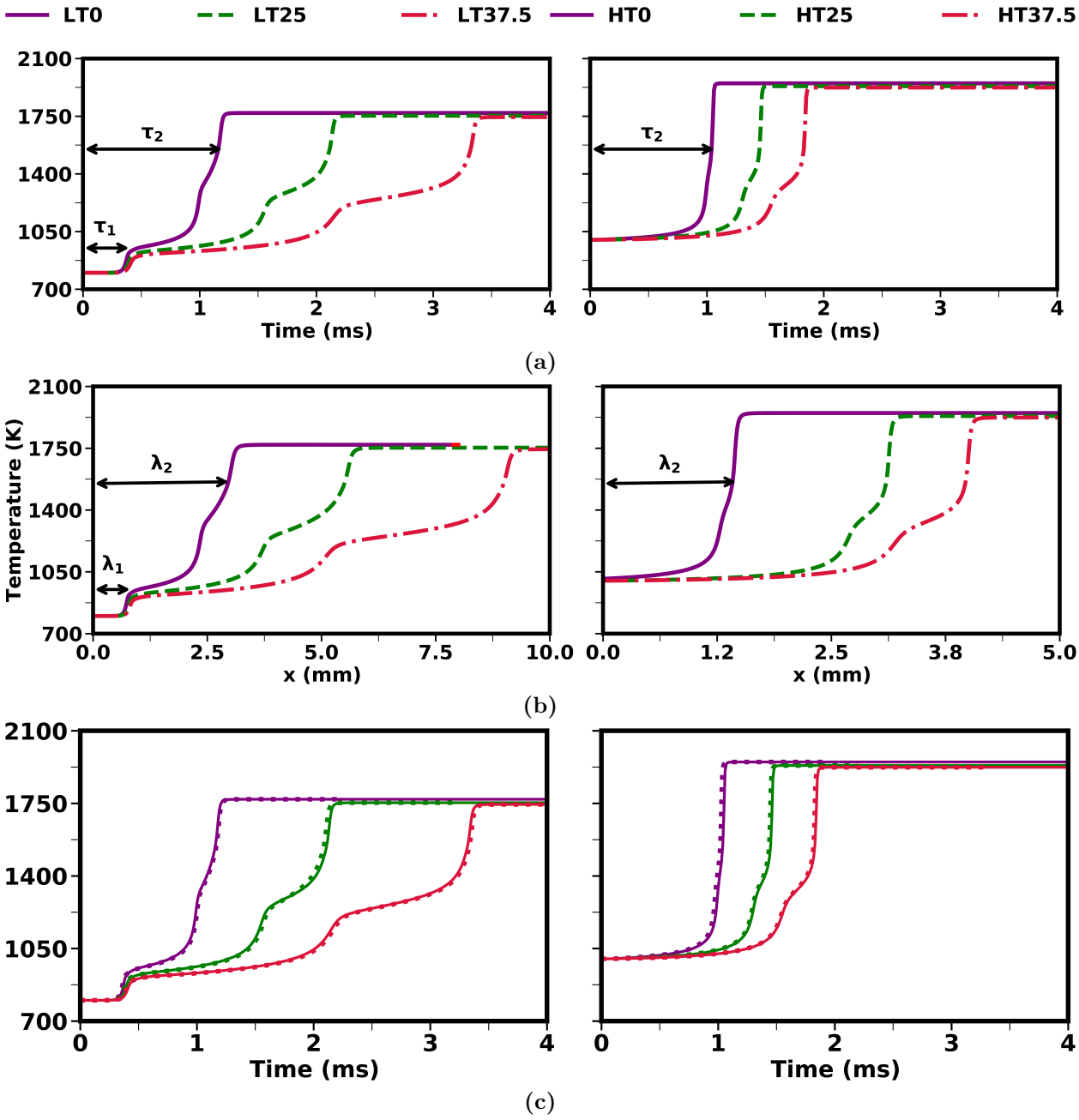

Figure 3.1: (a) Temporal temperature evolution for homogeneous ignition, (b) spatial temperature distribution and (c) temporal evolution from (a) shown as solid lines along with the spatial temperature distribution from (b) transformed to a temporal evolution and shown as dotted lines for the six cases under study. The ordinate axis range is the same on each row of sub-figures and hence omitted.

tend to delay the ignition whereas reactions with a positive sensitivity to temperature tend to advance it. It is found that the four most dominant reactions at the first-stage ignition are identical in the respective LT cases as shown in Figure 3.2 (a). Only the magnitude of sensitivity of the respective reactions is noticed to reduce with an increase in the amount of CH_4 concentration in the binary fuel blend. At the same time, the majority of the reactions at main stage ignition in the respective LT and HT cases are also the same as depicted in Figure 3.2 (b) and Figure 3.2 (c), albeit with differences in magnitudes of sensitivity. A similar observation was made for the most dominant reactions at the second-stage ignition in the different LT and HT cases. Therefore, in the present study, only the first- and the main-ignition stages in the respective cases have been identified to facilitate a better comparison between the obtained results for the different cases.

To identify a reference laminar flame speed, S_R, the method proposed in [21] was followed. A series of steady-state flame solutions were evaluated in Cantera [1] by varying the flame position, λ_2 (based on the location of maximum heat release rate), for which the correct inflow velocity, U_{in} was determined as an eigenvalue. Figure 3.3 presents λ_2 as a function of U_{in}. The derivative $d\lambda_2/dU_{in}$ vs. U_{in} is also shown. Distinguishable peaks in $d\lambda_2/dU_{in}$ at specific values of inlet velocity can be clearly identified in the respective cases. These results are consistent with those presented in Ref. [21], wherein multiple peaks in $d\lambda_2/dU_{in}$ were obtained for a two-staged reaction front. As such, for reaction fronts with multi-staged ignition, multiple reference flame speeds under auto-ignitive conditions can be expected. As per the argument provided in [21], the inlet velocity where $d\lambda_2/dU_{in}$ becomes maximum corresponds to S_R. Based on that criterion, the reference laminar flame speeds identified in the respective cases are listed in Table 3.2.

For the range of U_{in} investigated in the present study, multiple values of S_R were identified in all the LT cases and case HT0. In case LT37.5, the first peak in $d\lambda_2/dU_{in}$ occurred at 0.15 m/s (not visible). However, the magnitude of $d\lambda_2/dU_{in}$ at the next peak which occurred at 2.95 m/s far exceeded the first one. Since, the reference laminar flame speed at auto-ignitve conditions is identified solely based on maximum $d\lambda_2/dU_{in}$, 2.95 m/s was identified as the first reference laminar flame speed in case LT37.5. The most probable reason for this discrepancy, compared to the other cases, could be the larger separation between the

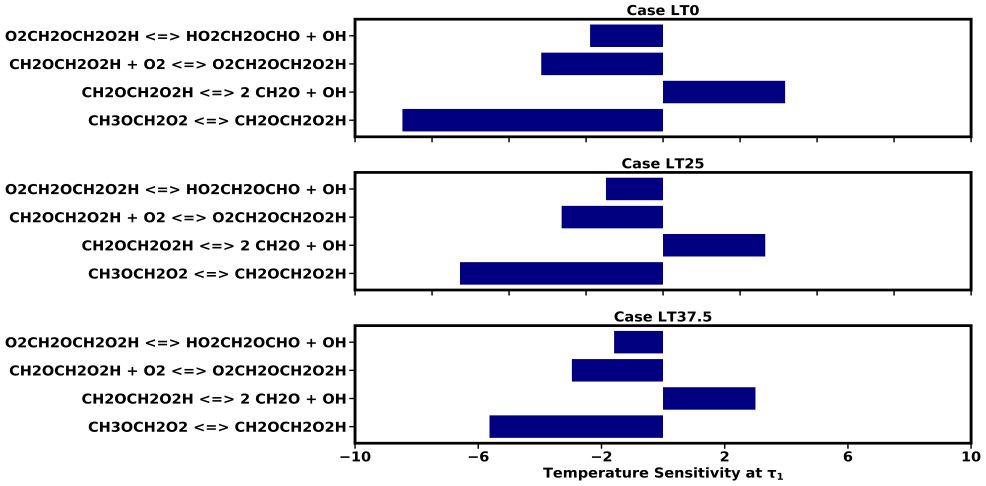

(a)

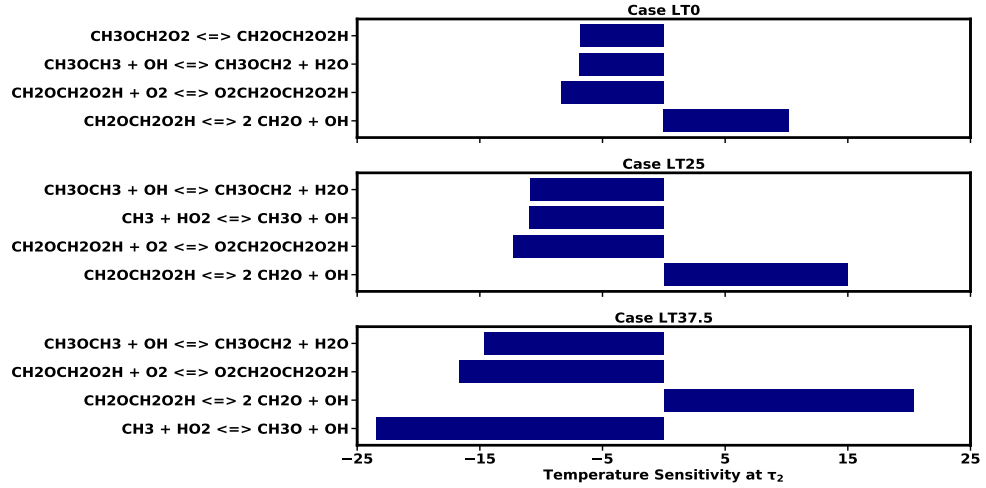

(b)

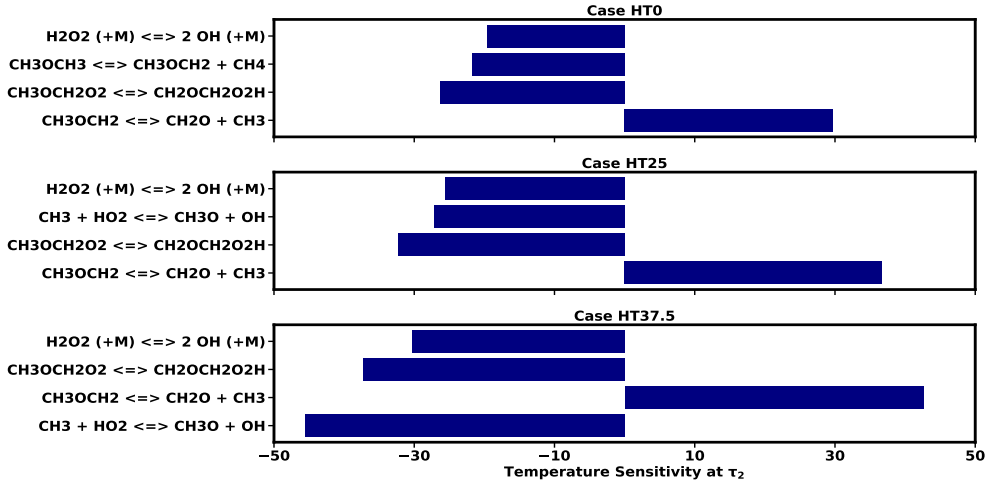

(c)

Figure 3.2: The four most dominant reactions at (a) first-stage ignition in the LT cases, (b) main-stage ignition in the LT cases and (c) main-stage ignition in the HT cases

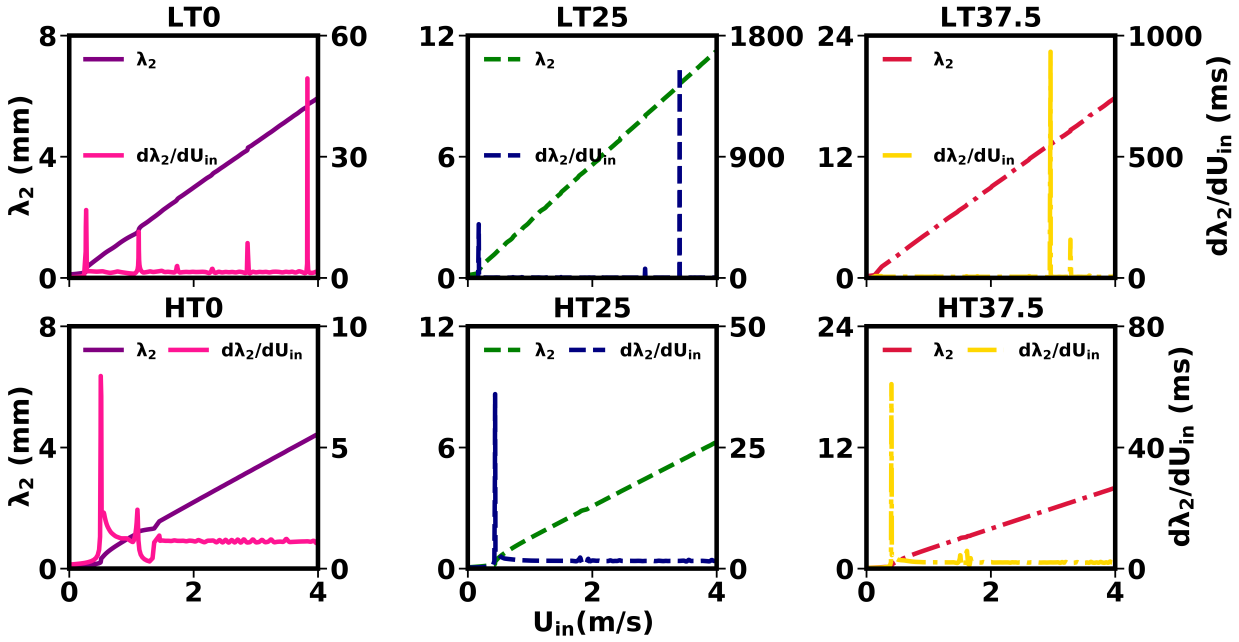

Figure 3.3: Position of the hot reaction front away from the inlet, λ_2, and derivative of the hot ignition front position with respect to the inlet velocity, $\mathrm{d}\lambda_2/\mathrm{d}U_{\mathrm{in}}$, vs. inlet velocity, U_{in}

Table 3.2: Reference flame speeds in the respective cases

Case	S_{R} (m/s)
LT0	**0.28, 1.12, 3.83**
LT25	**0.17, 3.41**
LT37.5	**2.95, 3.29**
HT0	**0.51, 1.1**
HT25	**0.44**
HT37.5	**0.41**

different ignition delays and how this spatial separation changes with respect to a change in the inlet velocity. Moreover, reaction fronts with $S < 1$ m/s resulted in flames attached to the inlet in the LT cases. Such burner attached flames could not be used in the present study due to interference with the imposed boundary conditions. Hence, a reaction front with $S = 2$ m/s as an initial condition in the unsteady cases is apt for the present study, which is also of the same order as that of the reference laminar flame speed at auto-ignitive conditions estimated in [21].

To perform a direct comparison of the flame response to the imposed stratification in the presence/absence of low-temperature chemistry, $S = 2$ m/s was purposefully chosen for the HT cases as well (even though S_{R} is much smaller in the HT cases). This choice is also supported via the transport budget analysis presented in section 3.2. Note that the present steady-state 1D calculations were carried out with significant care to avoid any spurious numerical errors. The spikes in the LT and HT results are a consequence of a very fine increase in λ_2 during each subsequent steady flame calculation and not due to numerical errors.

For the unsteady calculations, a selected steady solution shown in Figure 3.1 (b) is used as the initial condition, while the inflow DME concentration is varied in time as:

$$Y_{\mathrm{DME}}(t) = Y_{\mathrm{DME}}(t) + A\sin\left(\frac{2\pi t}{\tau_0}\right) \tag{3.3}$$

and at all times the deficit or excess of DME concentration is compensated for by adjusting the air concentration in cases LT0 and HT0 and by adjusting the air as well as CH_4 concentration in the remaining cases. In Equation 3.3, A is the amplitude, t is time and τ_0 is the period of oscillation. Non-reflective boundary conditions are imposed at the inlet and the outlet to avoid large pressure waves within the domain as described in Ref. [88]. Due to open boundaries, the thermodynamic pressure remains constant, thereby allowing a statistically stationary limit cycle behavior to be produced for the unsteady cases.

Since binary fuel blends make it difficult to define the mixture fraction or equivalence ratio unambiguously, three different equivalence ratios are defined as per the previous approaches

[12, 23]. The equivalence ratio with respect to DME and CH_4 are computed as:

$$\phi_{\mathrm{DME}} = \nu_{\mathrm{DME}} \frac{Y_{\mathrm{DME,u}}}{Y_{\mathrm{O_2,u}}} \tag{3.4}$$

$$\phi_{\mathrm{CH_4}} = \nu_{\mathrm{CH_4}} \frac{Y_{\mathrm{CH_4,u}}}{Y_{\mathrm{O_2,u}}} \tag{3.5}$$

where ν_{DME} and $\nu_{\mathrm{CH_4}}$ are the stoichiometric oxygen-to-fuel mass ratios for the respective fuels [100]. $Y_{\mathrm{DME,u}}$, $Y_{\mathrm{CH_4,u}}$ and $Y_{\mathrm{O_2,u}}$ are the unburned mass fractions of DME, CH_4 and O_2 respectively. Equations 3.4 and 3.5 assume that all of the local oxygen is available to react with both fuels, which is not the case in real operating conditions. Therefore, they do not necessarily represent the equivalence ratios in a strict sense, but rather indicate the normalized concentrations of DME and CH_4, respectively. Additionally, an overall equivalence ratio, ϕ_{overall}, is computed at every grid point from the mixture fraction, ξ, which is evaluated as:

$$\xi = \frac{\frac{1}{2}\left(\frac{Z_{\mathrm{H}} - Z_{\mathrm{H,air}}}{M_{\mathrm{H}}}\right) + 2\left(\frac{Z_{\mathrm{C}} - Z_{\mathrm{C,air}}}{M_{\mathrm{C}}}\right) - \left(\frac{Z_{\mathrm{O}} - Z_{\mathrm{O,air}}}{M_{\mathrm{O}}}\right)}{\frac{1}{2}\left(\frac{Z_{\mathrm{H,fuel}} - Z_{\mathrm{H,air}}}{M_{\mathrm{H}}}\right) + 2\left(\frac{Z_{\mathrm{C,fuel}} - Z_{\mathrm{C,air}}}{M_{\mathrm{C}}}\right) - \left(\frac{Z_{\mathrm{O,fuel}} - Z_{\mathrm{O,air}}}{M_{\mathrm{O}}}\right)} \tag{3.6}$$

In Equation 3.6, Z_{H}, Z_{C} and Z_{O} are the elemental mass fractions of hydrogen, carbon and oxygen at a given grid point, respectively. Similarly, $Z_{\mathrm{H,fuel}}$, $Z_{\mathrm{C,fuel}}$ and $Z_{\mathrm{O,fuel}}$ are the elemental mass fractions of hydrogen, carbon and oxygen in the binary fuel blend whereas $Z_{\mathrm{H,air}}$, $Z_{\mathrm{C,air}}$ and $Z_{\mathrm{O,air}}$ are the elemental mass fractions of hydrogen, carbon and oxygen in air. M_{H}, M_{C} and M_{O} are the atomic weights of hydrogen, carbon and oxygen, respectively. Once ξ is evaluated, the overall equivalence ratio, ϕ_{overall}, is computed as:

$$\phi_{\mathrm{overall}} = \frac{1/\xi_{\mathrm{st}} - 1}{1/\xi - 1}, \tag{3.7}$$

where

$$\xi_{\mathrm{st}} = \frac{\frac{Z_{\mathrm{O,air}}}{M_{\mathrm{O}}} - \frac{1}{2}\left(\frac{Z_{\mathrm{H,air}}}{M_{\mathrm{H}}}\right) - 2\left(\frac{Z_{\mathrm{C,air}}}{M_{\mathrm{C}}}\right)}{\frac{1}{2}\left(\frac{Z_{\mathrm{H,fuel}} - Z_{\mathrm{H,air}}}{M_{\mathrm{H}}}\right) + 2\left(\frac{Z_{\mathrm{C,fuel}} - Z_{\mathrm{C,air}}}{M_{\mathrm{C}}}\right) - \left(\frac{Z_{\mathrm{O,fuel}} - Z_{\mathrm{O,air}}}{M_{\mathrm{O}}}\right)} \tag{3.8}$$

ξ_{st} in Equation 3.8 is the stoichiometric mixture fraction. The overall equivalence ratio, ϕ_{overall}, computed using Equation 3.7 is identical to the equivalence ratio definition that is typically used in single-fuel systems.

As demonstrated in Ref. [9], a larger concentration of the high-reactivity fuel results in a greater tendency of deflagrative flame propagation. As such, ϕ_{DME} is intentionally kept higher than $\phi_{\mathrm{CH_4}}$ in each case as noted in Table. 3.1. It is expected to further promote deflagration as the dominant mode of propagation under unsteady conditions. For the LT cases, calculations are carried out with DME concentration stratification at six different timescales i.e. $\tau_0 = \tau_1/2, \tau_1, 2\tau_1, \tau_2/2, \tau_2, 2\tau_2$. Similarly, for the HT cases, simulations are performed with DME concentration stratification at three different timescales i.e. $\tau_0 = \tau_2/2, \tau_2, 2\tau_2$. The temporal variation in DME concentration at the inlet translates into pockets of stratified composition field due to flow advection. The frequency of oscillation along with the inlet flow velocity determines the characteristic length scale of stratification, which is of the same order as recently measured in an optical IC engine [90]. The amplitude of stratification in DME concentration, A, is selected such that there is sufficient flame response while ensuring stability and avoiding flame blow-off. Specifically, in cases LT0, LT25 and LT37.5,

$$A = \begin{cases} 0.06, & \tau_0 = \tau_1/2, \tau_1, 2\tau_1 \\ 0.02, & \tau_0 = \tau_2/2, \tau_2, 2\tau_2 \end{cases} \tag{3.9}$$

and in cases HT0, HT25 and HT37.5,

$$A = 0.06,\ \tau_0 = \tau_2/2, \tau_2, 2\tau_2. \tag{3.10}$$

Note that the purpose of the present investigation is not to reproduce the exact conditions from a specific set of engine experiments, but rather to reproduce a possible evolution of front propagation speeds under the influence of fuel reactivity stratification induced by direct injection at different length scales. In addition, even though fuel reactivity stratification usually affects the corresponding distribution of temperature, it has been neglected in the present study to solely investigate flame dynamics at auto-ignitive conditions under the influence of reactivity stratification.

3.2 The steady flame behavior

Previous studies have evaluated the steady front propagation speed at auto-ignitive conditions under the influence of varying inlet temperature [101] and inlet flow velocity [21]. In the present study, the steady-state analysis is carried out mainly for assessing the rise in S with respect to the high-temperature flame location, λ_2. Figure 3.4 shows the dependence of S on λ_2. For a given λ_2, S is determined as an eigenvalue in Cantera [1]. For all cases, S increases linearly with λ_2. Specifically, S increases from 2 m/s to $\approx$ 3.5 m/s as the reaction front is moved from points F1, F2, F3, F7, F8 and F9 to points F4, F5, F6, F10, F11 and F12, respectively. For both temperature conditions, S increases at the fastest rate for the 100% DME case (LT0 and HT0). Between the two, the rate of change of S with λ_2 in the HT0 case is much larger, which is attributed to its lower τ_2 at higher temperature resulting in a lower characteristic flow-through time, τ_f ($= \int_0^{\lambda_2} \frac{1}{u(x)}\, dx$, where $u(x)$ is the local flow velocity), which is required for the upstream mixture to auto-ignite and enter the spontaneous propagation regime before it reaches the flame. This finding is also consistent with the observations in [77].

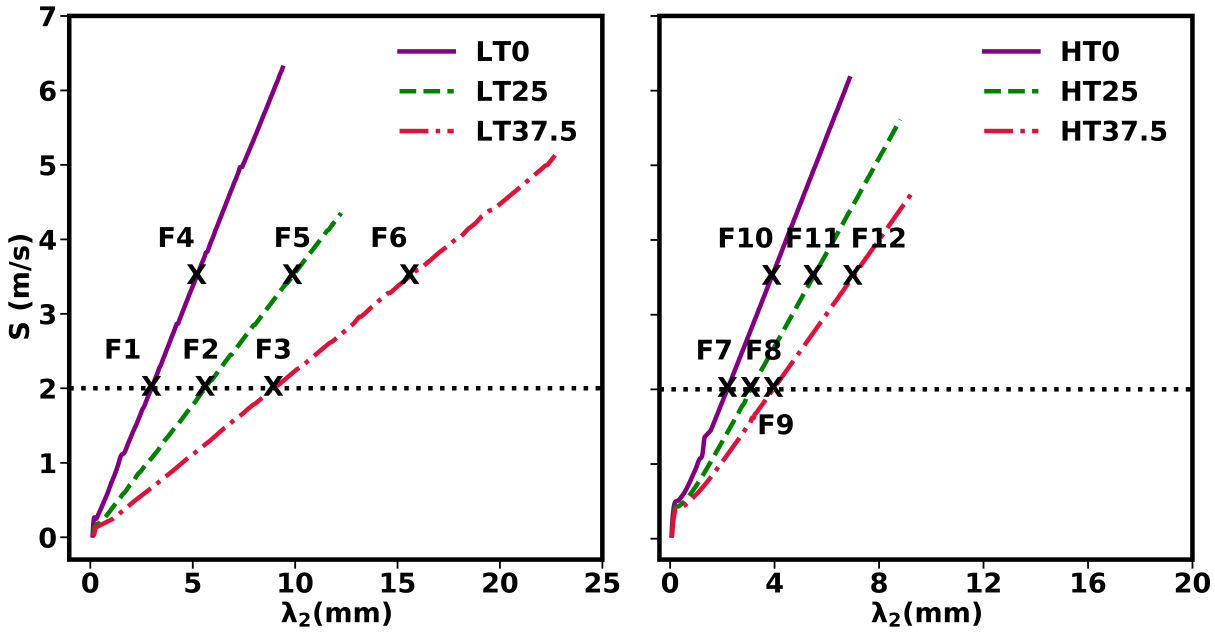

Figure 3.4: Variation in S with λ_2 for the respective cases. The horizontal dotted line corresponds to $S = 2$ m/s. The ordinate axis range in the right sub-figure is the same and hence omitted.

For distinguishing the combustion modes at the points marked in Figure 3.4, the reaction and diffusion rates of species O_2 are evaluated as shown in Figure 3.5. At all conditions, the reaction term is found to be much higher than the diffusion term, suggesting that the mixture upstream of the front is highly reactive due to preheating. The diffusion term, however, is not negligible across the reaction fronts, as shown by the peaks. Between the left and right columns of the figures, the magnitude of the diffusion term diminishes consistently as the front speed increases (at $S \approx 3.5$ m/s). The results are consistent with the findings in [94] wherein the absolute value of reaction term was 5 times larger than the diffusion term. It also supports the observations in [21, 56] where the transition from deflagration to spontaneous propagation usually required an order of magnitude increase in the inlet velocity. Hence, it is concluded that diffusive transport plays a role in accelerating the combustion even when the mode of propagation is nearly spontaneous. To this end, the reaction front at points F1, F2, F3, F7, F8 and F9 are classified to be in the auto-ignition-assisted deflagration regime as per the definition used in [21].

3.3 Response to unsteady DME concentration fluctuations

In this section, the effect of imposed monochromatic oscillation in DME concentration on the front propagation speed is presented. The steady flame solutions at points F1, F2, F3, F7, F8 and F9 with a constant $S = 2$ m/s depicted in Figure 3.4 are used as an initial condition in the respective cases. The initial temperature profiles of these reaction fronts were shown in Figure 3.1. The amplitude of stratification at the inlet in the respective cases is imposed following equations 3.9 and 3.10. Considering the unsteady nature, the flame-speed variations are examined in terms of the consumption speed based on O_2, defined as [100]:

$$S_c = -\frac{1}{\rho_u (Y_{O_2,u} - Y_{O_2,b})} \int_0^L \dot{\omega}_{O_2} \, dx \tag{3.11}$$

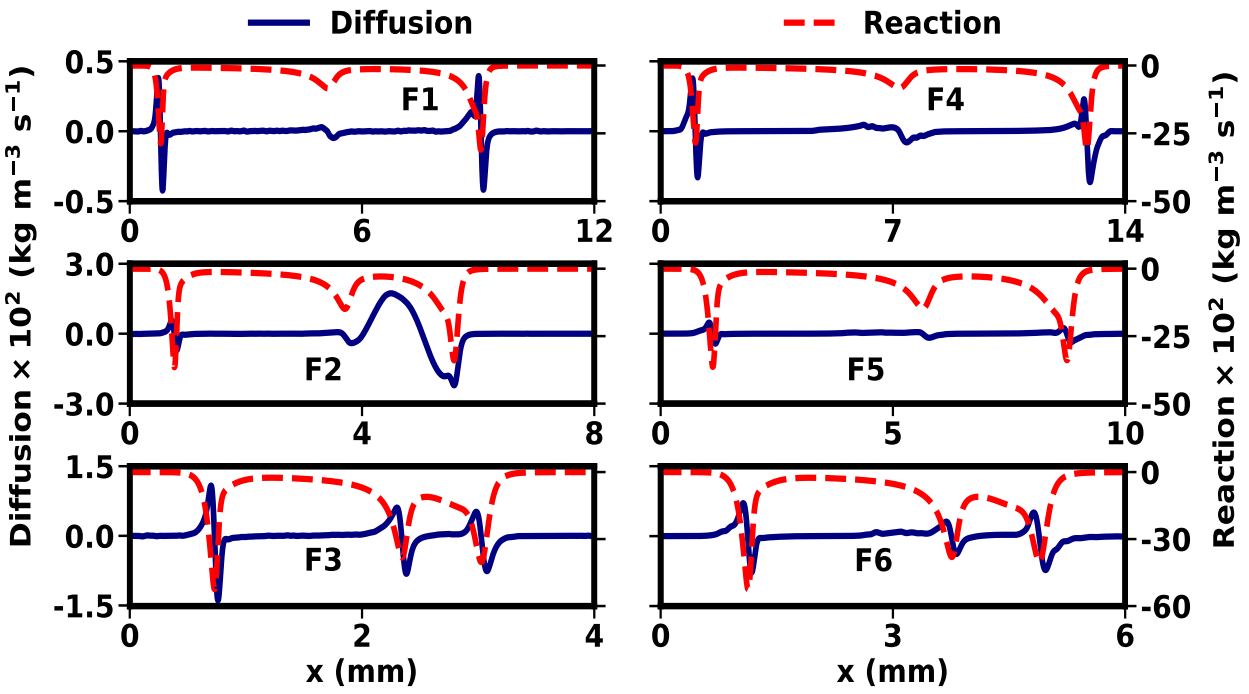

(a)

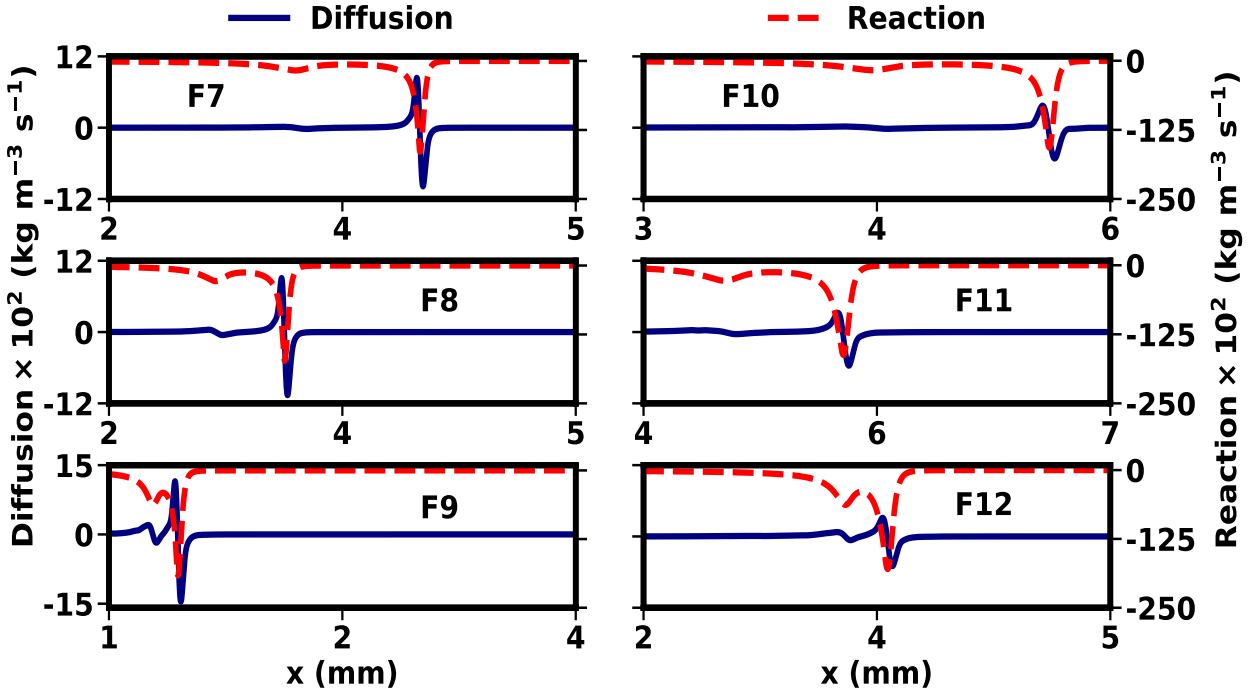

(b)

Figure 3.5: Reaction-diffusion balance for (a) Cases LT0, LT25 and LT37.5, (b) Cases HT0, HT25 and HT37.5. In each of the sub-figures, the y-axis on the left shows the magnitude of diffusion (Diffusion_{O_2}) (solid line) while the one on the right shows the magnitude of reaction (Reaction_{O_2}) (dashed line). The ordinate axis range on each row of sub-figures is the same and hence omitted.

where ρ_u is the unburned gas density, $Y_{O_{2,u}}$ and $Y_{O_{2,b}}$ are the mass fractions of oxygen in the unburned and burned gas, respectively, and $\dot{\omega}_{O_2}$ is the oxygen reaction rate.

Figure 3.6 shows the unsteady S_c as a function of overall equivalence ratio, $\phi_{overall}$, at the inlet after a limit cycle is reached in each case. It is clearly seen that the variation in S_c with respect to $\phi_{overall}$ is not harmonic but rather shows hysteretic behavior as previously observed [56, 77, 95]. However, unlike the observation in [77], there is negligible flame response at the smallest time scale ($\tau_1/2$) in all the LT cases. As τ_0 is increased, the limit cycle exhibits a complex shape with peaks which are similar to the observations of [77] and different from the elliptical shapes observed in [56, 95]. The overall variation in instantaneous S_c gradually subsides with an increase in c for $\tau_0 \leq 2\tau_1$ in the LT cases. This is evident from the flame response at $\tau_0 = \tau_1$ and $\tau_0 = 2\tau_1$ in case LT25 compared to case LT0. Further increase in c shows an even higher suppression of the dynamic response, as noticed in case LT37.5. These observations provide further insight into the effect of increasing blending ratio which was not investigated in [77]. In contrast, for $\tau_0 > 2\tau_1$, the peak and overall amplitude of the unsteady response rises with an increase in c, at all values of $\tau_0 = \tau_2/2$, τ_2, and $2\tau_2$. These observations are again found to be significantly different from those observed in [77]. The dynamic flame response in the HT cases is found to be qualitatively similar to that observed for the LT cases at $\tau_0 = \tau_2/2, \tau_2, 2\tau_2$. Therefore, the unsteady response at time scales related to the hot flames appears consistent. However, for an identical A = 0.06, the peak S_c in the HT cases is seen to be substantially higher compared to that in the LT cases, even though the mean S_c is the same for both sets of conditions.

To explain the contrasting unsteady response in the LT and HT cases, the effect of τ_0 relative to the corresponding characteristic time scales, τ_1 and τ_2, needs to be examined. The key intermediate species in the low-temperature ignition process is the methoxy-methyl-peroxy ($CH_3OCH_2O_2$) radical [42, 44], while one of the main species in the high-temperature ignition process of methane is the methyl (CH_3) radical [102]. The methyl radical is also found to be produced/consumed during the first-stage and the end-stage ignition of an unblended DME/air mixture [44]. Therefore, the reaction rates of these radical species are monitored, in terms of their total integrated quantity, $\dot{\Omega}_k = \int_0^L \dot{\omega}_k \, dx$, where $\dot{\omega}_k$ is the reaction rate of species k.

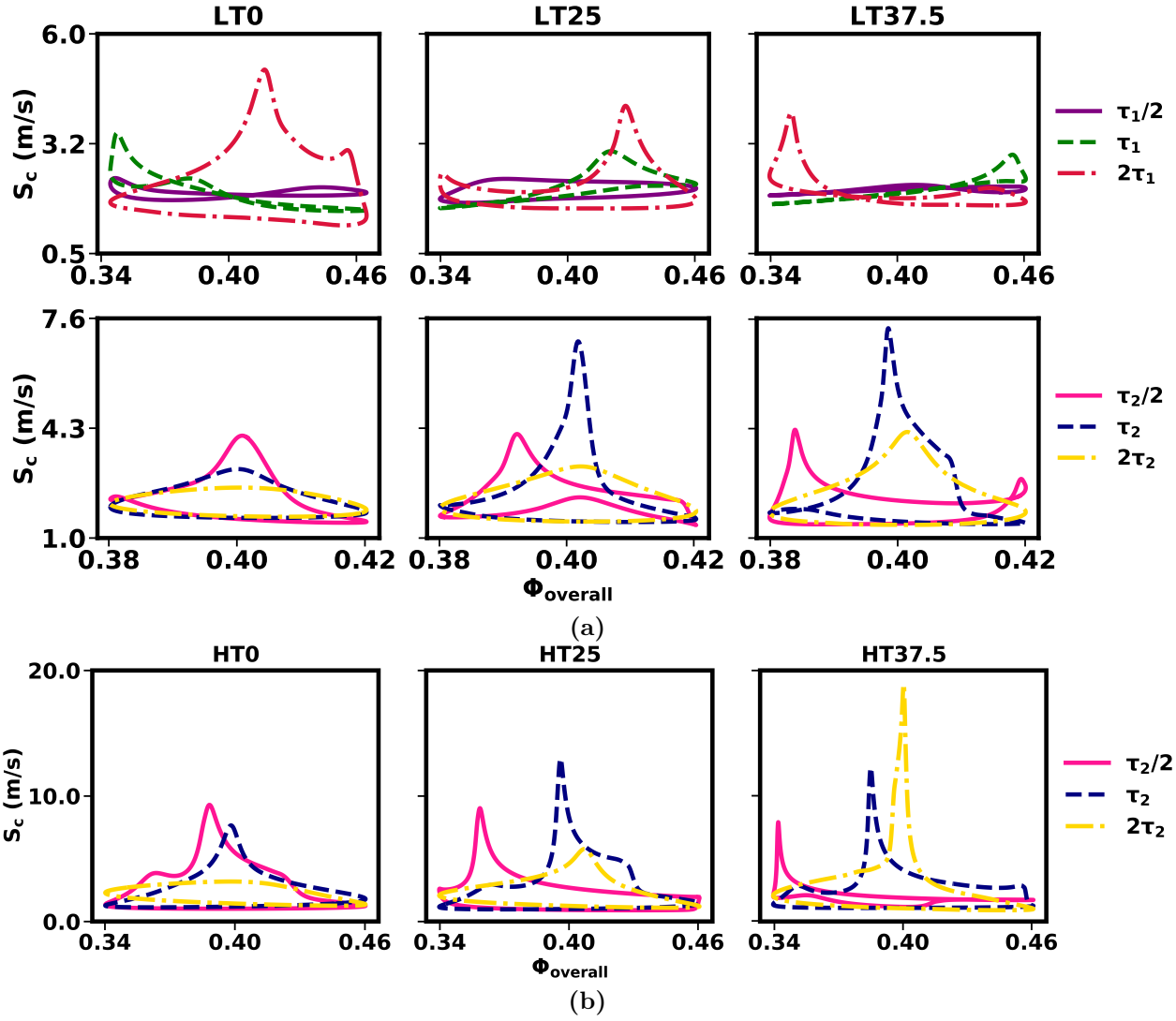

Figure 3.6: Variation in S_c with $\phi_{overall}$ at the inlet for different τ_0 in (a) cases LT0, LT25 and LT37.5, (b) cases HT0, HT25 and HT37.5. The ordinate axis range on each row of sub-figures is the same and hence omitted.

Figure 3.7 shows the temporal evolution of the instantaneous propagation speed and key radical reaction rates for the three blending ratios at different τ_0 in the LT cases. The time axis is normalized by τ_0 and two cycles after reaching the limit-cycle behavior are shown. It is seen that, irrespective of the blending ratio, c, the LTC reaction rate exhibits nearly a sinusoidal shape. As τ_0 is increased, the amplitude of fluctuation diminishes noticeably, indicating that LTC becomes progressively non-responsive to unsteady fluctuations as τ_0 is increased. In contrast, the variation in S_c is neither found to be sinusoidal nor in synchronization with $\dot{\Omega}_{CH_3OCH_2O_2}$. Hence, it is concluded that the effect of LTC on S_c is minimal.

On the other hand, the spikey responses in S_c coincide more with the reaction rate of the methyl radical, a representative of HTC characteristics, in terms of their temporal phasing, the attenuation of the amplitude with an increase of τ_0 from $\tau_1/2$ to $2\tau_1$, and the increase in the amplitude with an increase of τ_0 from $\tau_2/2$ to $2\tau_2$. This suggests that, at both LT and HT conditions, the flame speed depends more strongly on the HTC process which dictates the ultimate heat-release characteristics. Hence, it is concluded that HTC is mainly responsible for the observed variation in dynamic response as well as the rise in instantaneous S_c.

The corresponding analysis is performed for the HT cases i.e. HT0, HT25 and HT37.5, and the results are shown in Figure 3.8. In the absence of LTC, it is evident that the S_c response is directly correlated with the reaction rate of the methyl radical, in terms of both phasing and amplitude. Similar correlations between S_c and the reaction rate of the hydroxyl (OH) radical have been obtained in LT as well as HT cases. These findings are also consistent with those in [77]. While Figures 3.7 and 3.8 provide qualitative correlation between S_c and the reaction rate of the methyl radical, Figures 3.9 (a) and (b) provide quantification of this correlation. Interestingly, in all the cases, the limit-cycle behavior of $\dot{\Omega}_{CH_3}$ with respect to S_c exhibits a helical shape. Compared to the larger time scales, the dynamical response exhibits a narrow range of instantaneous S_c at smaller time scales, in both LT and HT cases. This observation indicates that HTC gets increasingly more responsive with an increase in stratification time scale which in turn affects the overall variation in instantaneous S_c. $\dot{\Omega}_{CH_3}$ is found to be positive at smaller values of S_c, in both LT and HT cases. This is suggestive of production of the methyl radical which is found to be significantly dependent on the imposed

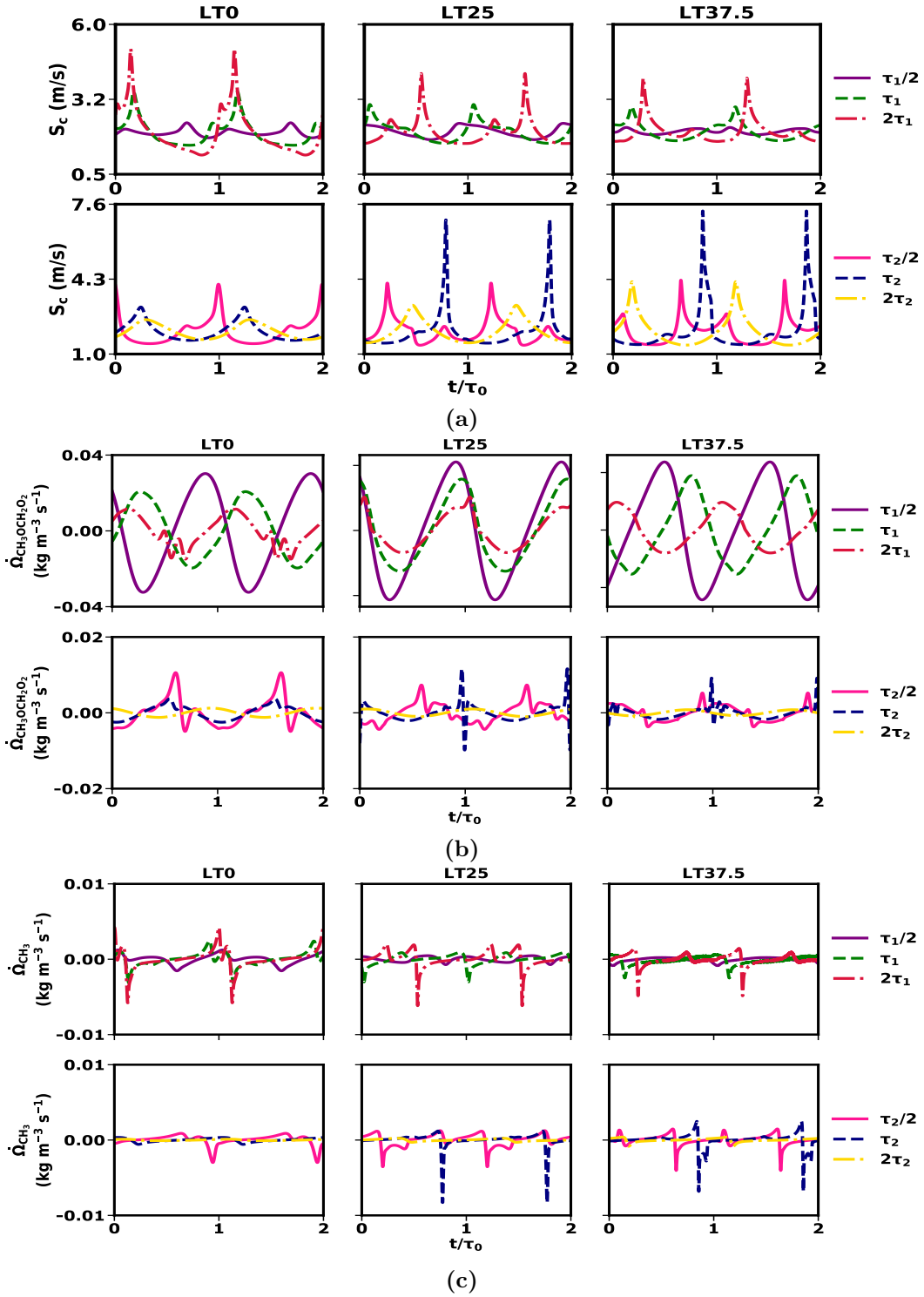

Figure 3.7: Effect of oscillation frequency in DME concentration on a) S_c, b) LTC, c) HTC in cases LT0, LT25 and LT37.5. The ordinate axis range on each row of sub-figures is the same and hence omitted.

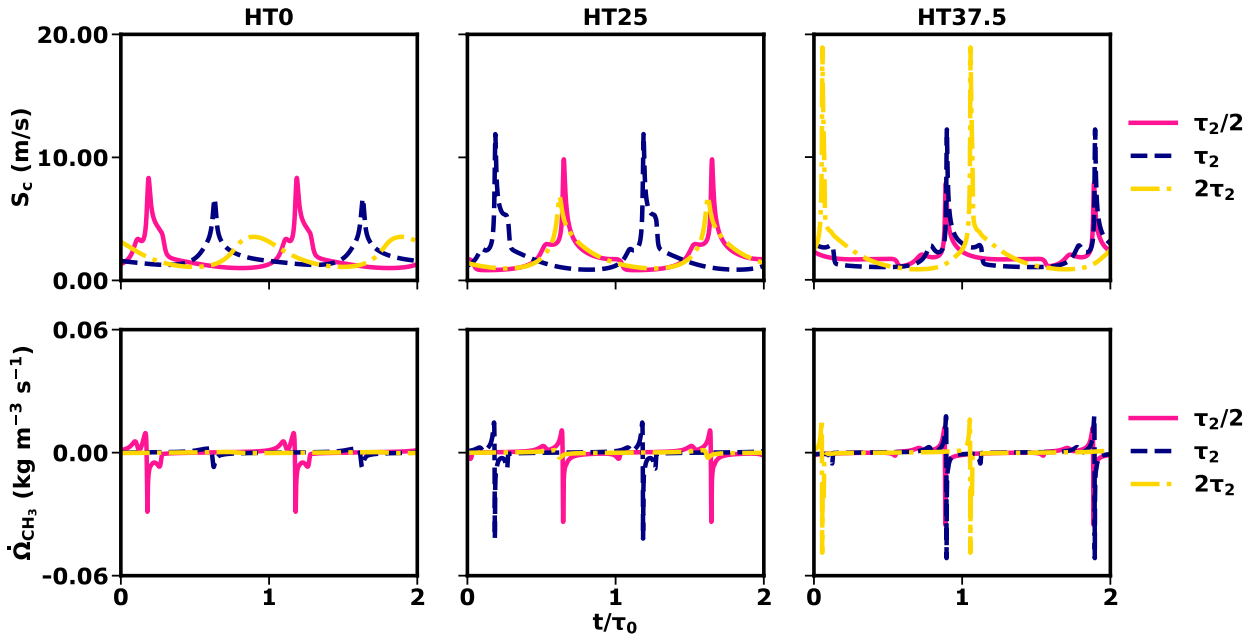

Figure 3.8: Effect of oscillation frequency in DME concentration on S_c and HTC in cases HT0, HT25 and HT37.5. The ordinate axis range on each row of sub-figures is the same and hence omitted.

stratification time scale. However, $\dot{\Omega}_{CH_3}$ becomes negative at larger values of S_c which is indicative of consumption of the methyl radical. As such, the observed rise in instantaneous S_c is mainly driven by the amount of CH_3 consumption at a given time scale. These results indicate that CH_3 production tends to slow down the reaction front whereas its consumption tends to accelerate it.

3.4 Identification of combustion modes

Thus far, S_c has been used to represent the *global* propagation speed of a reaction front exhibiting characteristics of both auto-ignition and deflagration. However, a density weighted displacement speed, S_d is a more appropriate *local* metric to identify the distinct characteristics of multiple reaction fronts and their respective speeds. The displacement speed S_d is defined by the movement of a scalar iso-contour that corresponds to the reaction front. For a given iso-contour of a species, the density weighted displacement speed [96] is

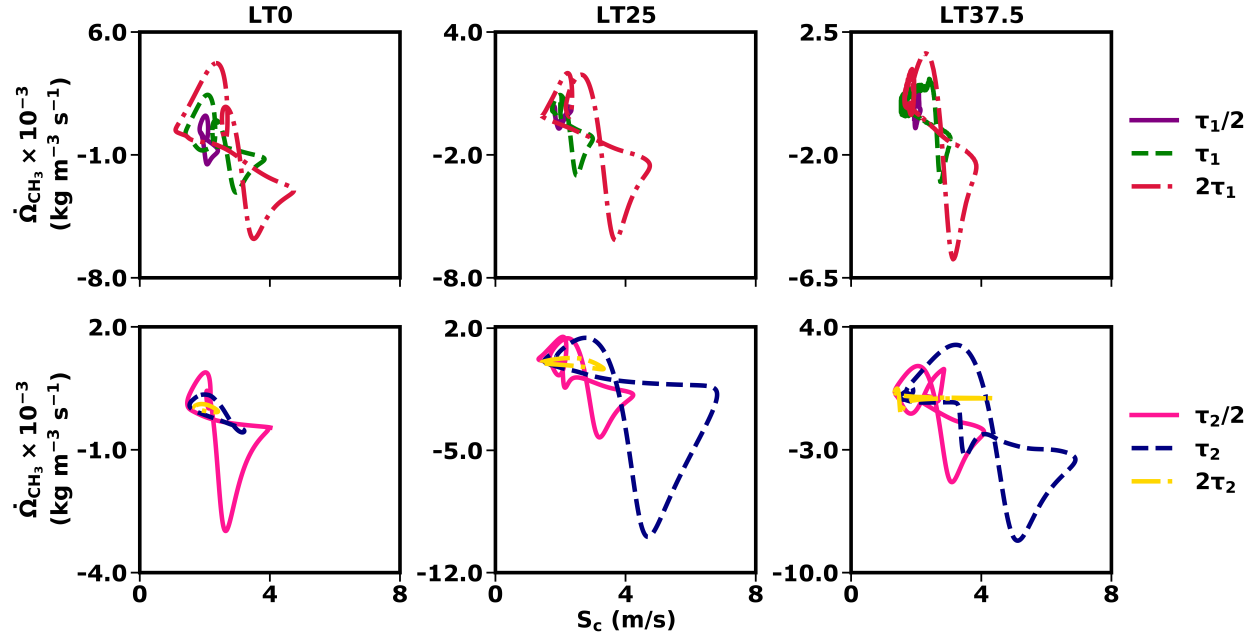

(a)

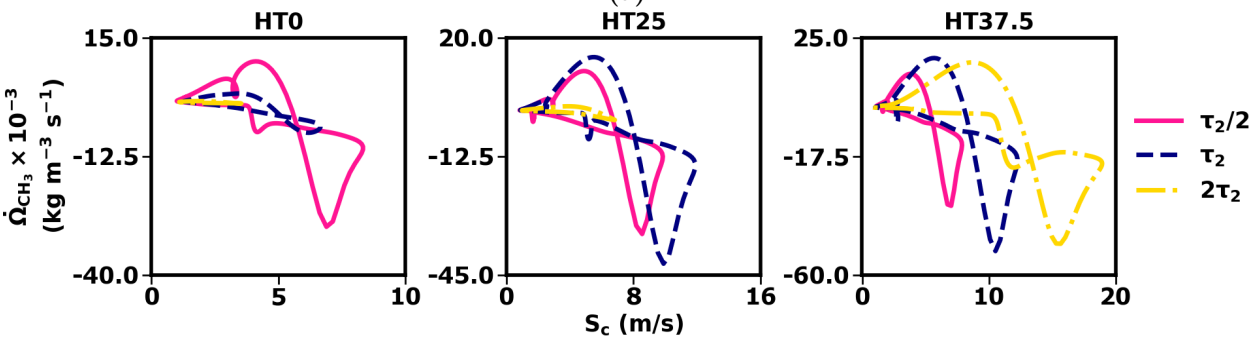

(b)

Figure 3.9: Correlation between S_c and $\dot{\Omega}_{CH_3}$ in a) LT, and b) HT cases at different oscillating time scales

defined as

$$S_{\mathrm{d}} = \frac{1}{\rho_{\mathrm{u}}|\nabla Y_{\mathrm{k}}|}(-\dot{\omega}_{\mathrm{k}} - \nabla \cdot (\rho D Y_{\mathrm{k}})) \tag{3.12}$$

where ρ_u is the density of the unburned mixture, $\dot{\omega}_k$ is the reaction rate of species k, Y_k is the mass fraction of species k and D is the thermal diffusivity. In this subsection, a displacement speed analysis is performed to identify the nature of the combustion mode. Since different shapes of limit cycles are observed based on the imposed value of τ_0 and c, S_{d} analysis has been carried out for three specific limit cycles as representative cases. The instantaneous S_{d} is evaluated at the spatial location where 50% of the cumulative CO_2 is produced. O_2 is used as the marker species to maintain consistency since S_{c} has also defined based on O_2 consumption. Under steady conditions, CO_2 was identified to have the narrowest spatial distribution among either of the reactant or product species as shown in Figure 3.10. As such, the choice of iso-contour is the least ambiguous in case of CO_2. Moreover, CO_2 was noticed to be predominantly produced only during the main ignition stage in the respective cases. This makes it an apt choice for performing the S_{d} analysis for the high-temperature reaction front. The steady and unsteady displacement speed results based on the chosen

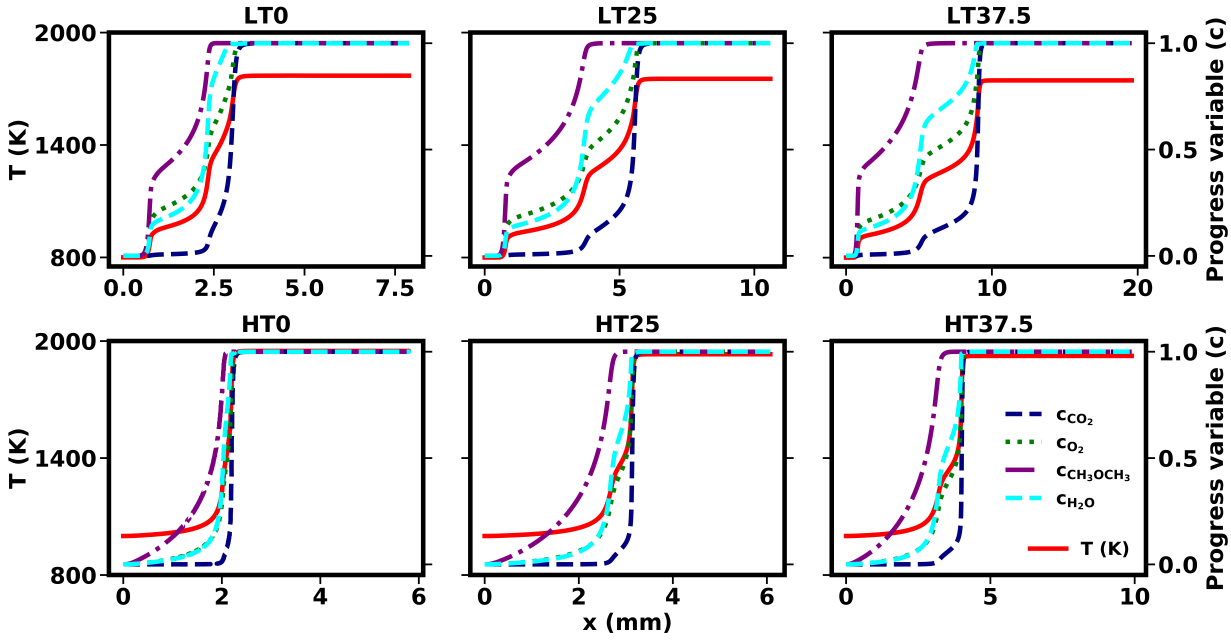

Figure 3.10: Spatial distribution of temperature and progress variable of different species in the respective cases. The ordinate axis range on each row of sub-figures is the same and hence omitted.

iso-contour ensure that the analysis is always performed within the high-temperature heat-release zone. The temperature at the chosen location of the iso-contour is $\approx 2 \times\ T_0$ in the LT cases and $\approx 1.75 \times\ T_0$ in the HT cases.

In addition, the individual contributions of different combustion modes to the total consumption speed, S_c is also evaluated. This is accomplished by first partitioning the domain based on the rate of change of temperature with the horizontal spatial location i.e. $\mathrm{d}T/\mathrm{d}x$ as depicted in Figure 3.11 and then integrating the oxygen reaction rate within the individual sub-domains. Cool reaction front (CF), pre-ignition (PI) upstream of the hot reaction front, spontaneous ignition front (SF) and hot reaction front (HF) zones depicted in Figure 3.11 are all identified this way. The CF region is demarcated between the origin and the spatial location where the temperature plateaus, i.e. either $\mathrm{d}T/\mathrm{d}x = 0$ or $\mathrm{d}T/\mathrm{d}x$ reaches a constant value between two consecutive grid points. Both PI and SF propagation modes can be observed to give rise to two separate reaction fronts with opposing temperature gradients. Hence, the first part of the PI/SF region is demarcated from the end point of CF

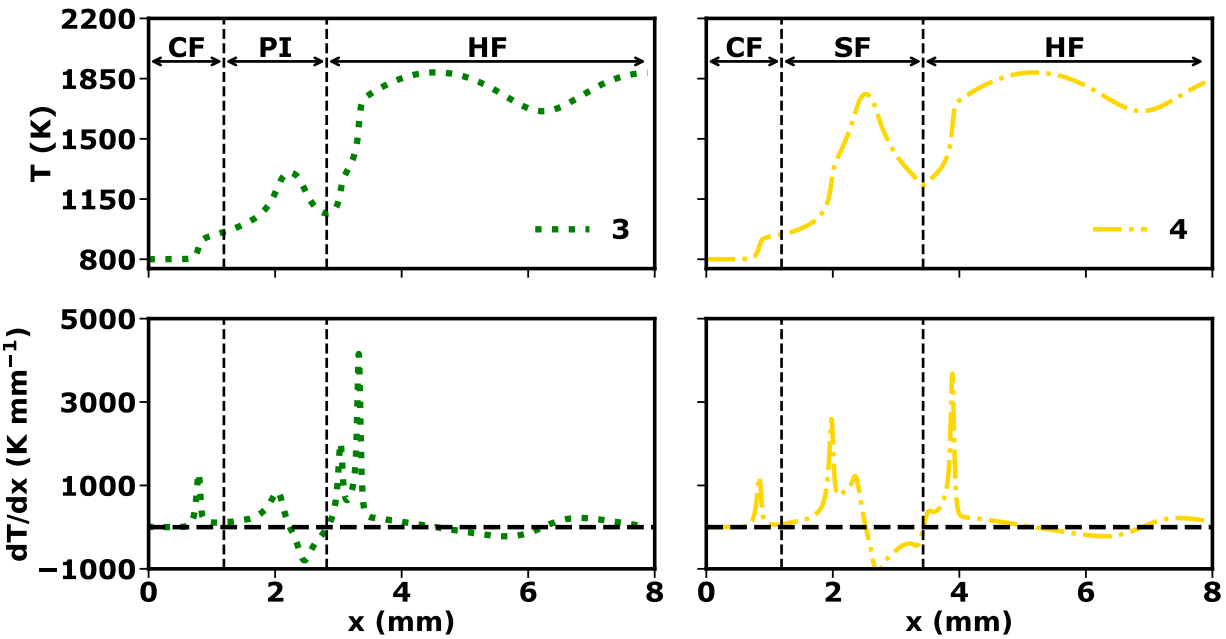

Figure 3.11: Partitioning the domain based on temperature gradient for evaluating the individual contributions of the cool reaction front (CF), pre-ignition (PI), spontaneous ignition front (SF) as well as the hot reaction front (HF) to the total consumption speed, S_c, in case LT0 at $\tau_0 = 2\tau_1$. The ordinate axis range on each row of sub-figures is the same and hence omitted.

to the point where the temperature reaches a constant value. From this point, the second part of the PI region is demarcated up to the point where the temperature becomes constant again. Once the PI/SF region is demarcated, the rest of the domain is identified as the HF region. PI is separated from SF based on the criterion used for performing the displacement speed analysis i.e. spatial location of 50 % cumulative CO_2 production.

As an illustration, Figure 3.12 shows the partitioned domain based on the local temperature gradients in case LT0 at $\tau_0 = 2\tau_1$. At point 3, three separate regions are identified — CF, PI, and HF. Accordingly, the integrated oxygen reaction rate within the individual sub-domains is then computed to measure the individual contributions of the respective combustion modes to the total consumption speed, S_c. The peak heat release rate, $\dot{Q}$, in the PI as well as the SF zone is significantly higher than that in the HF zone. Moreover, a significant amount of CO_2 production along with CH_3OCH_3 consumption is observed during the PI stage which is contrary to that under steady conditions. This observation suggests that under specific time scales, 2^{nd}-stage and main stage ignition could occur simultaneously. As such, PI and SF are related to both 2^{nd}-stage and main-stage heat release rate. This is another reason for only identifying the 1^{st}-stage and the main stage ignition in the present study. The reaction rate profile of CH_3OCH_2OH (representing LTC) further confirms that the different regions including the cool flame have been correctly identified by monitoring the variation in $\mathrm{d}T/\mathrm{d}x$. At point 4, the upstream pre-ignition matures into spontaneous ignition fronts (identified on the basis of iso-contour representing 50% of the cumulative CO_2 production). Consequently, the oxygen reaction within three separate regions — CF, SF and HF is evaluated to measure the individual contributions of the respective combustion modes to S_c. The same procedure has been adopted in the other two cases.

It should be noted that the domain segmentation analysis performed in the present study is mainly to provide additional quantification of the mechanisms leading to very high instantaneous consumption speeds that have been observed at specific time scales in each of the chosen cases. It is indeed not trivial to perform similar domain segmentation for multi-dimensional turbulent flames. Hence, before moving to multi-dimensional studies, a simple 1-D configuration was specifically adopted in the present study to enable additional

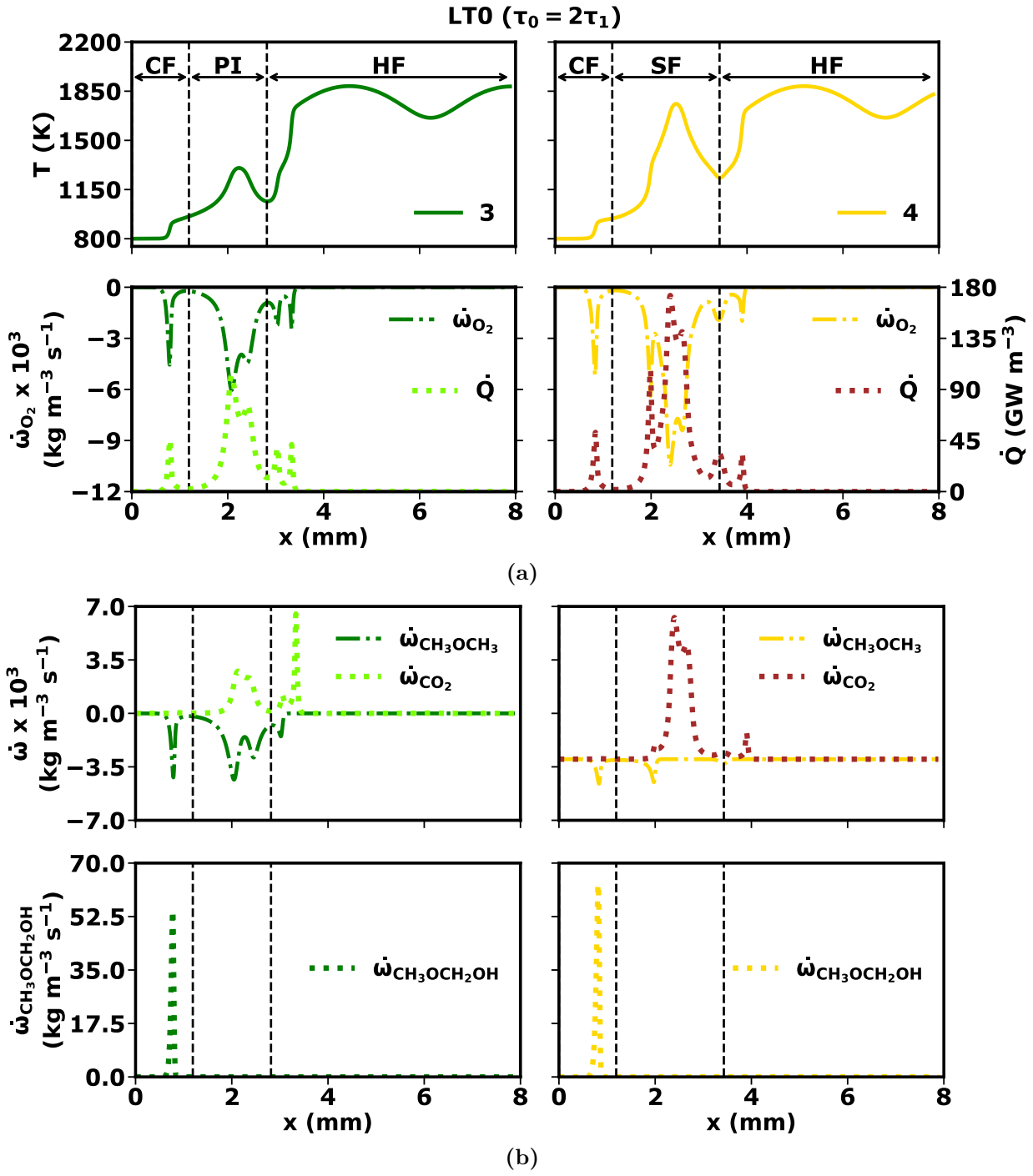

Figure 3.12: Individual contributions of the cool reaction front (CF), pre-ignition (PI), spontaneous ignition front (SF) as well as the hot reaction front (HF) to the total consumption speed, S_c in case LT0 at $\tau_0 = 2\tau_1$. The temperature, T, heat release rate, $\dot{Q}$, and the species reaction rate profiles correspond to points 3 and 4 depicted in Figure 3.13 (a). The ordinate axis range on each row of sub-figures is the same and hence omitted.

diagnostics of the obtained results, which may generally be not possible in multi-dimensional studies. For the 1-D flame configuration used in the present study, results obtained in the presence as well as absence of multi-stage ignition have shown consistent behavior while using the aforementioned domain segmentation approach. However, it may not be applicable to an arbitrary 1D flame wherein a CF region is embedded between PI/SF and HF regions. In such cases, an additional threshold could potentially be identified first, based on the maximum temperature attained in the cool flame (which is usually lower than the minimum temperature in either PI/SF or HF regions). The second CF region embedded between PI/SF and HF regions in such an arbitrary 1-D flame could then be identified based on this temperature threshold and subsequently verified by analyzing the reaction rate profiles of the representative LTC and HTC radicals.

Figure 3.13 shows the results of mode contributions for the three representative limit cycles at $\tau_0 = 2\tau_1, \tau_2$ and $\tau_2/2$ in cases LT0, LT25 and HT37.5, respectively. Points 1 to 4 in each sub-figure denote the temporal progression during a given oscillatory cycle. As before, the time axis is normalized by τ_0. The black dashed line in the right column of figures denotes the mean propagation speed of 2 m/s which separates auto-ignition assisted deflagration (HF) from spontaneous propagation (SF) modes. For unstretched, one-dimensional flames, the consumption speed through a flame front is equal to the density weighted displacement speed. Refs. [21, 56, 81] have demonstrated that the transition from deflagration to spontaneous (i.e. ignition-controlled) propagation occurs very gradually over a wide range of inlet velocities. Therefore, there is potentially a number of inlet velocities that could be used to differentiate deflagration from spontaneous propagation. This is also reflected in the non-unique reference laminar flame speeds that have been obtained as per the methodology suggested in [21] (see Figure 3.3). The range of reference laminar flame speed obtained in each case provides bounds to the value of S that can be used to differentiate deflagration from spontaneous propagation. Since $S = 2$ m/s is used as an initial condition in each case at which the reaction front is in the auto-ignition assisted deflagration regime and not in the spontaneous-ignition controlled regime (established via a transport budget analysis presented in Figure 3.5), the chosen parameter of $S = 2$ m/s is found to be the most logical choice for distinguishing SF from HF. At all points, the front propagation is made of multiple modes at varying degrees.

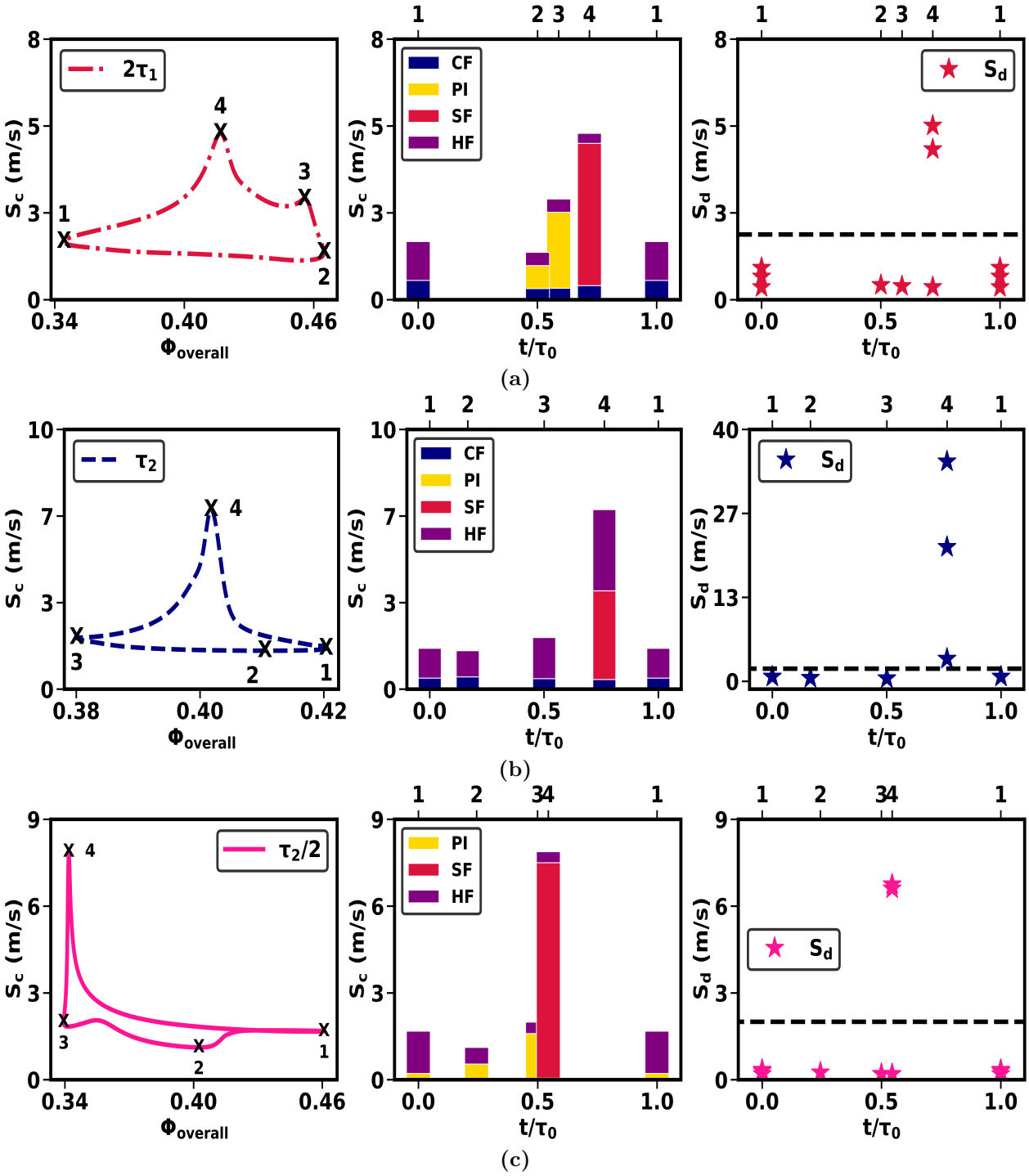

Figure 3.13: Individual contributions of cool reaction front (CF), pre-ignition (PI), spontaneous ignition front (SF) and hot reaction front (HF) to S_c and S_d analysis for the limit cycle at a) $\tau_0 = 2\tau_1$ in case LT0, b) $\tau_0 = 2\tau_2$ in case LT25, c) $\tau_0 = \tau_2/2$ in case HT37.5

In particular, rise in the instantaneous S_c at point 4 is mainly attributed to an increased contribution from spontaneous ignition fronts (SF). Most other points are found to be in the auto-ignition assisted deflagration regime ($S_d < 2$ m/s) with negligible contribution from either pre-ignition or spontaneous ignition fronts. It is also notable that maximum S_d in case LT25 is much higher than any other cases.

In case LT25, there is no contribution from pre-ignition at any point on the limit cycle. Furthermore, the contribution of the cool reaction front does not change noticeably throughout the limit cycle. This is consistent with the conclusions in Section 3.3, where HTC was found to be mainly responsible for the observed rise in instantaneous S_c. The simultaneous presence of such dual combustion modes coupled with the periodic transition of the high-temperature reaction front from deflagration to spontaneous propagation provides further explanation for the complex shapes of the limit cycles that have been observed in each case. Note that S_c is an integrated quantity while S_d is a local measure, and thus the two quantities do not necessarily match quantitatively.

To validate that the selected iso-contour accurately differentiate deflagrations from spontaneous ignition fronts, the instantaneous temperature profiles for the three chosen limit cycles is shown in Figure 3.14. For the chosen cases involving LTC (i.e. LT0 and LT25), it can be seen that there is no significant change in the temperature profile of the cool reaction front due to the imposed stratification. However, at $\tau_0 = 2\tau_1$ in case LT0, the upstream mixture spontaneously ignites and establishes multiple reaction fronts ahead of the existing hot reaction front. On the other hand, at $\tau_0 = \tau_2$ in case LT25, a periodic transition of the hot reaction front from deflagration to spontaneous propagation regime is observed. The sequence of combustion mode transition at $\tau_0 = \tau_2/2$ in case HT37.5 is found to be qualitatively similar to that in case LT0 at $\tau_0 = 2\tau_1$, wherein pre-ignition in the upstream mixture establishes multiple reaction fronts ahead of the existing hot reaction front. From these observations, it can deduced that the sequence of transition in the front propagation regime is highly dependent on the value of τ_0 and c, which in turn affects the overall front propagation speed as well as the shape of the limit cycle.

Finally, it is also useful to measure the time a reaction front takes to accelerate from mean S_c (i.e. 2 m/s) to peak S_c, t_{rise}, and then decelerate back from peak S_c to mean S_c,

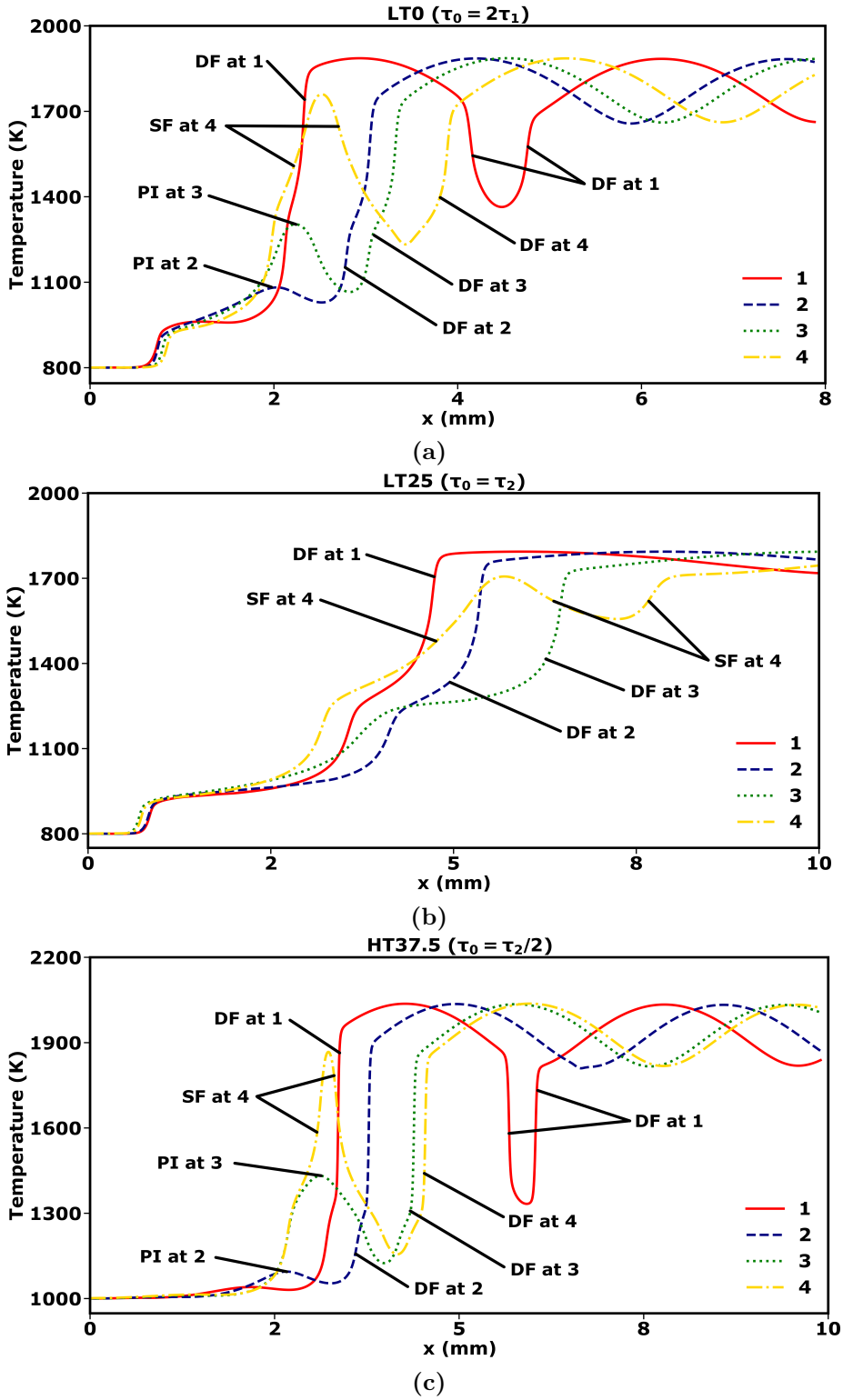

Figure 3.14: Variation in temperature profiles at a) $\tau_0 = 2\tau_1$ in case LT0, b) $\tau_0 = \tau_2$ in case LT25 and c) $\tau_0 = \tau_2/2$ in case HT37.5. Here, DF = Deflagration front, SF = Spontaneous ignition front, PI = Pre-ignition.

t_{fall}. Specifically, t_{rise} and t_{fall} were evaluated from the results shown in Figures 3.7 and 3.8. The computed values of t_{rise} and t_{fall} for the different cases are listed in Table 3.3. It is found that, for a given amplitude of oscillation, the magnitudes of t_{rise} and t_{fall} increase with an increase in τ_0, in majority of the LT cases and all the HT cases. The temporal variation in DME concentration at the inlet translates into pockets of stratified composition field due to flow advection. The frequency of oscillation along with the inlet flow velocity determines the characteristic length scale of the stratification. As such, larger stratification time scales give rise to hot/cold spots of larger sizes. Therefore, the time required by a given hot/cold spot to combust completely is directly dependent upon its size. Hence, both t_{rise} and t_{fall} increase with τ_0. It can also be seen that, irrespective of the amplitude of stratification or the stratification time scales, if there is enough induction time (dependent on the concentration of CH_4 in the binary blend and hence magnitude of τ_2), the upstream mixture auto-ignites and establishes additional reaction fronts ahead of the main flame front which causes a swift rise in instantaneous S_c.

3.5 Concluding remarks

A parametric study of front propagation speeds from fully resolved unsteady one-dimensional simulations with dimethyl-ether/methane/air mixtures under engine relevant conditions was presented using reduced kinetics and transport. Different time scales of monochromatic inhomogeneities in DME concentration with varying DME/methane blending ratios were simulated to understand the effect of reactivity stratification on the flame dynamics. In each case, the simulation was run until a statistically stationary limit-cycle behavior was observed. Different shapes of limit cycles were observed based on the imposed value of stratification time scale and the blending ratio. The variation in the cumulative reaction rate of methyl radical (representing high-temperature chemistry) as well as the methoxy-methyl-peroxy radical (representing low-temperature chemistry) over a given limit cycle was examined. Unlike the low-temperature chemistry, the feedback of high-temperature chemistry to the imposed stratification predominantly affected the propagation speed. For all the cases being studied here, it was found that the magnitude of unsteady global consumption speed, S_c,

Table 3.3: Time required to transition from mean S_c (i.e. 2 m/s) to peak S_c and vice-versa at different time scales in the respective cases

Case	τ_0 (μs)	**Peak S_c (m/s)**	t_{rise} (μs)	t_{fall} (μs)	A	**Pre-ignition observed?**
LT0	$\tau_1/2$	**2.4**	**26**	**19.5**	**0.06**	**Yes**
	τ_1	**3.84**	**102**	**63**	**0.06**	**Yes**
	$2\tau_1$	**4.74**	**117.5**	**219.5**	**0.06**	**Yes**
	$\tau_2/2$	**3.96**	**217**	**41.5**	**0.02**	**Yes**
	τ_2	**3.22**	**249**	**211**	**0.02**	**No**
	$2\tau_2$	**2.41**	**404**	**691.5**	**0.02**	**No**
LT25	$\tau_1/2$	**2.34**	**20**	**71**	**0.06**	**Yes**
	τ_1	**2.99**	**41.5**	**87**	**0.06**	**Yes**
	$2\tau_1$	**4.75**	**262.5**	**98.5**	**0.06**	**Yes**
	$\tau_2/2$	**4.24**	**111**	**256**	**0.02**	**Yes**
	τ_2	**6.82**	**296**	**200.5**	**0.02**	**Yes**
	$2\tau_2$	**3.33**	**765.5**	**964.5**	**0.02**	**No**
LT37.5	$\tau_1/2$	**2.13**	**15**	**18.5**	**0.06**	**Yes**
	τ_1	**3.05**	**121.5**	**51.5**	**0.06**	**Yes**
	$2\tau_1$	**3.85**	**74**	**113.5**	**0.06**	**Yes**
	$\tau_2/2$	**4.09**	**81.5**	**818.5**	**0.02**	**Yes**
	τ_2	**6.9**	**263**	**313**	**0.02**	**Yes**
	$2\tau_2$	**4.35**	**1087.5**	**1409.5**	**0.02**	**No**
HT0	$\tau_2/2$	**8.33**	**64.5**	**68.5**	**0.06**	**Yes**
	τ_2	**6.65**	**118.5**	**193**	**0.06**	**No**
	$2\tau_2$	**3.54**	**352**	**563**	**0.06**	**No**
HT25	$\tau_2/2$	**9.85**	**121.5**	**145.5**	**0.06**	**Yes**
	τ_2	**11.9**	**175.5**	**292**	**0.06**	**No**
	$2\tau_2$	**6.83**	**315**	**744.5**	**0.06**	**No**
HT37.5	$\tau_2/2$	**7.88**	**41**	**146.5**	**0.06**	**Yes**
	τ_2	**12.25**	**268.5**	**436.5**	**0.06**	**Yes**
	$2\tau_2$	**18.94**	**343**	**936**	**0.06**	**Yes**

scales proportionally to the corresponding variation in the cumulative reaction rate of methyl radical.

At smaller time scales, with an increase in the level of CH_4 concentration in the binary fuel blend, there was a suppression in the dynamic response of a reaction front involving low-temperature chemistry. Addition of CH_4 made the binary fuel blend more resistant to auto-ignition. As a result, the high-temperature chemistry remained mostly unaffected, which was manifested by the reduced variation in the cumulative reaction rate of methyl radical. At larger time scales, however, increasing the level of CH_4 concentration in the binary fuel blend caused a noticeable increase in the dynamic response of a reaction front, irrespective of the presence/absence of low-temperature chemistry. It was shown that this behavior was mainly due to a more responsive high-temperature chemistry. Moreover, based on the variation in the cumulative reaction rate of methoxy-methyl-peroxy radical over a given limit cycle, at relatively smaller time scales, the low-temperature chemistry showed a similar dynamic response irrespective of the level of CH_4 concentration in the binary fuel blend. On the other hand, at larger time scales, it became increasingly non-responsive with an increase in the level of CH_4 concentration in the binary fuel blend.

The displacement speed analysis together with the temporal evolution of temperature profile provides evidence of cyclical transition of the combustion mode from deflagration to spontaneous propagation. The induction time available for the upstream mixture to pre-ignite increased with an increase in the CH_4 concentration in the binary fuel blend. As such, multiple reaction fronts were observed ahead of the main flame front, irrespective of either the amplitude or the time scale of stratification. These reaction fronts propagated at much higher speeds than the main flame front itself and predominantly lead to a substantial rise in the overall propagation speed.

Chapter 4

WENO schemes - an essential element of DNS solvers

Results discussed in chapters 2 and 3 displayed a high probability of contact discontinuities embedded within relatively smooth regions in the computational domain. As mentioned earlier in the introduction, the presence of such discontinuities may render the standard eighth-order finite central difference operator [24] used in KARFS cost-prohibitive due to extremely fine grid resolution requirement or ineffective in capturing the underlying physics altogether. As such, before proceeding to multi-dimensional simulations, the implementation methodology and validation of several high-order WENO schemes in KARFS is presented in this chapter. Moreover, the scalability and performance of KARFS is demonstrated using different grid sizes, block decomposition and parallelism strategies. In addition, the performance portability of KARFS is demonstrated on a variety of heterogeneous architectures including NVIDIA Tesla P100 GPUs and NVIDIA Kepler K20X GPUs.

4.1 Implementation of WENO

The convective term in Equation (1b) of Appendix A, $\frac{\partial(\rho u_i u_j)}{\partial x_j}$, makes the system of governing Equations (1a) to (1d) highly non-linear and is responsible for complex features such as shock waves, contact discontinuities and turbulence. Hence, the use of minimally dissipative, high-order shock capturing schemes is an essential element when computing

complex compressible reacting flows in order to avoid excessive numerical damping of the flow features over a wide range of length scales as well as to prevent spurious numerical oscillations near shock waves and discontinuities. In particular, implementation of a seventh-order mapped WENO (WENO7M) scheme is described below. Several other WENO schemes including the 8^{th}-order symmetric bandwidth optimized WENO (WENO8) [103] and the 7^{th}-order WENO-Z scheme (WENO7Z) [104] have also been implemented in KARFS, details of which are provided in Appendix B. The different WENO schemes in KARFS yielded similar results in majority of the validation and performance studies. As such, only the test cases yielding different results while using the various WENO schemes have been discussed for brevity. Furthermore, for the sake of conciseness, the presentation is restricted to the x-direction only, noting that the same procedure can be easily applied in the y- and z-directions respectively.

The main concept of the WENO scheme is to use a superposition of several sub-stencils with adaptive coefficients to construct a higher-order approximation of the solution, avoiding the interpolation across discontinuities and preserving a uniformly high order of accuracy at all points where the solution is smooth. Specifically, the WENO procedure is based on the fact that a reconstruction polynomial can be decomposed as a certain convex combination of reconstruction polynomials of lower order, provided they are evaluated at points within a certain range. To illustrate this idea, we consider the one-dimensional (x-direction) version of the system of governing Equations (1a) to (1d) provided in Appendix A:

$$\frac{\partial Q_t}{\partial t} + \frac{\partial C_x}{\partial x} + \frac{\partial D_x}{\partial x} = S\,, \tag{4.1}$$

where

$$Q_t = \begin{pmatrix} \rho \\ \rho u \\ \rho e_{\text{t}} \\ \rho Y_k \end{pmatrix}\,,\; C_x = \begin{pmatrix} \rho u_x \\ \rho {u_x}^2 + P \\ (\rho e_{\text{t}} + P) u_x \\ \rho Y_k u_x \end{pmatrix}\,,\; D_x = \begin{pmatrix} 0 \\ -\tau_{xx} \\ -(\tau_{xx} u_x + \tau_{xy} u_y + \tau_{xz} u_z) + q \\ J_{k,x} \end{pmatrix}\,,\; S = \begin{pmatrix} 0 \\ 0 \\ 0 \\ \dot{\omega}_k \end{pmatrix}$$

In Equation 4.1, Q_t is the solution vector, C_x is the vector consisting of the convective flux functions, D_x is the vector consisting of the viscous and molecular diffusion flux functions, and S is the vector of source terms. Problems involving shocks or contact discontinuities require separate treatment of the convective and the diffusive flux components. Henceforth, the spatial derivatives of the convective flux functions are determined using the WENO7M scheme whereas the spatial derivatives of the viscous and the molecular diffusion flux functions are determined using an eighth-order centered-difference (CD8) scheme. The WENO reconstruction procedure could be directly applied to any given set of quantities: primitive variables, conservative variables or their flux components. For ensuring stability, it is preferred to split the convective flux components in the physical space rather than the characteristic space, as in the present framework. Accordingly, each of the convective flux functions are split using the local Lax-Friedrichs flux splitting methodology [105]:

$$C_x = C_x^+ + C_x^- \,, \text{ where} \tag{4.2}$$

$$C_x^+ = \frac{1}{2}(C_x + \lambda_{\max} Q_t)\,, C_x^- = \frac{1}{2}(C_x - \lambda_{\max} Q_t)$$

Here, $\lambda_{\max}$ is the maximum local wave propagation speed in x-direction, which can be determined as

$$\begin{aligned}(\lambda_{\max})_i = \max((|u_x|)_{i-1}, (|u_x| + c)_{i-1}, (|u_x| - c)_{i-1}\,, \\ (|u_x|)_i, (|u_x| + c)_i, (|u_x| - c)_i)\end{aligned} \tag{4.3}$$

with u_x being the flow velocity in x-direction and c being the sound speed. For finding the maximum local wave propagation speed in multiple dimensions, the respective flow velocities in y- (v_y) and z- (w_z) directions are used. The spatial derivative of the convective flux function can be obtained by differentiating Equation 4.2 with respect to x,

$$\frac{\partial C}{\partial x} = \frac{\partial C^+}{\partial x} + \frac{\partial C^-}{\partial x}\,. \tag{4.4}$$

In the WENO framework, for each grid point, reconstructed left and right states are determined and used to calculate fluxes at edges as

$$\left.\frac{\partial C^+}{\partial x}\right|_i = \left.\frac{\partial \hat{C}^+}{\partial x}\right|_{i+1/2} - \left.\frac{\partial \hat{C}^+}{\partial x}\right|_{i-1/2},$$
$$\left.\frac{\partial C^-}{\partial x}\right|_i = \left.\frac{\partial \hat{C}^-}{\partial x}\right|_{i+1/2} - \left.\frac{\partial \hat{C}^-}{\partial x}\right|_{i-1/2}.$$

This is accomplished in KARFS by using the WENO7M interpolator as follows:

$$\left.\frac{\partial \hat{C}^+}{\partial x}\right|_{i+1/2} = \frac{\text{WENO7M}(C^+_{i-3}, C^+_{i-2}, C^+_{i-1}, C^+_i, C^+_{i+1}, C^+_{i+2}, C^+_{i+3})}{\Delta x} \tag{4.6a}$$

$$\left.\frac{\partial \hat{C}^+}{\partial x}\right|_{i-1/2} = \frac{\text{WENO7M}(C^+_{i-4}, C^+_{i-3}, C^+_{i-2}, C^+_{i-1}, C^+_i, C^+_{i+1}, C^+_{i+2})}{\Delta x} \tag{4.6b}$$

$$\left.\frac{\partial \hat{C}^-}{\partial x}\right|_{i+1/2} = \frac{\text{WENO7M}(C^-_{i+4}, C^-_{i+3}, C^-_{i+2}, C^-_{i+1}, C^-_i, C^-_{i-1}, C^-_{i-2})}{\Delta x} \tag{4.6c}$$

$$\left.\frac{\partial \hat{C}^-}{\partial x}\right|_{i-1/2} = \frac{\text{WENO7M}(C^-_{i+3}, C^-_{i+2}, C^-_{i+1}, C^-_i, C^-_{i-1}, C^-_{i-2}, C^-_{i-3})}{\Delta x} \tag{4.6d}$$

The Equations (4.6a) to (4.6d) give an approximation of the spatial derivative of the numerical flux function [106, 107] at $i\pm1/2$. The functional form of the WENO7M interpolator in Equation (4.6a) is given by

$$\text{WENO7M}(C^+_{i-3}, C^+_{i-2}, C^+_{i-1}, C^+_i, C^+_{i+1}, C^+_{i+2}, C^+_{i+3}) = \sum_{k=0}^{3} w_k a_k\,, \tag{4.7}$$

where w_k are the WENO7M weights and the component stencils a_k are

$$a_0 = \frac{1}{24}(-6C^+_{i-3} + 26C^+_{i-2} - 46C^+_{i-1} + 50C^+_i)\,, \tag{4.8a}$$

$$a_1 = \frac{1}{24}(2C^+_{i-2} - 10C^+_{i-1} + 26C^+_i + 6C^+_{i+1})\,, \tag{4.8b}$$

$$a_2 = \frac{1}{24}(-2C^+_{i-1} + 14C^+_i + 14C^+_{i+1} - 2C^+_{i+2})\,, \tag{4.8c}$$

$$a_3 = \frac{1}{24}(6C^+_i + 26C^+_{i+1} - 10C^+_{i+2} + 2C^+_{i+3})\,. \tag{4.8d}$$

The weights w_k are formulated in two steps as outlined in [108]. The final weights are first approximated following the procedure described in [107] as

$$w^*_k = \frac{\gamma_k}{\sum_{i=0}^{3}\gamma_i},\ \text{where}\ \gamma_k = \frac{\bar{w}_k}{(\epsilon + \beta_k)^p}\,. \tag{4.9}$$

The weights used to ponder the contribution of each lower-order polynomial depend on the interpolating point and are known as ideal weights, $\bar{w}_k$. WENO schemes define nonlinear weights based on the ideal weights so as to construct an essentially non-oscillatory interpolant. As such, the ideal weights are assigned constant values as follows

$$\bar{w}_0 = \frac{1}{35},\ \bar{w}_1 = \frac{12}{35},\ \bar{w}_2 = \frac{18}{35},\ \bar{w}_3 = \frac{4}{35}\,, \tag{4.10}$$

and the smoothness indicators β_k are defined as

$$\begin{aligned}
\beta_0 =& \frac{1}{36}(-2C^+_{i-3} + 9C^+_{i-2} - 18C^+_{i-1} + 11C^+_i)^2 \\
&+ \frac{13}{12}(-C^+_{i-3} + 4C^+_{i-2} - 5C^+_{i-1} + 2C^+_i)^2 \\
&+ \frac{781}{720}(-C^+_{i-3} + 3C^+_{i-2} - 3C^+_{i-1} + C^+_i)^2\,,
\end{aligned} \tag{4.11a}$$

$$\begin{aligned}
\beta_1 =& \frac{1}{36}(C^+_{i-2} - 6C^+_{i-1} + 3C^+_i + 2C^+_{i+1})^2 \\
&+ \frac{13}{12}(C^+_{i-1} - 2C^+_i + C^+_{i+1})^2 \\
&+ \frac{781}{720}(-C^+_{i-2} + 3C^+_{i-1} - 3C^+_i + C^+_{i+1})^2\,,
\end{aligned} \tag{4.11b}$$

$$\beta_2 = \frac{1}{36}(-2C^+_{i-1} - 3C^+_i + 6C^+_{i+1} - C^+_{i+2})^2$$

$$
\begin{aligned}
&+\frac{13}{12}(C_{i-1}^{+}-2C_{i}^{+}+C_{i+1}^{+})^{2}\\
&+\frac{781}{720}(-C_{i-1}^{+}+3C_{i}^{+}-3C_{i+1}^{+}+C_{i+2}^{+})^{2}\,, \qquad (4.11c)\\
\beta_3 =&\frac{1}{36}(-11C_{i}^{+}+18C_{i+1}^{+}-9C_{i+2}^{+}+2C_{i+3}^{+})^{2}\\
&+\frac{13}{12}(2C_{i}^{+}-5C_{i+1}^{+}+4C_{i+2}^{+}-C_{i+3}^{+})^{2}\\
&+\frac{781}{720}(-C_{i}^{+}+3C_{i+1}^{+}-3C_{i+2}^{+}+C_{i+3}^{+})^{2}\,. \qquad (4.11d)
\end{aligned}
$$

In Equation 4.9, $\epsilon = 10^{-40}$ is a small number that prevents division by zero errors [106] and p may be varied to increase or decrease the WENO7M adaptation sensitivity. Unless otherwise stated, $p = 2$ in the present study. The approximated w_k^* are now mapped to the corrected w_k such that the accuracy of the method is seventh-order in general. This is achieved through the mapping procedure outlined in Ref. [108]

$$
g_k(w) = \frac{w(\bar{w}_k + \bar{w}_k^2 - 3\bar{w}_k w + w^2)}{\bar{w}_k^2 + (1-2\bar{w}_k)w}\,. \qquad (4.12)
$$

The final corrected weights are then given by

$$
w_k = \frac{g_k(w_k^*)}{\sum_{i=0}^{3} g_i(w_i^*)}\,. \qquad (4.13)
$$

From a close inspection of the set of Equations (4.6a) to (4.6d), it can be noticed that the spatial derivatives of positive and negative convective flux components at the left edge, i.e. $\frac{\partial \hat{C}^{+}}{\partial x}\Big|_{i-1/2}$ and $\frac{\partial \hat{C}^{-}}{\partial x}\Big|_{i-1/2}$, can be obtained by merely shifting the index of the corresponding spatial derivatives evaluated at the right edge, i.e. $\frac{\partial \hat{C}^{+}}{\partial x}\Big|_{i+1/2}$ and $\frac{\partial \hat{C}^{-}}{\partial x}\Big|_{i+1/2}$, by one to the left:

$$
\begin{aligned}
\frac{\partial \hat{C}^{\pm}}{\partial x}\Big|_{i-1/2} &= \frac{\mathrm{WENO7M}(C_{i-4}^{+}, C_{i-3}^{+}, C_{i-2}^{+}, C_{i-1}^{+}, C_{i}^{+}, C_{i+1}^{+}, C_{i+2}^{+})}{\Delta x}\\
&= \frac{\mathrm{WENO7M}(C_{i-3-1}^{+}, C_{i-2-1}^{+}, C_{i-1-1}^{+}, C_{i-0-1}^{+}, C_{i+1-1}^{+}, C_{i+2-1}^{+}, C_{i+3-1}^{+})}{\Delta x}
\end{aligned}
$$

$$= \frac{\partial \hat{C}^{\pm}}{\partial x}\Big|_{i+1/2-1}. \tag{4.14}$$

Hence, the WENO7M operator needs to be used only twice instead of four times for computing the numerical fluxes. While the number of convective flux evaluations does reduce to half as per Equation 4.14, the number of MPI communications is increased when performing the aforementioned shift. Note that for non-periodic domains, special handling is needed when evaluating the spatial derivatives of the convective flux functions at the boundaries. Using Equation 4.4, the spatial derivative of the convective flux function can finally be evaluated. Subsequently, the spatial derivatives of the viscous and molecular diffusion flux functions are determined using the CD8 scheme, and the solution is advanced in time.

4.2 Validation of WENO

4.2.1 Sod's shock tube problem

The popular Sod shock tube problem [109] constitutes probably one of the most standard numerical benchmarks designed for compressible-flow solvers. This test consists of a fluid, initially at rest, in which a virtual membrane located at the center of the domain separates two distinct sections: the one on the left at a higher density and pressure, and the one on the right at a lower density and pressure. The membrane is removed at $t = 0$ and a shock wave develops propagating toward the right, followed by a contact discontinuity and a rarefaction wave propagating to the left. The application of KARFS to this case serves to validate the implementation of the WENO7M scheme and evaluate its performance. In particular, we consider a one-dimensional (1D) setup, solving the 1D Euler equations. The tube is 1 m long and the initial conditions for pressure P, density ρ, and velocity u are as follows:

$$(P, \rho, u) = \begin{cases} (4.0 \text{ MPa}, 4.62659 \times 10^{-4} \text{ kg/m}^3, 0 \text{ m/s}), & x \leq 0.5 \text{ m}, \\ (1.0 \text{ MPa}, 1.15665 \times 10^{-4} \text{ kg/m}^3, 0 \text{ m/s}), & x > 0.5 \text{ m}. \end{cases} \tag{4.15}$$

The domain is uniformly discretized with 1200 grid points and the equations are integrated in time with a constant time step size of 1 ns. The fluid considered here is air and is assumed to be a perfect gas. The numerical solutions for pressure, density, velocity and specific internal energy, e, at time $t = 2.5$ μs are shown in Figure 4.1. The numerical solution provided by the WENO7M scheme in KARFS closely follows the exact solution. It is also seen that there is negligible spreading of the numerical solution in the vicinity of the contact discontinuity, which has been previously documented for the standard WENO family of schemes [107]. These results suggest that the WENO7M scheme, when properly applied to compressible DNS codes, can yield an excellent shock capturing capability.

4.2.2 Decay of isotropic turbulence

Turbulence is an irregular motion that can be described by statistical values, depending on both position and time, of the quantities that characterize the flow field. When all possible states of turbulence are equally probable at any given point of the flow field, turbulence is said to be homogeneous. When turbulence is isotropic, the statistical averages are independent of the coordinate system. Isotropic, homogeneous turbulence is an idealization, and its study

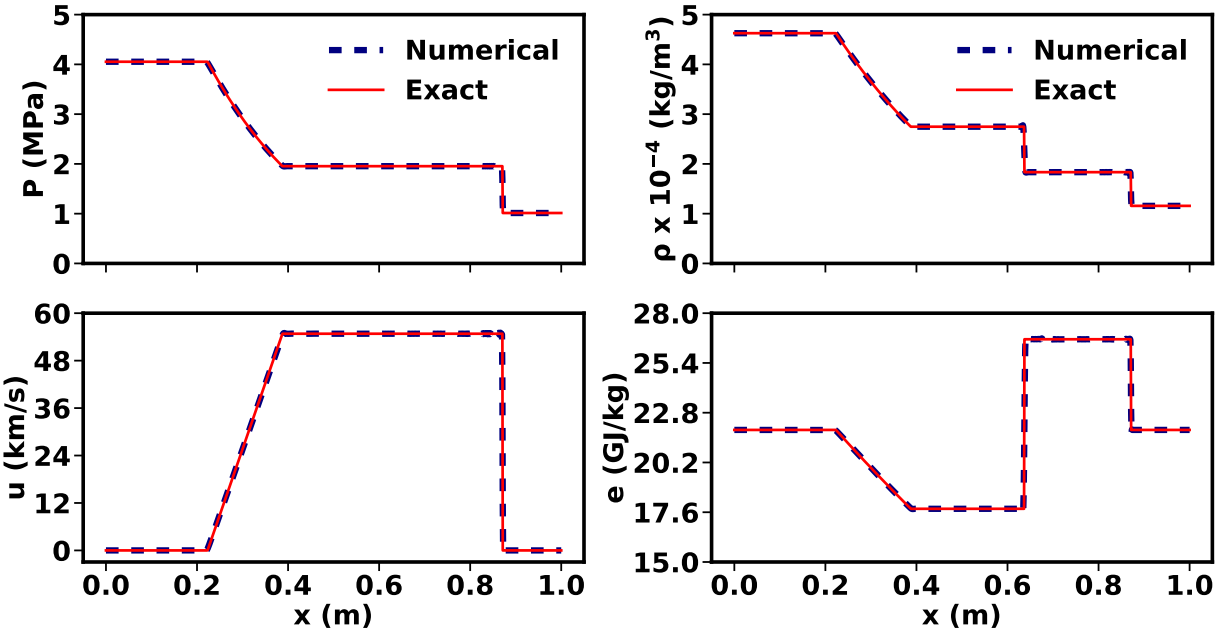

Figure 4.1: Comparison of exact and numerical solutions for pressure, density, velocity and specific internal energy at $t = 2.5$ μs

is the simplest possible study of turbulence. In this section, we consider decaying isotropic turbulence to test the efficiency of the various WENO schemes in resolving all the relevant turbulent length scales and time scales. The governing equations are the Equations (1a) to (1d). The simulation domain is a cube with 128^3 grid points, and the boundary conditions are periodic in all three Cartesian directions for all the flow variables. We start with a uniform density, pressure, temperature and a Passot-Pouquet spectrum [110] for velocity which is divergence free initially and given by:

$$E(k) = 16\sqrt{\frac{2}{\pi}}\left(\frac{u'^2}{k_\mathrm{e}}\right)\left(\frac{k}{k_\mathrm{e}}\right)^4 \exp\left(-2\left(\frac{k}{k_\mathrm{e}}\right)^2\right) \tag{4.16}$$

where k is the wave number, k_e is the wave number at which the spectrum peaks, and $u' = \langle(u_\mathrm{x}^2+v_\mathrm{y}^2+w_\mathrm{z}^2)/3\rangle^{1/2}$ is the turbulent fluctuating velocity. Here, $\langle....\rangle$ is a volume average over the computational domain at a fixed time instant. We consider the flow conditions where shock waves are not present and the comparison against the CD8 scheme is meaningful, specifically, the turbulent Mach number, $M_\mathrm{t} = 0.17$ and the Reynolds number based on the Taylor micro-scale (λ), $Re_\lambda = 35$, where

$$M_\mathrm{t} = \frac{\langle {u_\mathrm{x}}^2 + {v_\mathrm{y}}^2 + {w_\mathrm{z}}^2\rangle^{1/2}}{\langle c\rangle}, \text{ and} \tag{4.17}$$

$$Re_\lambda = \frac{u'\lambda}{\langle\nu\rangle} \tag{4.18}$$

k_e is determined from the most energetic length scale, l_e, which has been set as 446 μm. As before, the fluid considered here is air with an average density, $\langle\rho\rangle = 1.17$ kg/m^3 and an average temperature $\langle\mathrm{T}\rangle = 300$ K. Under the chosen conditions, the Kolmogorov length scale, $l_\mathrm{k} = 17.7$ μm. Accordingly, a uniform grid resolution of 8.8 μm is used such that there are at least 2 grid points across the Kolmogorov length scale. As such, numerically converged results are ensured. We simulate the decay of isotropic turbulence for 20 non-dimensional time periods based on the initial large-eddy turn over time, $\tau_\mathrm{eddy} = \lambda/u'$.

Figure 4.2(a) shows the temporal evolution of normalized turbulent kinetic energy, K_e for the various central difference as well as WENO schemes that have been implemented in

KARFS. As stated earlier in section 4.1, the power parameter, p, can be varied to increase or decrease the WENO adaptation sensitivity. Irrespective of the scheme employed, the normalized kinetic energy decays at almost an identical rate until t $\leq 7\tau_{\text{eddy}}$. CD6 (6^{th}-order central difference) and CD8 (8^{th}-order central difference) schemes show an identical and the least dissipation until the end of the simulation. It is also seen that with $p = 2$, the WENO7M (W7M, 7^{th}-order mapped WENO [106]) scheme has significantly higher dissipation than either WENO7Z (W7Z, 7^{th}-order WENO-Z [104]) or WENO8 (W8, 8^{th}-order bandwidth optimized WENO [103]) scheme for t $\geq 10\tau_{\text{eddy}}$. However, the dissipation of the WENO7M scheme is found to be significantly reduced by setting $p = 1$. Dissipation of the WENO7Z scheme is comparatively less wherein it matches that of the WENO8 scheme when $p = 2$ and better than both, WENO7M and WENO8 schemes when $p = 1$.

Figure 4.2(b), on the other hand, shows the energy spectra at t = 20 τ_{eddy} for the same simulations. Minor aliasing errors are found for each of the WENO schemes in the tail of the spectrum, which do not affect the overall results. These results indicate that a given WENO scheme, with an appropriate value of power parameter p, can be successfully used to

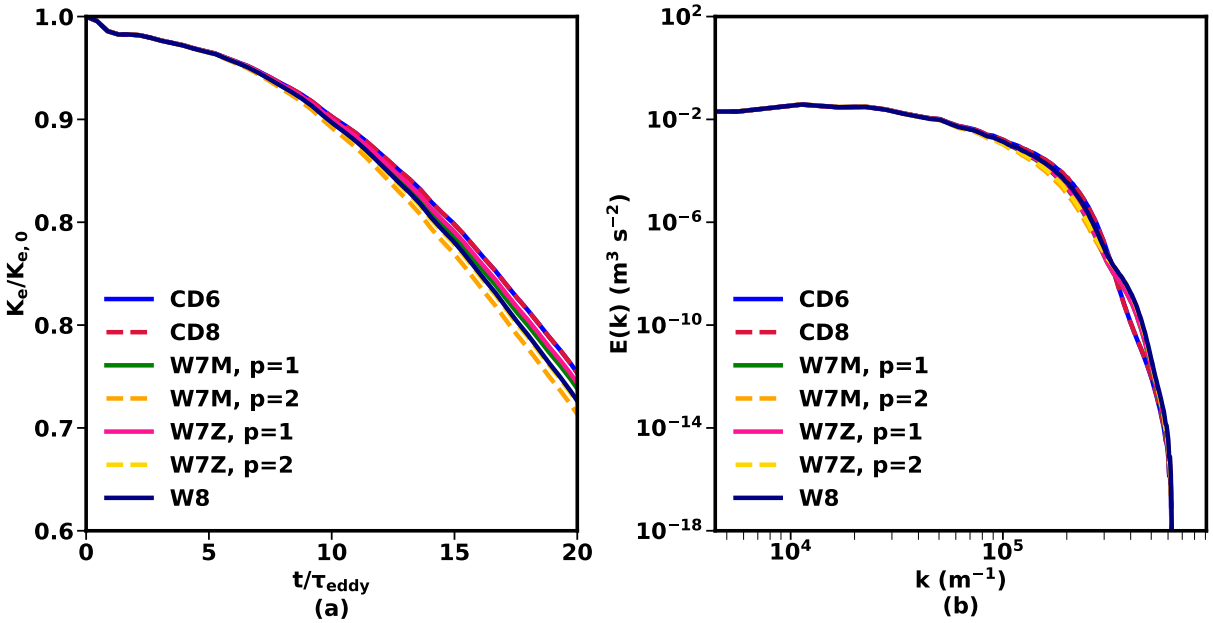

Figure 4.2: DNS data of decaying isotropic turbulence at $M_t = 0.17$ and $Re_\lambda = 35$, comparing the WENO7M, WENO7Z, WENO8, CD6 and the CD8 schemes. (a) Temporal evolution of turbulent kinetic energy and (b) energy spectra at t = 20 τ_{eddy}

simulate turbulent flows, especially in the absence of shocks. It is important to note that the WENO family of schemes tend to have higher numerical dissipation because of insufficient distinction between shock-containing and smooth regions on typical DNS grids. Decreasing the dissipation inherent in the WENO adaptation mechanism is challenging because potential deficiencies relevant primarily to the damping of turbulent features may become apparent only in realistic simulations and must then be examined locally.

4.2.3 Detonation in a thermally stratified constant volume reactor

Detonation development from a flame kernel initiated by a pre-ignition event is demonstrated here for further assessing the robustness of the newly implemented WENO7M scheme. The specific test case has been adopted from a recent study by Sow et al [111]. The WENO7M scheme is implemented for the convective terms, whereas the eighth-order central difference scheme is employed for the diffusive terms. The solution is advanced in time with a fourth-order, six-stage explicit Runge-Kutta scheme. The implicit stiff ODE CVODE solver with Strang splitting is also employed to deal with chemical stiffness. The numerical configuration (see Figure 4.3) is a constant volume reactor with impermeable and adiabatic walls at both boundaries. For the initial condition, the Cantera [1] solution for a freely propagating stoichiometric hydrogen-air flame with detailed chemistry [112] is mapped near the left wall to represent the initial flame front developed by the pre-ignition event. The flame travels from the left to the right where the initial pressure and velocity are constant and set to 10 atm and 0 m/s, respectively. The thermal stratification is modeled as a linear function and the magnitude of the temperature gradient, dT/dx is set at 2.4 K/mm, which corresponds to the temperature difference of 40 K over the length of the temperature variation. The total domain length, x_L is 20 mm and the initial position, x_0, where the temperature variation starts is 3.35 mm. A uniform grid spacing of 1 μm and a constant time step of 0.2 ns is used in the present study.

Figure 4.4 depicts some results obtained at six different times. Due to a positive temperature gradient, the end gas ignites. Propagation towards the flame amplifies the pressure wave. A subsequent increase in the chemical heat release is also noticeable during this period. When the auto-ignition front transitions to a developing detonation wave (256.8

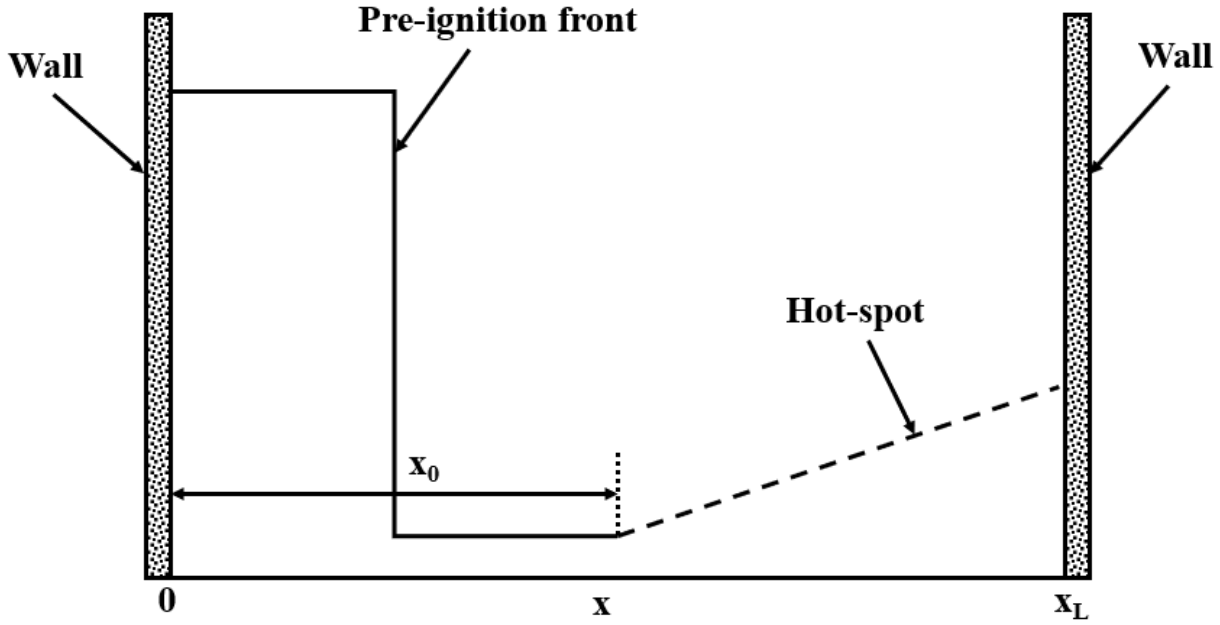

Figure 4.3: Numerical configuration for simulating detonation in a thermally stratified constant volume reactor

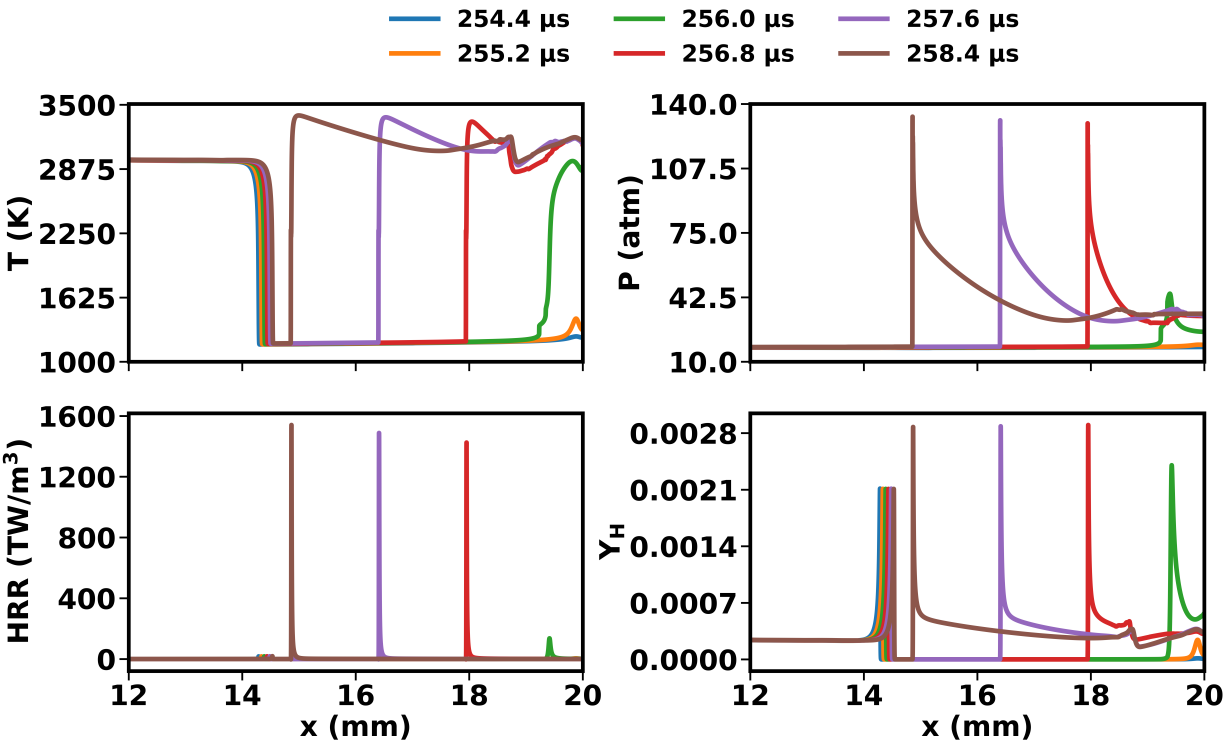

Figure 4.4: Temporal evolution of temperature, pressure, heat release rate and H radical mass fraction

μs), there is enough fresh mixture ahead of it. The reactive shock wave develops afterwards and collides with the pre-ignition front.

4.2.4 Flame induced auto-ignition

As stated earlier, when a propagating reaction front encounters an adverse gradient in reactivity, it can turn into a contact discontinuity with steep gradients in density, temperature and composition. In internal combustion (IC) engines, compression of the fresh gas mixture due to piston motion and the propagating reaction front further aggravates this process. This phenomenon has also been observed in experimental investigations of IC engines [113–115]. An accurate prediction of front propagation speed under such conditions still remains a challenge. Moreover, the presence of contact discontinuities may render the central difference schemes cost prohibitive due to very fine grid resolution requirements or ineffective in capturing the underlying physics altogether. As such, the importance of the WENO7M scheme to multidimensional reacting flows is further emphasized. To compare the performance of the WENO7M scheme and the CD8 scheme in accurately resolving the physics of reacting flows with contact discontinuities, the computation of an initially planar flame propagating into a compositionally stratified mixture under compression heating is conducted in this part of the study. A two-dimensional (2D) simulation is performed for a rectangular domain with an inlet and outlet along the axis of propagation. The simulation is carried out using both the CD8 and the WENO7M schemes. A uniform mixture of dimethyl-ether (DME) and air, at an equivalence ratio of 0.4, initial temperature of 800 K and an elevated pressure of 20 atm, is considered with the description of chemical kinetics by the mechanism of Bhagatwala et al. [23]. The rectangular domain has a length, $L_{\mathrm{x}} = 9.75$ mm and a width, $L_{\mathrm{y}} = 1.44$ mm. It is discretized with 249,600 points (1300 by 192) with a uniform grid spacing of 7.5 μm (corresponding to at least 12 grid points across the thinnest species reaction rate layer which in the present study has been identified to be CH_3O) when using the WENO7M scheme. The CD8 scheme with an identical grid spacing was noticed to cause spurious oscillations due to its inability to capture the contact discontinuity. As such, a uniform grid spacing of 3.75 μm (corresponding to at least 24 grid points across the thinnest CH_3O reaction rate layer) is required when using the CD8 scheme. As a result, the

total number of grid points required for the CD8 scheme is 4 times higher. Moreover, the solution obtained using the CD8 scheme is filtered at every time step using a tenth-order de-aliasing filter so as to further prevent high wave-number oscillations.

To mimic pressure rise due to piston motion and front propagation, an inert mass source term is added to the governing Equations (1a) to (1d), following the previous approaches [9, 87, 94, 116]. A schematic of the numerical configuration used for this case is shown in Figure 4.5. Pockets of stratified temperature and composition fields are routinely observed to occur in IC engines due to wall heat transfer and imperfect mixing with the residuals. Hence, apart from the addition of inert mass source term to the governing equations, the velocity and temperature at the inlet are held constant whereas the mass fraction of DME at the inlet is varied using a monochromatic 2D sinusoidal wave as:

$$Y_{\mathrm{DME}}(t) = Y_{\mathrm{DME}}(0) + A \sin\left(\frac{2\pi t}{\tau_0}\right) \sin\left(\frac{2\pi y}{\lambda}\right) \tag{4.19}$$

where t is time, A is the wave amplitude, τ_0 is the time period, y is the coordinate along the width of the domain, and λ is the length-scale of the stratification eddies. At all times, the deficit or excess of DME concentration is also compensated by adjusting the air concentration. This configuration corresponds to an IC engine condition wherein a flame propagates into a pocket of stratified concentration field of a certain length scale. Non-reflecting inflow and outflow boundary conditions [88] are also imposed to avoid large pressure waves within the domain. The value of $A = 0.2$ has been chosen such that the root-mean-square of the equivalence ratio at the inlet is of the same order of magnitude as the one that been used in previous studies [8, 9]. In a recent study [77], it was found that stratification eddies, with time scales comparable to the auto-ignition delay times,

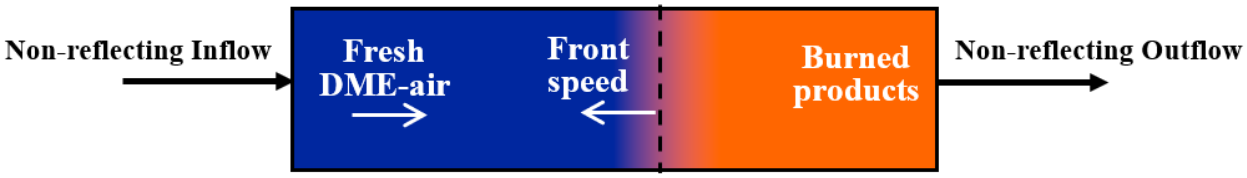

Figure 4.5: Numerical configuration for simulating flame propagation into a compositionally stratified mixture under compression heating

have maximum interaction with the ignition chemistry and significantly affect the front propagation speed. Hence, for the present study, $\tau_0 = 240$ μs and $\lambda = 0.4775$ mm such that the domain has three stratification eddies along the width.

The simulation is initially run till $t = 1.92$ ms with constant inflow velocity and temperature of 2 m/s and 800 K, respectively, such that the flame remains statistically stationary. This is carried out to generate pockets of stratified composition field ahead of the flame without causing any change its propagation speed, S_c (defined as per Equation 4.20). It should be noted that chemistry is active throughout the entire simulation time. At time $t = 1.92$ ms, the fresh gas mixture is isentropically compressed such that the pressure in the domain increases from 20 to 40 atm, such as with the pressure rise due to piston motion and flame propagation. The pressure rise rate is controlled so as to match the combustion duration time in a typical homogeneous charge compression ignition (HCCI) engine [117]. The pressure and temperature at the boundaries are also varied isentropically at the same rate. A comparison of the instantaneous temperature fields obtained using both the CD8 and the WENO7M schemes is shown in Figure 4.6. At $t = 1.92$ ms, the temperature fields obtained using either of the two methods are almost indistinguishable. Once the compression heating is started at $t = 1.92$ ms, the flame begins to propagate towards the inlet by consuming the upstream fresh gas. At the same time, pre-ignition is observed to occur in the upstream fresh gas due to the rise in temperature and pressure caused by compression heating, as can be seen between $t = 2.31$ ms and $t = 2.5$ ms. This is also evident by examining the mass fractions of major (O_2) and minor (OH) species (i.e. Y_{O_2} and Y_{OH}) as depicted in Figures 4.7 and 4.8. The minimum and maximum values of temperature and Y_{O_2} and Y_{OH} obtained using either of the two methods are nearly identical till $t = 2.36$ ms. However, for $t \geq 2.5$ ms, a difference in peak values of the respective quantities obtained using either of the two methods is observed. A lower peak value of temperature, Y_{O_2} and Y_{OH} observed when using the CD8 scheme is mainly due to the application of the de-aliasing filter to the solution vector at every time step.

Compression heating due to piston motion and flame propagation causes the fresh gas to spontaneously auto-ignite, resulting in an abrupt change in temperature and hence density. This leads to the formation of a contact discontinuity which, by definition, is a surface that

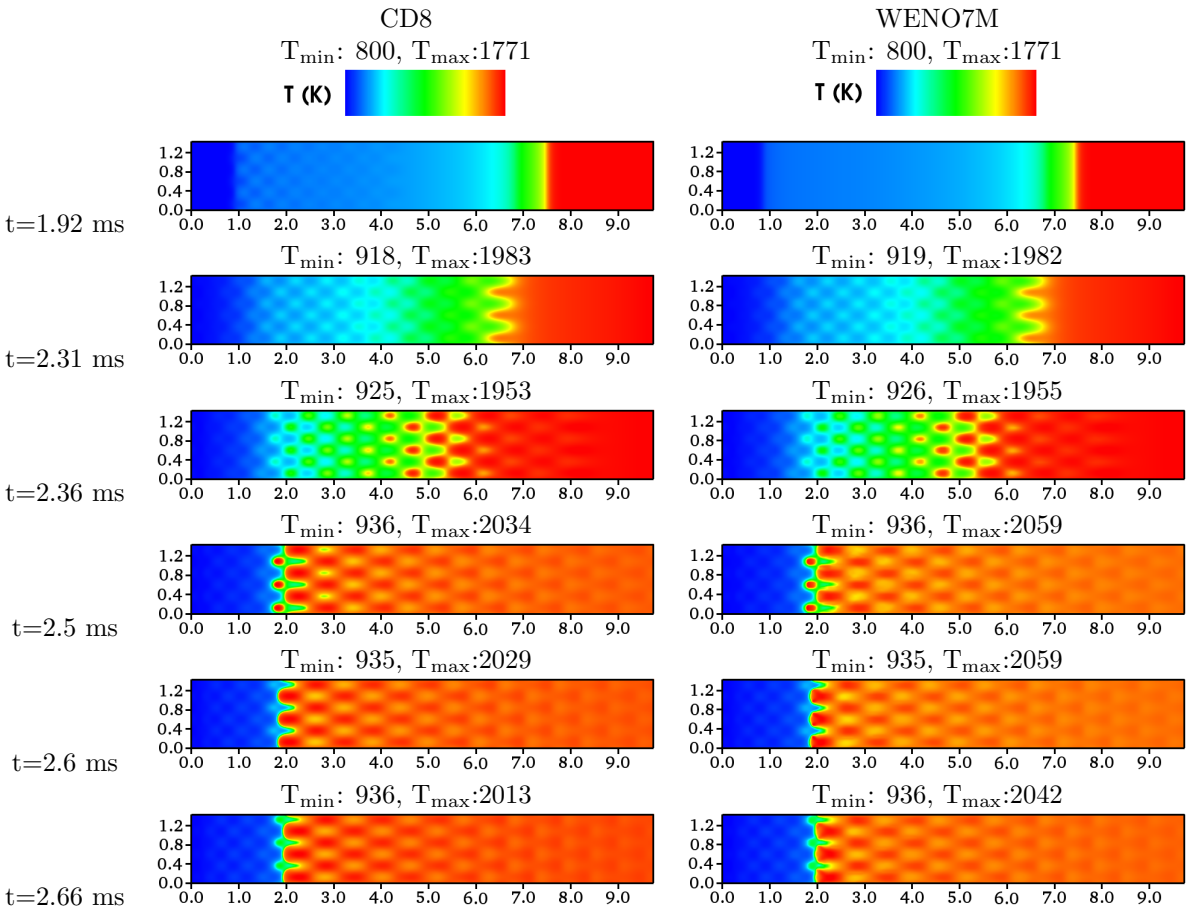

Figure 4.6: Instantaneous temperature fields obtained using the eighth-order centered difference (CD8) scheme and the seventh-order mapped WENO (WENO7M) scheme. The domain dimensions are in mm.

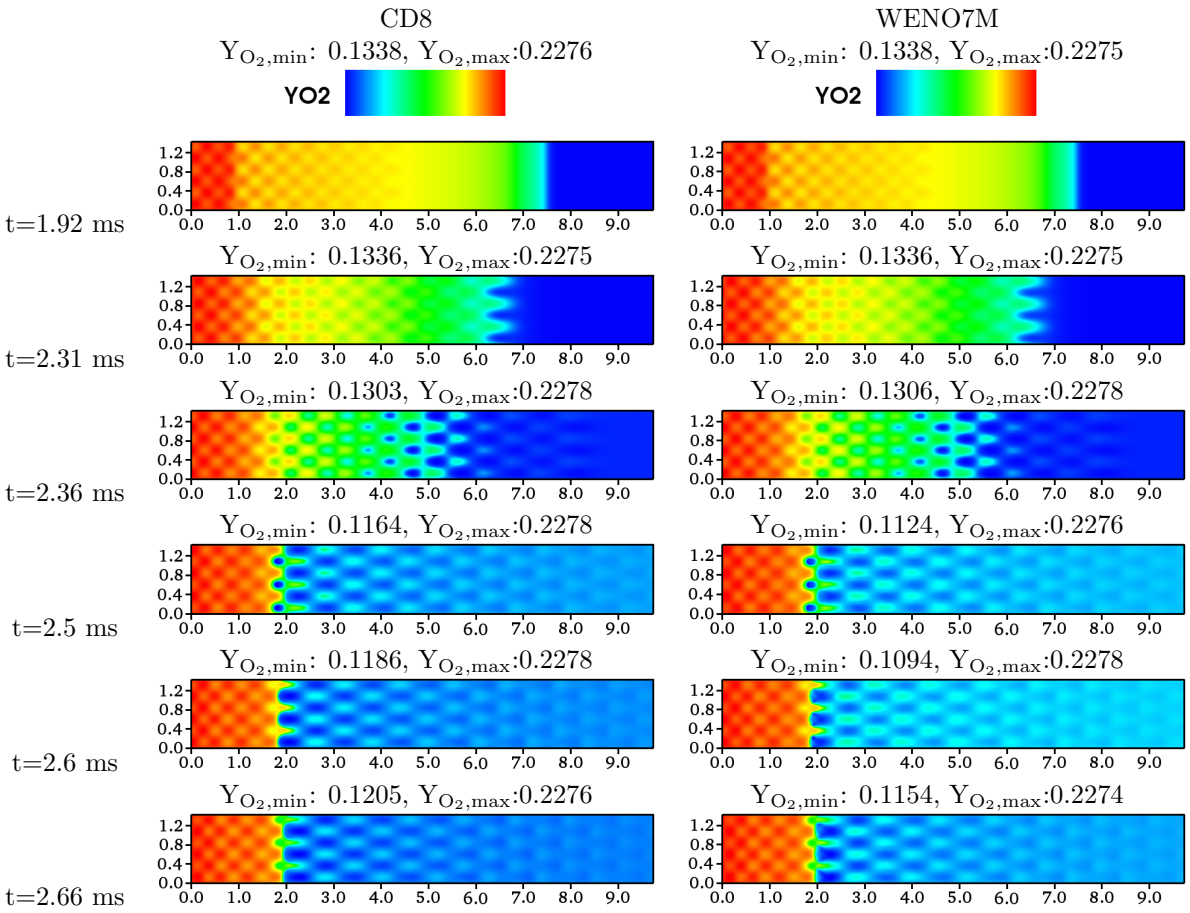

Figure 4.7: Instantaneous mass fraction of oxygen obtained using the eighth-order centered difference (CD8) scheme and the seventh-order mapped WENO (WENO7M) scheme. The domain dimensions are in mm.

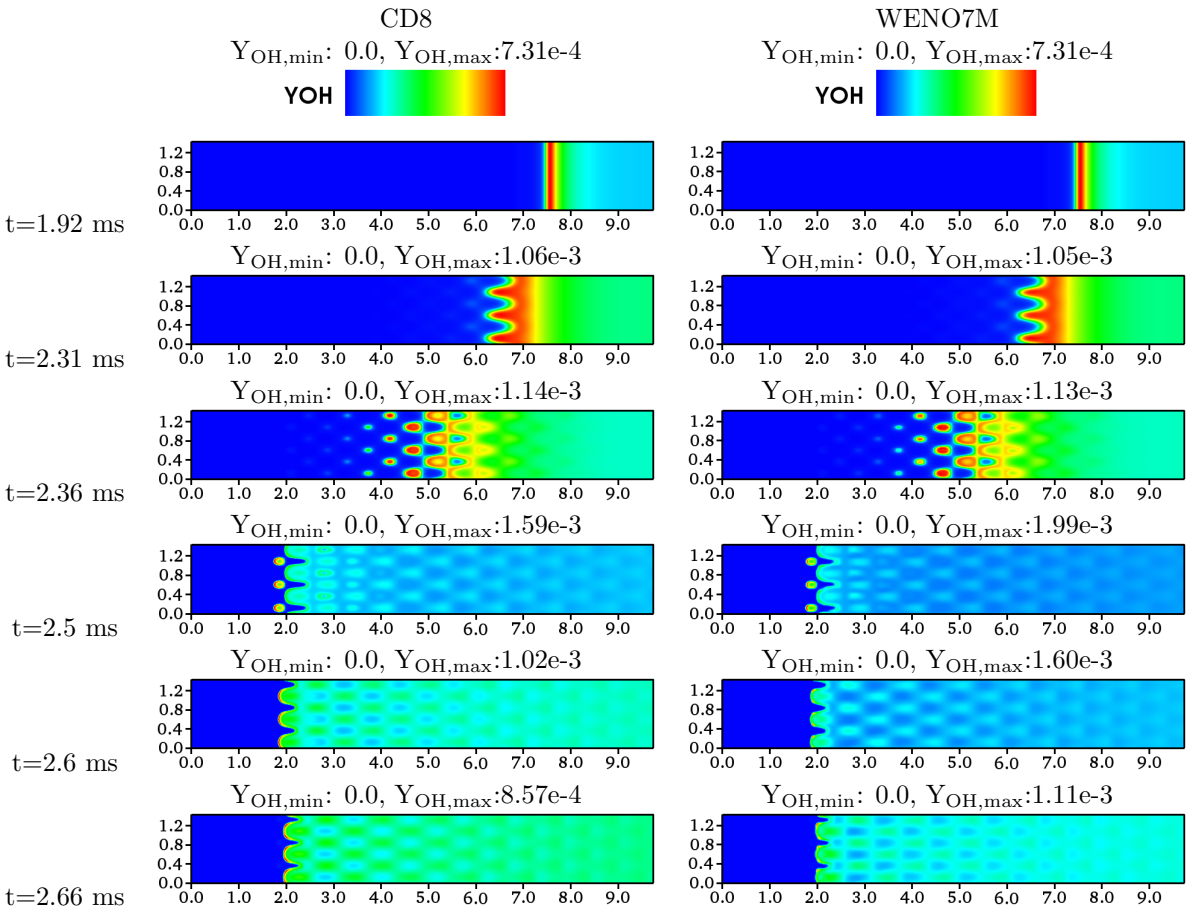

Figure 4.8: Instantaneous mass fraction of hydroxyl (OH) radical obtained using the eighth-order centered difference (CD8) scheme and the seventh-order mapped WENO (WENO7M) scheme. The domain dimensions are in mm.

separates zones of different density and temperature while being in pressure equilibrium. As mentioned earlier, the CD8 scheme created spurious oscillations due to its inability to capture the contact discontinuity when a uniform grid resolution of 7.5 μm was used, leading to an unstable solution. Subsequently, the CD8 scheme provided a stable solution with a finer grid resolution of 3.75 μm. It also necessitated the use of the de-aliasing filter at every time step which is observed to damp out the flow features as well. Unlike the CD8 scheme, the WENO7M scheme remains stable on a coarser 7.5 μm grid and provides insight into the dominant physics at play when a flame propagates into a compositionally stratified mixture under compression heating. The front propagation speed, S_{c}, using either of the two discretization schemes, is computed based on oxygen consumption as:

$$S_{\mathrm{c}} = -\frac{1}{\rho_{\mathrm{u}}(Y^{\mathrm{u}}_{\mathrm{O}_2} - Y^{\mathrm{b}}_{\mathrm{O}_2})} \int_0^{L_{\mathrm{x}}} \int_0^{L_{\mathrm{y}}} \dot{\omega}_{\mathrm{O}_2} \, \mathrm{dy} \, \mathrm{dx} \tag{4.20}$$

where ρ_u is the unburnt gas density, $Y^{\mathrm{u}}_{\mathrm{O}_2}$ and $Y^{\mathrm{b}}_{\mathrm{O}_2}$ is the mass fraction of oxygen in the unburned and burned gas, respectively, and $\dot{\omega}_{\mathrm{O}_2}$ is the oxygen reaction rate. The values of S_{c} obtained with the two discretization schemes at different times is reported in Table 4.1. It can be noticed that S_{c} quickly rises from 2 m/s at 1.92 ms to $\approx$ 24 m/s at 2.36 ms due to multiple pre-ignition events occurring ahead of the flame. As the simulation progresses further in time, S_{c} drops significantly (as observed at 2.66 ms) and eventually stabilizes at 2 m/s which corresponds to the velocity imposed at the inlet. Note that the difference in instantaneous S_{c} obtained using either of the two discretization schemes is negligible, even though the grid spacing used for the CD8 scheme is half that of the WENO7M scheme.

Table 4.1: Instantaneous front propagation speed, S_{c}, obtained using the two discretization schemes

Time (ms)	S_{c} (m/s) (CD8)	S_{c} (m/s) (WENO7M)
1.92	2.00	2.00
2.31	22.44	22.42
2.36	23.56	23.86
2.50	2.91	2.84
2.60	1.24	1.23
2.66	1.50	1.39

In the following section, we present the performance characteristics of KARFS, including weak scalability, strong scalability as well as GPU scalability, using both the CD8 and WENO7M schemes. Additionally, the performance of the operator splitting scheme using GPU acceleration is also presented using detailed chemical mechanisms of different sizes.

4.3 Performance Characteristics

In this section, the performance characteristics of KARFS and its scalability using different block sizes are presented. The primary system used in this work is the Titan supercomputer at the Oak Ridge Leadership Computing Facility (OLCF). Titan is a hybrid-architecture Cray XK7 system, consisting of 18,688 compute nodes that are interconnected by Cray's Gemini network. Each node is composed of a 16-core AMD Opteron processor and an NVIDIA Tesla K20X graphics processing unit (GPU) as an accelerator. Moreover, each node has 32 GB of memory on the host Opteron processor and 6 GB memory on the GPU accelerator.

The particular benchmark test, herein referred to as the "Quiescent Test", involves integrating the governing equations (1a–1d) over 10 time steps. The computational domain consists of a periodic cube containing air at a temperature of 800 K and an elevated pressure of 20 atm. Nevertheless, the description of chemical kinetics is specified using the 30 species dimethyl-ether mechanism [23] which consists of 175 reactions as well as 9 species identified as global quasi-steady state species. As such, the performance characteristics obtained herewith are representative of an actual production DNS run. The performance characteristics of the newly implemented WENO7M scheme are compared with those of the existing CD8 scheme. The time taken to advance the solution field over a known number of time steps is measured in the performance tests. It should be noted that the time reported here represents the total time to solution and not just the time taken by the advection operators. Specifically, the reported times consist of the time spent in the Runge–Kutta time loop including each of the six sub-stages, time spent for calculating the right-hand-side terms of the governing Equations (1a) to (1d) including the viscous fluxes, the diffusive fluxes as well as the chemical source terms, plus the time taken to apply the de-aliasing filter. Only the I/O

time has been excluded from the benchmark test as this can limit scalability. The chemical source terms are independent of the spatial derivative operators used in the transport solvers. As such, GPU acceleration of the chemical source terms has been excluded. Note that, oftentimes, only the speedup obtained using the different parallelism strategies is reported while the computational cost in terms of node-time is rarely discussed. In the present study, the computational performance is quantified using a metric for the computational time per grid point per time step in terms of node-time as

$$\text{Cost} = \frac{\text{number of nodes} \times \text{wall clock time}}{\text{number of grid points} \times \text{number of time steps}}. \tag{4.21}$$

4.3.1 MPI weak scalability

An MPI weak scalability study is performed on up to 8788 nodes (140,608 cores) for two block sizes: 16^3 and 32^3. The two block sizes have been chosen such that they are neither too small for the high-order discretization methods being investigated nor too big to mask the underlying deficiencies of the DNS code. To fully utilize all the processing cores on the node, 16 MPI tasks are placed on each node irrespective of the block size. We note that neither GPU nor OpenMP threading is utilized for weak scalability. Figure 4.9 shows the performance of KARFS while scaling from 4 nodes to 8788 nodes on the Titan system.

Irrespective of the block size, the WENO7M scheme is found to be about twice as expensive compared to the CD8 scheme. This is primarily because of the additional computations that are needed when using the WENO7M scheme including flux-splitting, interpolation and separate flux evaluations. It is observed that weak scaling is nearly perfect for the selected block sizes when the CD8 scheme is used for evaluating the spatial derivatives. The WENO7M scheme also shows excellent weak scalability till around 2000 nodes for the larger block size of 32^3, beyond which its computational cost begins to increase linearly. The weak scalability of the WENO7M scheme deteriorates more rapidly for the smaller block size of 16^3. In each case, the reason for the observed rise in computational cost is twofold: 1) increasing the number of nodes increases the amount of time spent in MPI communications and 2) as discussed earlier in Section 4.1, extra time for MPI communications is added while

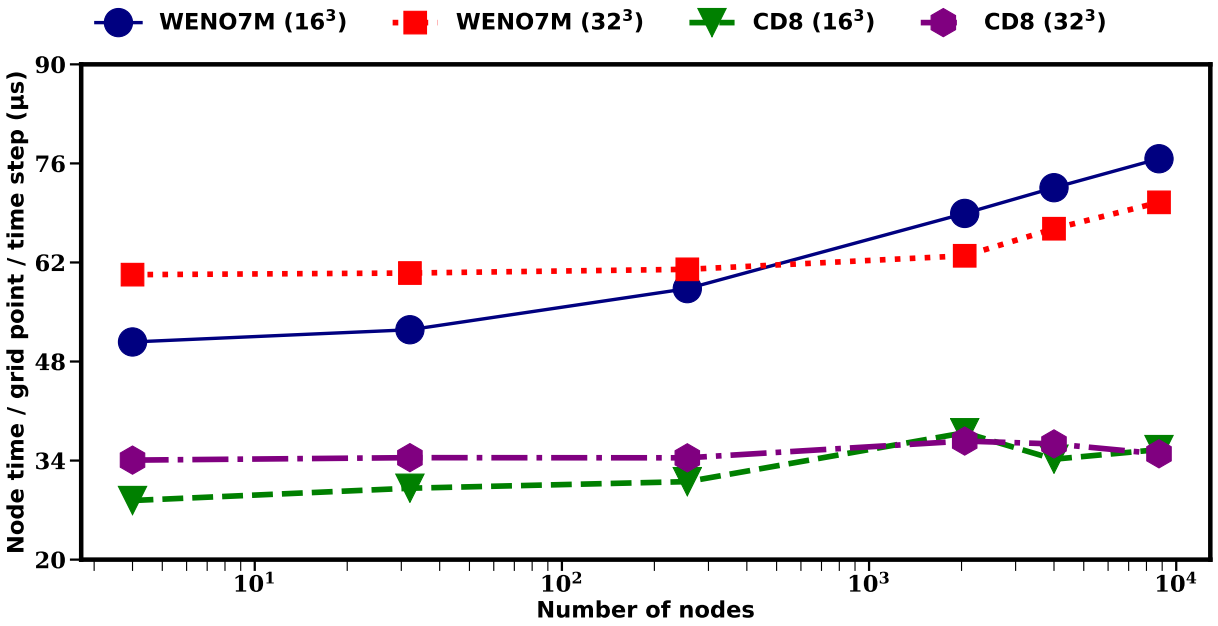

Figure 4.9: MPI weak scalability of KARFS. The block size per MPI as well as the discretization scheme for each case is indicated.

evaluating the numerical fluxes at the left cell boundary when using the WENO7M scheme.

4.3.2 OpenMP scalability

In this section, the effects of multi-threading on the performance of KARFS is investigated by using both numerical discretization schemes (CD8 and WENO7M) for two block sizes: 16^3 and 32^3. For this part of the study, 64 nodes are utilized, each with 1 MPI task. Also, on each node, the number of threads per MPI task is varied from 1 to 16. Results are shown in Figure 4.10.

For the smaller block size of 16^3, multi-threading provides a substantial reduction in the computational cost for the WENO7M scheme when the number of OpenMP threads is increased from 1 to 2. A similar trend is observed for the CD8 scheme until the number of OpenMP threads is increased to 4. Further increase in the number of OpenMP threads degrades the performance of both schemes. This is mainly because of two reasons: 1) there is not enough work for each thread and 2) OpenMP thread creation and synchronization result in an additional time overhead. However, as the block size is increased to 32^3, an

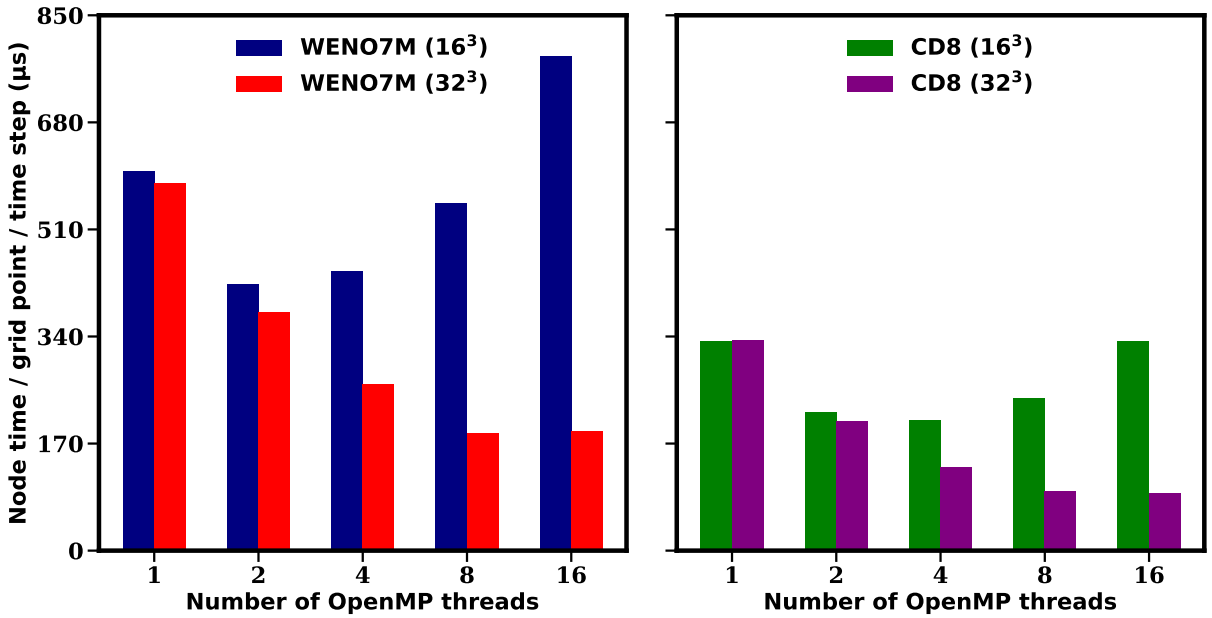

Figure 4.10: OpenMP scalability of KARFS. The block size per MPI as well as the discretization scheme for each case is indicated.

improved OpenMP scalability is observed while using either of the numerical schemes. The overall computational cost of each scheme is reduced by more than 67% when the number of OpenMP threads is increased from 1 to 8. A marginal degradation in OpenMP scalability is observed for each scheme when the number of OpenMP threads is increased from 8 to 16 due to the reasons stated above. In addition, the computational cost of the WENO7M scheme remains about twice that of the CD8 scheme, irrespective of the number of OpenMP threads, as has been already observed in the previous section.

It is also interesting to note that regardless of the numerical scheme or the number of OpenMP threads, the computational cost associated with MPI + OpenMP is higher than MPI only. To explain this, it is important to understand the difference between "Speedup" and "Cost". Table 4.2 shows a comparison of Speedup and Cost for the MPI + OpenMP and MPI-only strategies when using the CD8 scheme for a block size of 32^3. It can be seen that the total time to advance the solution field over a known number of time steps is smaller for MPI + OpenMP, irrespective of the number of OpenMP threads, than the MPI only strategy. As a result, there is a definite "Speedup" in performance. However, since more nodes are utilized in the former, the "Cost" of MPI + OpenMP is significantly higher.

Table 4.2: Comparison of "Speedup" and "Cost" of MPI + OpenMP versus MPI only strategies when using the CD8 scheme for a block size of 32^3. Speedup = Time (MPI only) / Time (MPI + OpenMP).

NX	NY	NZ	px	py	pz	MPI tasks	Nodes	OpenMP threads	Time (s)	Speedup	Cost
32	32	32	4	4	4	64	4	-	169.15	-	32.26
32	32	32	4	4	4	64	64	1	109.65	1.54	334.62
32	32	32	4	4	4	64	64	2	67.54	2.5	206.11
32	32	32	4	4	4	64	64	4	43.21	3.91	131.87
32	32	32	4	4	4	64	64	8	31	5.46	94.6
32	32	32	4	4	4	64	64	16	30.1	5.62	91.85

4.3.3 MPI strong scalability

Here, we investigate the strong scalability of KARFS with a fixed problem size while increasing the number of nodes in successive runs. Specifically, the problem size is kept constant at 256^3 with an initial block size of 128^3 partitioned into 8 MPI tasks on a single node. For subsequent runs, the block size is progressively halved by doubling the number of MPI tasks in each direction until it becomes 16^3. Note that neither GPU acceleration nor OpenMP threading is employed for this part of the study. As shown in Figure 4.11, the computational cost of both numerical schemes reduces considerably when the number of nodes is increased from 1 to 4. However, the reduction in computational cost for each numerical scheme is rather gradual as the number of nodes is further increased to 32 and subsequently to 256. This is mainly because, as the number of nodes is increased, the MPI communication overhead also increases. Moreover, with an increase in the number of nodes, the amount of work available for each core on a given node also decreases.

In addition, results obtained after converting the "Cost" (node time/grid point/time step) metric to "Time" metric are shown in Figure 4.12. This is done to clearly demonstrate excellent strong scaling of KARFS while using either of the two discretization schemes. The log-log plot for the data is very similar to what would be expected for ideal scaling: a straight line for strong scaling. As has been observed before, the computational cost of the WENO7M scheme is about twice that of the CD8 scheme. Note that domain decomposition less than 16^3 was not possible in the present study since both CD8 and WENO7M operators used in KARFS require at least an 8-point and a 7-point stencil respectively.

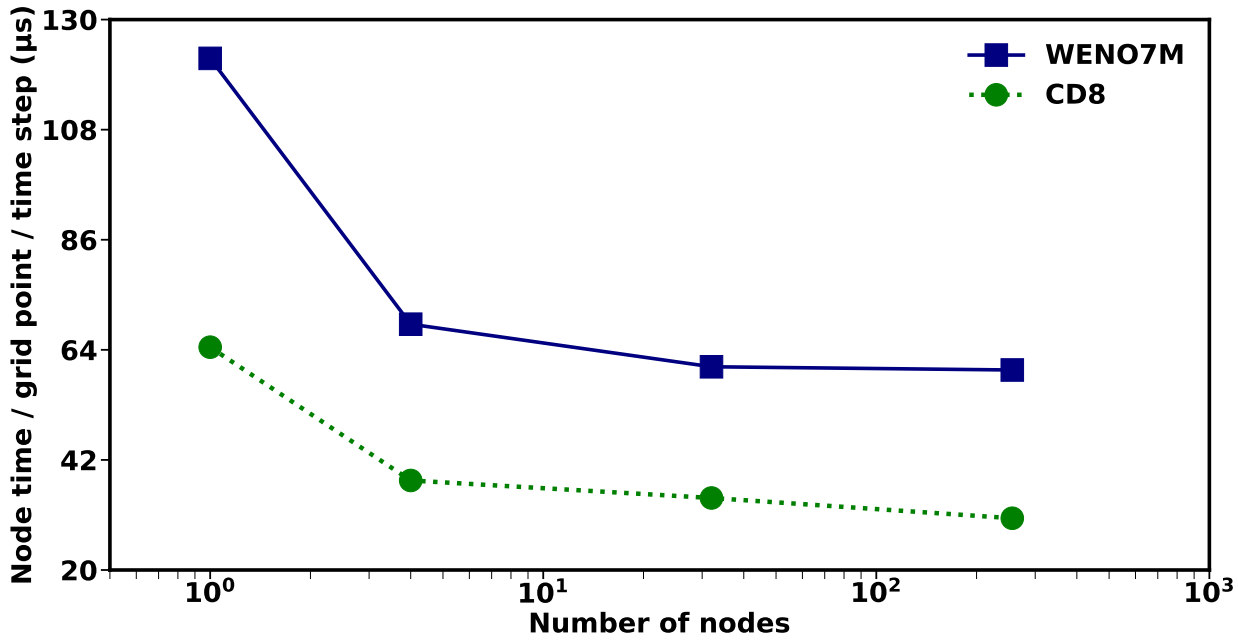

Figure 4.11: MPI strong scalability of KARFS using "Cost" metric

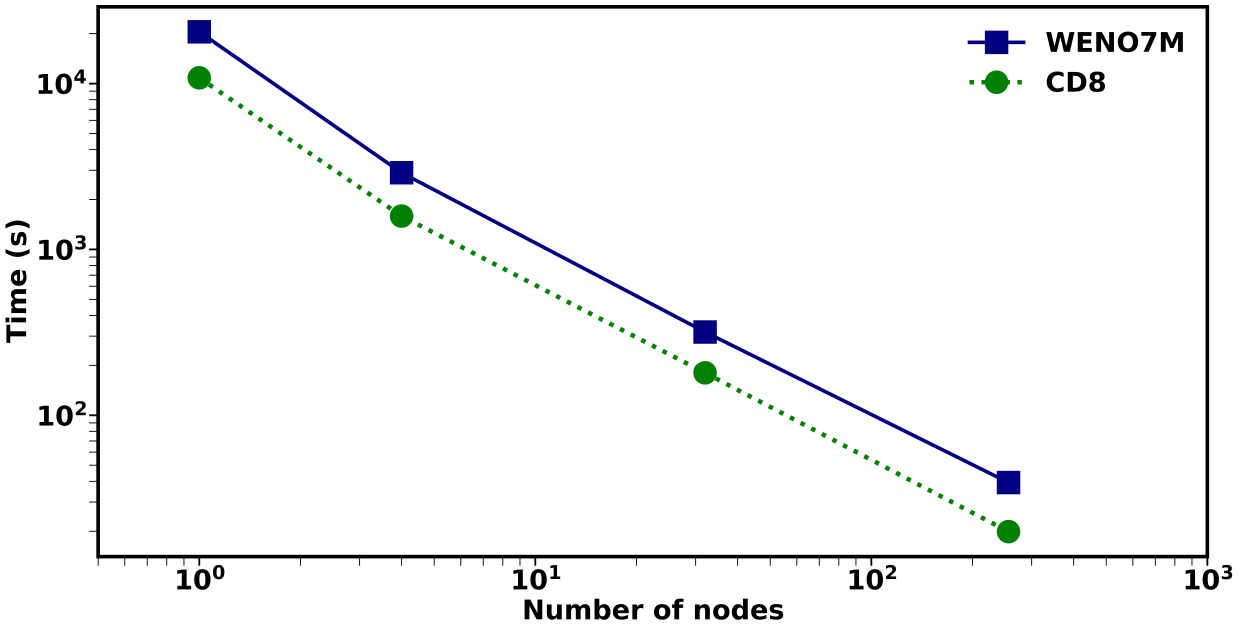

Figure 4.12: MPI strong scalability of KARFS using "Time" metric

It is also well-known that strong scaling is limited by Amdahl's law [118], wherein the maximum "Speedup" achievable is limited by the serial part of the code. Amdahl's law can be formulated as:

$$\text{Speedup} = \frac{1}{(S + \frac{P}{N})} \tag{4.22}$$

In Equation 4.22, N represents the number of cores used. S represents % of serial portion of KARFS while P represents % of parallel portion of KARFS such that $S + P = 100$. Here, "Speedup" is defined based on the ratio of measured wall-clock time at the lowest core count to the actual measured time. For an obtained value of "Speedup", the values of S and P can be determined using equation 4.22. Table 4.3 shows the speedup achieved in the strong scaling study using both the CD8 and WENO7M schemes. It can be noticed that, at the highest core count, more than 99% of KARFS has been parallelized. As such, almost the entire portion of KARFS is parallelizable, and there is no lack of strong scalability. From the above table, it can also be seen that when the WENO7M scheme is used, the obtained speedup as well as the resulting percentage of the parallel portion is higher when the number of cores is between 8 and 512. This is expected since the WENO7M scheme involves more operations compared to the CD8 scheme. Increasing the number of cores to 4096 results in marginal degradation of the WENO7M performance. This has also been observed in the weak scaling results discussed in section 4.3.1. It is mainly due to 1) an increased amount of time spent in MPI communication resulting from the increase in number of nodes/cores, 2) extra time for MPI communication being added while evaluating the numerical fluxes at the left cell boundary when using the WENO7M scheme.

Table 4.3: Strong scaling analysis based on Amdahl's law.

CD8						WENO7M					
Nodes	Cores	Time (s)	Speedup	S	P	Nodes	Cores	Time (s)	Speedup	S	P
1	8	10826.81	1	100.0	0.0	1	8	20509.78	1	100.0	0.0
4	64	1589.29	6.81	13.33	86.67	4	64	2899.25	7.07	12.78	87.22
32	512	180.32	60.04	1.47	98.53	32	512	317.80	64.54	1.36	98.64
256	4096	19.89	544.39	0.16	99.84	256	4096	39.30	521.84	0.17	99.83

4.3.4 GPU scalability

In this section, the performance of KARFS with GPU acceleration is compared against its OpenMP scalability by using four different block sizes: 16^3, 32^3, 64^3, and 96^3. Furthermore, to demonstrate KARFS portability, the benchmark runs are also performed on a developmental system at ORNL consisting of 8 compute nodes, each with two NVIDIA Tesla P100 accelerators. Each GPU accelerator has a memory of 16 GB. A number of combinations for the MPI+X hierarchical parallelism of KARFS, where "X" stands for OpenMP or CUDA backends, are tested, and the respective computational cost for each discretization scheme is shown in Figures 4.13 and 4.14. Since the focus of this part of the study is to solely evaluate the performance of CD8 and WENO7M schemes with GPU acceleration, the chemistry has been frozen (i.e., the term $\dot{\omega}_k$ in equation (1d) is not evaluated) for these bench-marking runs.

Figure 4.13 shows the performance of KARFS when using the CD8 numerical scheme. It is seen that for a block size of 16^3, the MPI + OpenMP parallelism strategy results in a lower computational cost than MPI + CUDA. CUDA has a start-up overhead and for a small block size of 16^3, the start-up overhead outweighs any gains from using the GPU. As the block size is increased to 32^3, a significant reduction in the computational cost is observed for the MPI + CUDA strategy compared to MPI + OpenMP. Moreover, the resulting computational cost with the Tesla P100 GPU is about half that of the Tesla K20X GPU. For the two larger block sizes of 64^3 and 96^3, there is no noticeable change in the computational cost with MPI + OpenMP. However, the computational cost decreases even further with MPI + CUDA. Note also that for the two smaller block sizes of 16^3 and 32^3, the computational cost of MPI + CUDA is significantly higher than the MPI-only strategy. These results demonstrate that domains with larger block sizes could be efficiently run on a significantly smaller number of nodes with GPUs.

The performance of KARFS when using the WENO7M is shown in Figure 4.14. The computational costs obtained for the different block sizes are qualitatively similar to those obtained using the CD8 scheme. Additionally, as has been observed in the previous sections, the respective costs for the WENO7M scheme are higher than those for the CD8 scheme.

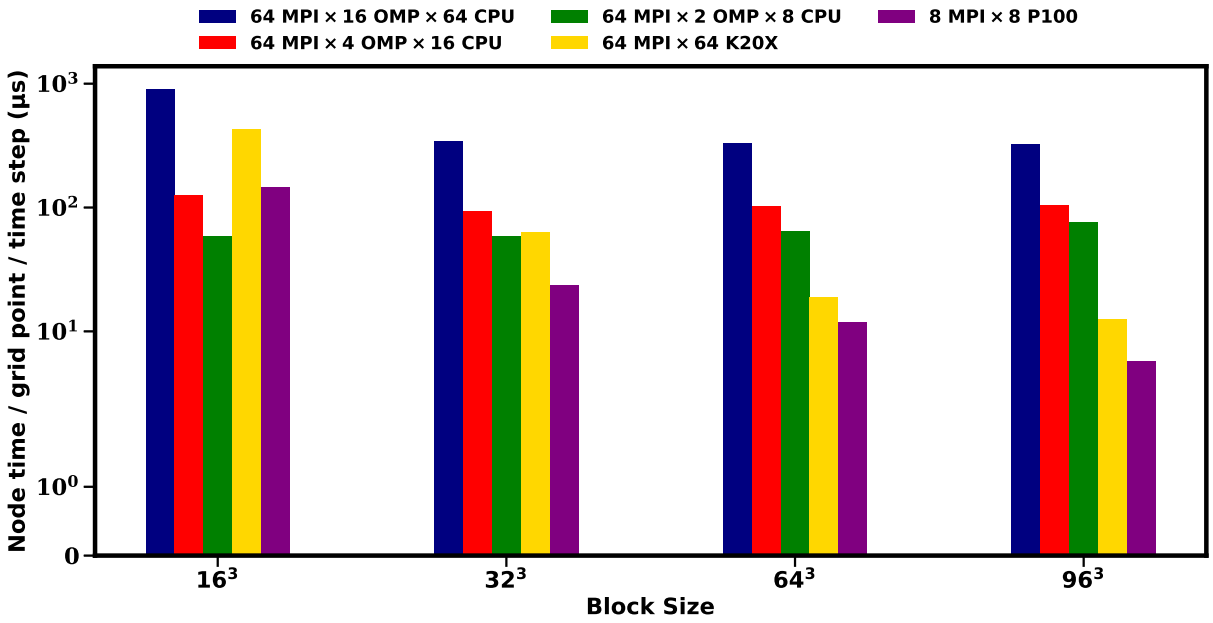

Figure 4.13: Performance of KARFS when using the CD8 numerical scheme. 1 CPU = 16 cores.

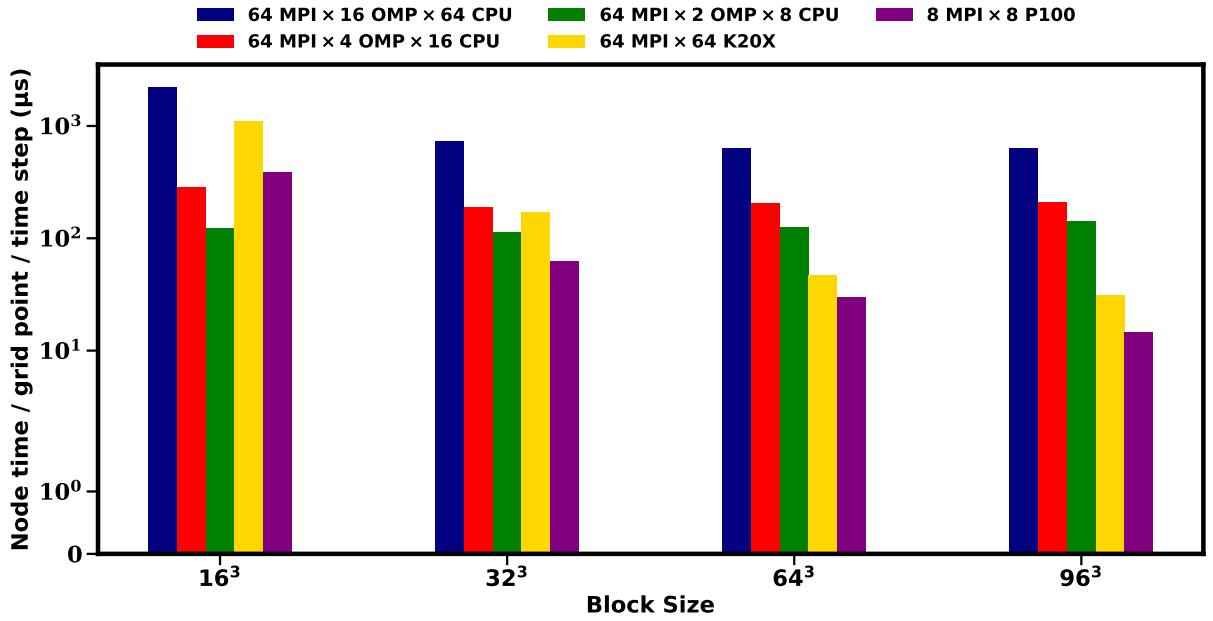

Figure 4.14: Performance of KARFS when using the WENO7M numerical scheme. 1 CPU = 16 cores.

4.4 Concluding remarks

Using the MPI+X programming model, the implementation and validation of multiple WENO schemes in KARFS is demonstrated. The MPI+X programming model relies on Kokkos for performance portability to multi-core, many-core and GPUs. The capability and potential of the newly implemented WENO schemes in KARFS to perform DNS of compressible flows is also demonstrated with model problems involving shocks, isotropic turbulence, detonations and flame propagation into a stratified mixture with complex chemical kinetics. It is demonstrated that the power parameter p in the WENO schemes can be modified to increase or decrease the dissipation of the employed WENO scheme. As such, the WENO-Z scheme [104] is found to be best suited for performing DNS of turbulent reacting flows in the absence of shocks.

In addition, performance and scalability of KARFS using the two spatial discretization schemes (eighth-order central difference (CD8) and seventh-order, mapped WENO (WENO7M)) is evaluated to provide estimates that can be used for an appropriate load-balanced decomposition of future production simulations. The computational performance is quantified using a metric termed as "Cost" for the computational time per grid point per time step so as to provide a better estimate of the computational resources (i.e. node/core hours). Across the different scaling studies, it is revealed that the cost of WENO7M scheme is about two to three times higher than the CD8 scheme, mainly due to an increase in the amount of computations involved in the former. In the weak scaling studies, the code shows almost perfect scaling when using the CD8 scheme. Meanwhile, the performance deteriorates with an increase in the number of nodes when the WENO7M scheme is used. An increase in the amount of time spent in MPI communications is found to be majorly responsible for such degradation in performance. Based on Amdahl's law analysis, the code demonstrates perfect strong scaling in terms of reduction in wall-clock time. However, the reduction in cost of both the numerical schemes is found to gradually subside with an increase in the number of nodes which is a direct consequence of the increased utilization of computational resources.

A marked speedup is obtained when MPI + OpenMP strategy is used, especially for the larger block size. However, irrespective of the block size, the computational cost of MPI + OpenMP is found to be significantly higher as compared to MPI only strategy. This is due to an increase in the number of nodes being used at a given time with MPI + OpenMP strategy. From the GPU scaling studies, it is found that block sizes larger than 32^3 are needed to overcome the startup overhead associated with MPI + CUDA strategy and subsequently achieve a reduction in computational cost of each numerical scheme. Nonetheless, the MPI + CUDA strategy with larger block sizes results in the usage of smaller number of nodes and also leads to a substantial reduction ($\approx 90\%$) in the computational cost of each numerical scheme in comparison to MPI + OpenMP strategy. With regards to GPU acceleration of the operator splitting scheme, a significant speedup is achieved, as the size of reaction mechanisms increases. It is also found that the dependence of speedup on the grid size is relatively minor since the GPU is exclusively used in the linear-algebraic operations associated with operator splitting.

Chapter 5

Effects of temperature and composition stratification on turbulent flame propagation at auto-ignitive conditions

In this chapter, direct numerical simulations (DNS) of 2D turbulent flames in a stratified dimethyl-ether (DME)/air mixture are conducted at auto-ignitive conditions using a statistically stationary planar configuration. Under the chosen conditions, the initial laminar flame is strongly affected by auto-ignition, which is expected to occur under engine conditions, and exhibits a multi-staged (i.e. cool + hot) ignition front structure. As such, the corresponding laminar flame speed, S_{L}, is found to be highly dependent on the position of the hot reaction front from the inlet. Three sets of conditions with an identical turbulence intensity but different stratification/turbulence length scales and correlations between temperature (T) and equivalence ratio (ϕ) fields are simulated to study the dynamics of turbulent stratified flame propagation at auto-ignitive conditions. The influence of different length scales and T-ϕ correlations on the mean turbulent cool as well as the hot reaction front structure is examined by comparing the flame statistics obtained from 2D simulations against the corresponding laminar 1D solution. A global analysis of the front

propagation speed is carried out to determine the individual contributions of flame wrinkling (A') and the enhancement of burning rate per unit length (I_0) to the overall burning rate.

In an attempt to quantify and model the influence of turbulence on premixed combustion, a premixed flame is treated as a surface separating the fresh reactants and burnt products. This allows the influence of turbulence on combustion to be distinguished into two important phenomena: (i) an increase in the flame surface area within the same volume through wrinkling and aerodynamic straining of the flame, and (ii) a change in the burning rate of the flame per unit surface area with respect to a laminar flame. Based on this concept, a model for turbulent burning velocity has been suggested by Bray [119] and Candel and Poinsot [120]. In this model, the mean turbulent burning velocity can be written as:

$$S_{\mathrm{T}} = S_{\mathrm{L}} \cdot I_0 \cdot A' \tag{5.1}$$

where S_{L} is the laminar burning velocity, I_0 is the efficiency factor to account for change in burning velocity per unit length, and A' accounts for the increase in flame length. Formulating turbulent burning velocity in this manner allows models to be derived for the two contributing factors, I_0 and A'. However, the aforementioned model for turbulent burning velocity presumes the fuel/air mixture to be non-reactive at upstream of the flame. As a result, S_{L} is assumed to have a unique value, irrespective of the domain size or the flame location from the inlet. However, Refs. [16, 21, 77] have demonstrated a strong dependence of S_{L}, to the location of hot reaction front from the inlet. As such, in the present study, we relate the turbulent burning velocity to the one-dimensional propagation speed, S_{1D} (instead of S_{L}), through I_0 and A' for quantifying the effect of turbulence length scales and upstream reactivity on the global burning velocity as:

$$S_{\mathrm{T}} = S_{\mathrm{1D}} \cdot I_0 \cdot A' \tag{5.2}$$

S_{1D} in Equation 5.2 is obtained by relating the location of peak heat release rate in the mean turbulent reaction front to that of a steady 1D laminar flame solution as previously demonstrated in [21, 77]. Furthermore, to account for the contribution of upstream reactivity to the overall burning rate, S_{1D} is defined as:

$$S_{1D} = S_R \cdot I_R \tag{5.3}$$

where S_R is the reference laminar burning velocity at auto-ignitve conditions evaluated as per the methodology suggested in [21] and I_R accounts for the contribution from upstream reactivity to the overall burning rate. Expressing the turbulent burning velocity in this way permits evaluation of individual contributions of I_0, A' and I_R to S_T. Although turbulence is inherently three-dimensional, the present 2D study is a first step in understanding the effects of inhomogeneties in both temperature and equivalence ratio on turbulent flame propagation at conditions which are representative of PCI engines. Dimethyl ether (DME) has been chosen for the present study since it is one of the simplest fuel molecules that exhibits multi-stage ignition and negative temperature coefficient (NTC) behaviour.

5.1 Numerical method and initial conditions

The simulations are performed using the DNS code KARFS [31], which solves the fully compressible Navier-Stokes, species and energy equations. To deal with contact discontinuities encountered due to the rapid heat release rate in the computational domain, a 7^{th} order mapped weighted essentially non-oscillatory (WENO) [106] scheme is implemented for the convective terms. For the diffusive terms, a high-fidelity finite difference method with 8^{th} order central difference [24] is employed. The solution is advanced in time with a 4^{th} order, 6-stage explicit Runge-Kutta scheme [44] using a constant time step of 10 ns. A reduced DME chemical mechanism [23] consisting of 30 species and 175 reactions and an additional 9 species identified as global quasi-steady state species is used in the present study.

Figure 5.1 presents a schematic diagram of the turbulent flame configuration. A 2D statistically planar, freely propagating DME/air flame with an unburned mixture temperature of 800 K, ϕ=0.4 and an elevated pressure of 20 atm is chosen to study the effects of turbulence and stratification on the dynamics of turbulent flame propagation at auto-ignitive conditions. The simulation is initialized using a laminar solution obtained from Cantera [1] with a fixed inflow velocity of 2 m/s. The computed inflow velocity under such

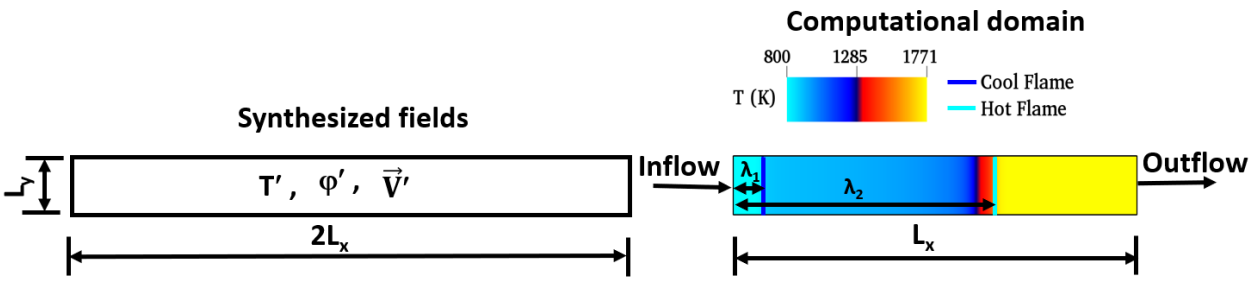

Figure 5.1: Schematic diagram of the flow configuration

conditions corresponds to the steady propagation speed, S. Periodic boundary condition in the y-direction and non-reflecting inflow and outflow [88, 89] in the x-direction have been used. λ_1 and λ_2 in Figure 5.1 represent the location of stabilization (measured at the points of maximum heat release) of the cool flame and the hot flame respectively.

Under the chosen unburned mixture conditions, a stable freely propagating double flame (i.e. a coupled cool flame and a hot flame) could not be obtained as the characteristic residence time ($= \int_0^{\lambda_1} \frac{1}{u(x)} dx$, where u(x) is the local flow velocity) is within an order of magnitude from the first-stage ignition delay. The laminar flame solution has been found to be strongly dependent on the flame location away from the inlet at such conditions [16, 21, 77]. As such, at low inflow velocities, a stable flame can only be attached to the inlet (see Figure 5.3). Such a flame cannot be used to initialize turbulent flames while avoiding interference from the imposed boundary conditions at the inlet. Hence, an ignition front propagating at 2 m/s is used. Moreover, $S = 2$ m/s is of the same order as that of the reference laminar flame speed at auto-ignitive conditions estimated in [21]. This made it possible to maintain the reaction front at a sufficient distance away from the inlet and avoid interference of the boundary conditions at the same time. Externally synthesized turbulent velocity, composition and temperature fields were then injected at the inlet in addition to the mean inflow velocity, temperature and composition. The initial turbulent flow field is synthesized by using an isotropic kinetic energy spectrum function by Passot-Pouquet [110]. The most energetic turbulence length scale, l_e, is varied from 480 to 960 μm, which is of the same order as recently measured in an optical engine [90]. In real engines, the turbulence time scale, τ_t is comparable to τ_{ignition} [94]. Therefore, based on the two homogeneous ignition delay times under the chosen conditions, τ_1 and τ_2, velocity fluctuation RMS, u', of

0.4 is selected to match τ_t with $\tau_{ignition}$. $u' = 0.4$ also ensured that there were no negative inlet velocities. Composition and temperature fields were also synthesized from the same energy spectrum as turbulence but with different random seeds. The various physical and numerical parameters used in the present study are listed in Table 5.1. A uniform grid spacing, Δ, of 7.5 μm is sufficient to fully resolve the chemistry (at least 12 grid points across the thinnest radical reaction rate layer, CH_3O). The Kolmogorov length scale, l_k, is estimated as $l_k = (\nu^3/\epsilon)^{1/4}$ where $\nu = 4.1 \times 10^{-5}$ m^2/s is the kinematic viscosity at the inflow conditions, and ϵ is the turbulence energy dissipation rate. For the present study, chemistry (i.e. the thinnest radical reaction rate layer) rather than Kolmogorov length scale is found to be the limiting parameter that determined the required Δ for ensuring grid convergence. In all cases, the characteristic length scale of temperature fluctuations, l_T, and the characteristic length scale of composition fluctuations, l_{DME}, were selected identical to the most energetic turbulence length scale, l_e, so as to have the most effective turbulent mixing of the mixture [121]. The case labels suffixed with N had a negatively correlated T-ϕ distribution whereas those suffixed with R had an uncorrelated T-ϕ distribution. The number in the case labels denotes the length scale in μm. The values of temperature fluctuations RMS, T' and the composition fluctuation RMS, ϕ' were chosen such that the

Table 5.1: Simulation parameters

Case	**480N**	**480R**	**720N**	**720R**	**960N**	**960R**
Domain size (L_x, mm $\times$ L_y, mm)	**11.52 x 1.44**		**12.96 x 2.16**		**12.96 x 2.88**	
Mesh size ($N_x \times N_y$)	**1536 x 192**		**1728 x 288**		**1728 x 384**	
Uniform grid spacing, Δ (μm)	**7.5**					
Thermal Thickness, L_f (μm)	**350**					
Cool flame stabilization location, λ_1 (mm)	**0.87**					
Hot flame stabilization location, λ_2 (mm)	**7.43**					
First homogeneous ignition delay time, τ_1 (ms)	**0.48**					
Last homogeneous ignition delay time, τ_2 (ms)	**3.06**					
Reference laminar flame speed, S_R (m/s)	**0.32**					
Kolmogorov length scale, l_k (μm)	**95**		**105**		**112**	
Turbulence intensity (u'/S_R)	**1.25**					
$l_e = l_T = l_{DME}$ (μm)	**480**		**720**		**960**	
Temperature fluctuation RMS, T′ (K)	**15**					
Composition fluctuation RMS, ϕ'	**0.1**					
Turbulence time scale, τ_t (ms)	**1.2**		**1.8**		**2.4**	
$U_{in} = S = S_T$ (m/s)	**2**					
Karlovitz Number, Ka (L_f/l_k)	**3.69**		**3.33**		**3.10**	
Flow through time, τ_f (ms)	**5.76**		**6.48**		**6.48**	

range of temperature and composition distribution closely matched the observations of Wang et al. [122].

Based on the mean inlet velocity, $U_{\text{in}} = 2$ m/s, the flow-through time, τ_{f}, varied from 5.76 to 6.48 ms in the respective cases. The solution is advanced for two flow-through times in each case. The first flow-through time is neglected from analysis to remove any effects due to initial transients. Data from equally spaced time instants from the remainder of the simulation are used to obtain the statistical results. Averaging is performed in time and the y-direction.

5.2 1D analysis

To identify a reference laminar flame speed, the method proposed in [21] was followed. A series of steady-state flame solutions were evaluated in Cantera [1] by varying the flame position, λ_2 (based on the location of maximum heat release rate), for which the correct inflow velocity, U_{in} was determined as an eigenvalue. Figure 5.2 presents λ_1 and λ_2 as a function of U_{in}. The derivative $\mathrm{d}\lambda_2/\mathrm{d}U_{\text{in}}$ vs. U_{in} is also shown. A distinguishable peak in $\mathrm{d}\lambda_2/\mathrm{d}U_{\text{in}}$ can be seen at the inflow velocity of 0.32 m/s. As per the argument provided in [21], this value corresponds to the reference laminar flame speed, S_{R}. Based on this value of S_{R}, the non-dimensional turbulence intensity (u'/S_{R}) is 1.25. Due to the presence of two separate reaction fronts, two different one-dimensional propagation speeds, $S_{\text{1D,cool}}$ and $S_{\text{1D,hot}}$ were evaluated by relating the time-averaged values of λ_1 and λ_2 to the corresponding values in a steady 1D laminar flame solution obtained from Cantera as previously demonstrated in [21, 77]. These were later used to determine the individual contributions from increase in length (A'), from the increase in burning rate per unit length of the flame (I_0) and the upstream reactivity (I_{R}) to the overall burning rate as per equations 5.2 and 5.3 respectively. Accordingly, two values of A$'$ (A'_{hot} and A'_{cool}), I_0 ($I_{0,\text{hot}}$ and $I_{0,\text{cool}}$) and I_{R} ($I_{\text{R,hot}}$ and $I_{\text{R,cool}}$) were evaluated. The results of the global analysis are discussed in the subsequent sections.

A transport budget analysis [93] has been performed based on oxygen (O_2) for several steady flame solutions to demonstrate the effect of increasing propagation speed on the evolution of combustion mode. It can be seen in Figure 5.3 that the magnitude of reaction

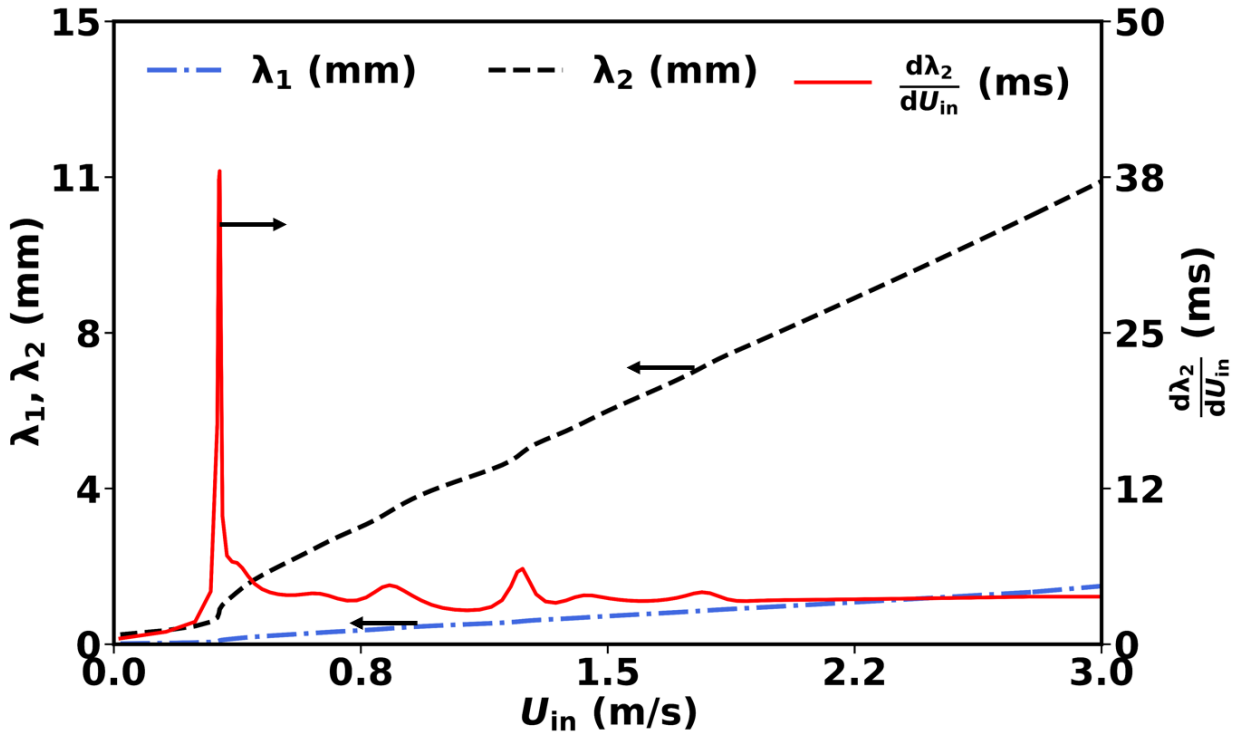

Figure 5.2: (Blue) Position of the cool ignition front away from the inlet, λ_1, vs. inlet velocity, U_{in}. (Black) Position of the hot ignition front away from the inlet, λ_2, vs. inlet velocity, U_{in}. (Red) Derivative of the hot ignition front position with respect to the inlet velocity, $d\lambda_2/dU_{in}$ vs. U_{in}

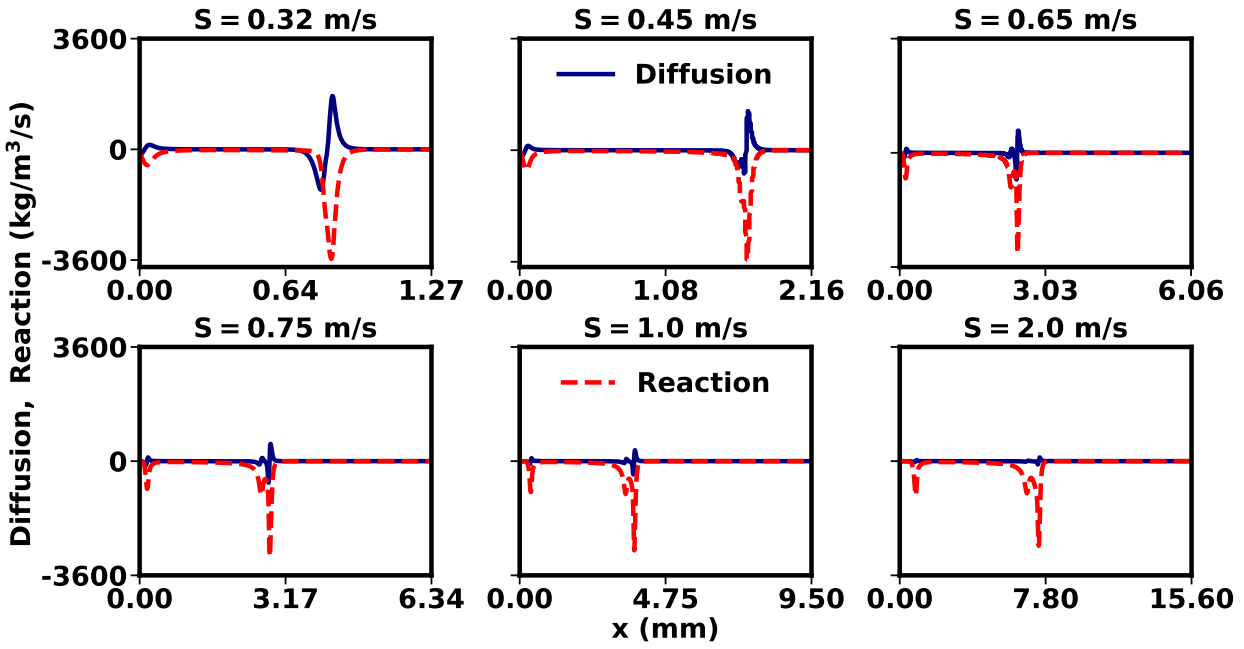

Figure 5.3: Transport budget analysis for steady flames obtained from Cantera [1] propagating at different speeds

and diffusion in the cool as well as the hot reaction front at $S = 0.32$ m/s is of the same order. Hence, in the present study, $S_R = 0.32$ m/s represents the reference laminar flame speed for both the cool as well as the hot reaction front. At the same time, the cool reaction front can be noticed to be attached to the inlet. A clear reduction in diffusion is observed with an increase in S. The cool reaction front appears to be lifted from the inlet only at $S = 1$ m/s. Additionally, the two-stage ignition is found to be transitioning to multi-stage ignition with an increase in S. Although the cool flame at $S = 1$ m/s appears to be lifted, the steady flame solution with $S = 2$ m/s has been used as an initial condition in the present study to avoid interference with the imposed boundary conditions. Moreover, the contribution of diffusion to the overall flame propagation at $S = 1$ m/s as well as $S = 2$ m/s is almost negligible.

The structure of the initial laminar ignition front with $S = 2$ m/s, computed with Cantera [1], is presented in Figure 5.4 in physical space, with heat release rate, $\dot{Q}$ and chemical source terms of representative species, $\dot{\omega}_i$. The following species were selected to study the reaction front structure: 1) oxygen, (O_2), 2) the fuel (CH_3OCH_3), 3) a product of LTC, methoxy-methyl-alcohol (CH_3OCH_2OH), 4) a product of LTC and HTC intermediate, formaldehyde (CH_2O) and 4) a product of HTC, carbon dioxide (CO_2). Several features that are specific to the present mixture conditions can be identified. First, a multi-staged heat release rate can be observed, which is notably different than two-stage heat release typically reported for stoichiometric fuel/air mixtures. The three-staged DME auto-ignition has also been previously reported by Oshibe et al. [46]. Moroever, in a recent study by Sarathy et al. [98], lean n-heptane/air mixtures were also found to exhibit three-stage heat release at high pressures and low-to-intermediate temperatures. Hence, the observed multi-stage ignition is not an artifact of the kinetic model employed herein. In the present study, only the initial and the final ignition stages have been identified for simplicity. Second, a wide range of length scales can be identified. The oxygen consumption and heat release occur over a similar length scale. Likewise, the fuel consumption and formaldehyde production/consumption occur over a comparable length scale. LTC, represented by $\dot{\omega}_{CH_3OCH_2OH}$, is contained to the most upstream portion of the flame and is characterized by a shorter length scale. On the other hand, HTC, represented by $\dot{\omega}_{CO_2}$ is found far downstream and is also characterized by a shorter length scale.

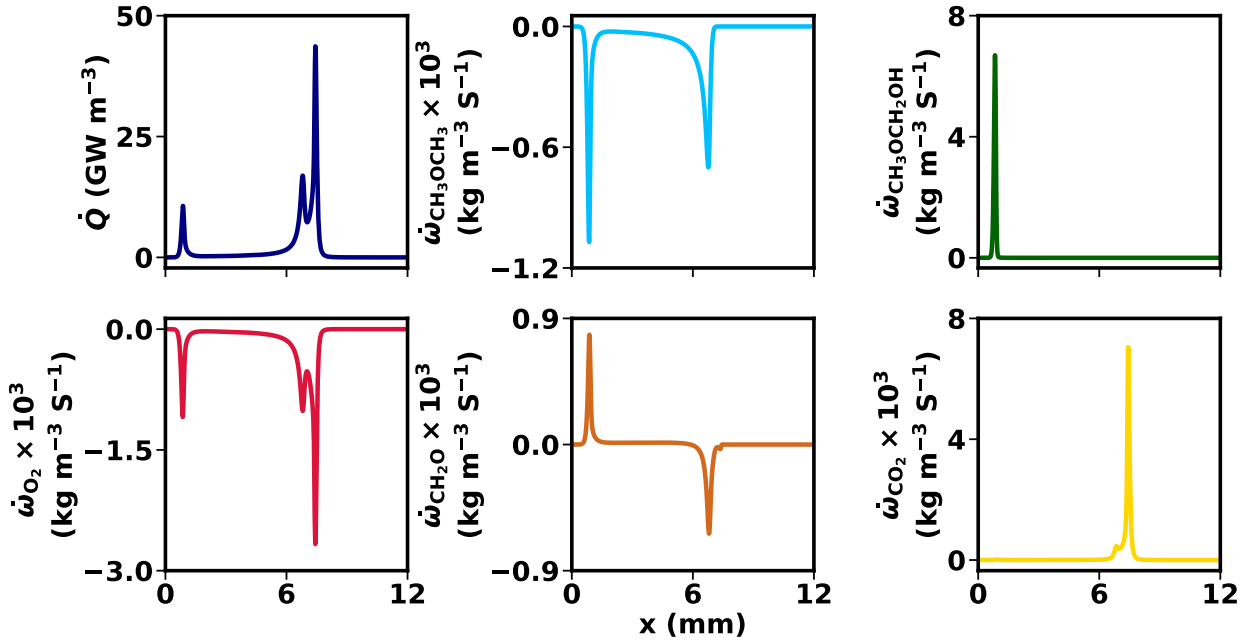

Figure 5.4: Laminar ignition front structure in physical space, showing temperature, heat release rate and species chemical source terms respectively. Note that only a part of the domain is shown to highlight the reaction zone.

5.3 Instantaneous flame structure

In the present study, the cool and the hot ignition fronts have been identified by defining a progress variable, c as: $c = (T - T_u)/(T_b - T_u)$ where, T is the temperature at any point, T_u is the unburned gas temperature and T_b is the burned gas temperature. The value of c corresponding to the maximum heat release rate in the cool and the hot ignition front under laminar conditions was selected as the iso-contour representing the cool and the hot ignition front respectively. At the chosen mean mixture conditions, the respective peaks were observed to occur at $c = 0.05$ and $c = 0.85$.

Figures 5.5, 5.6 and 5.7 depict the instantaneous temperature (T), heat-release rate ($\dot{Q}$), reaction rate of CO_2 ($\dot{\omega}_{CO_2}$, product of HTC) and reaction rate of CH_3OCH_2OH ($\dot{\omega}_{CH_3OCH_2OH}$, product of LTC) in the respective cases. Specifically, the top and bottom sub-figures indicate the quantities at instances of maximum and minimum wrinkling of the hot reaction front (A'_{hot}) respectively. The range of values for the respective quantities is provided in Table 5.2. It is seen that both the cool ignition front as well as the hot ignition front experience turbulence wrinkling. The spatial separation of species representing LTC

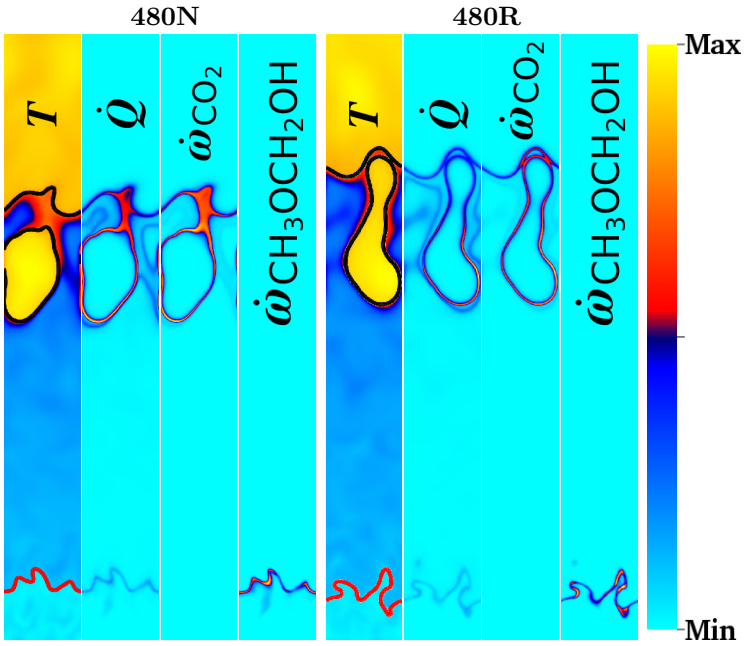

a) Maximum A'_{hot}

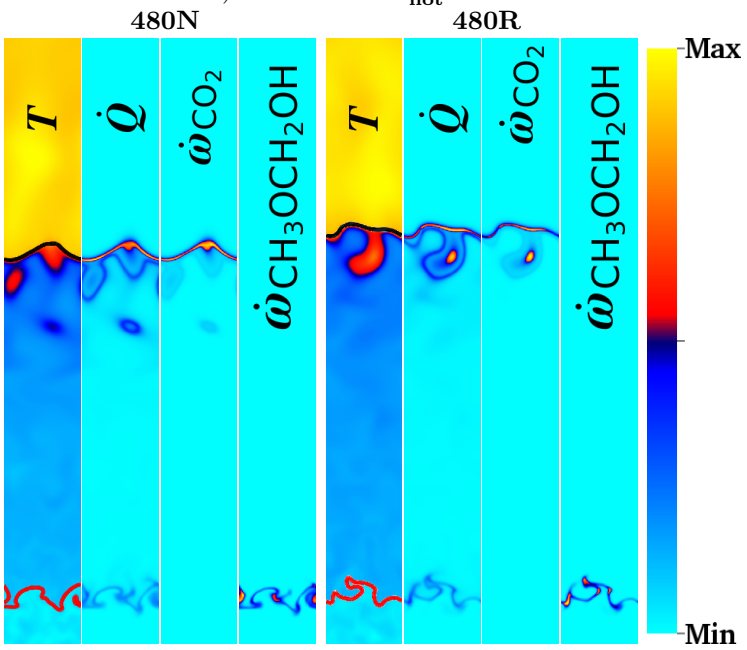

b) Minimum A'_{hot}

Figure 5.5: Instantaneous temperature (T) with iso-contours c = 0.05 (red) and c = 0.85 (black) superimposed, heat release rate ($\dot{Q}$), reaction rate of CO_2 ($\dot{\omega}_{CO_2}$) and reaction rate of CH_3OCH_2OH ($\dot{\omega}_{CH_3OCH_2OH}$) in cases 480N and 480R at instances of a) Maximum A'_{hot}, b) Minimum A'_{hot}. The range of values for the respective quantities is provided in Table 5.2.

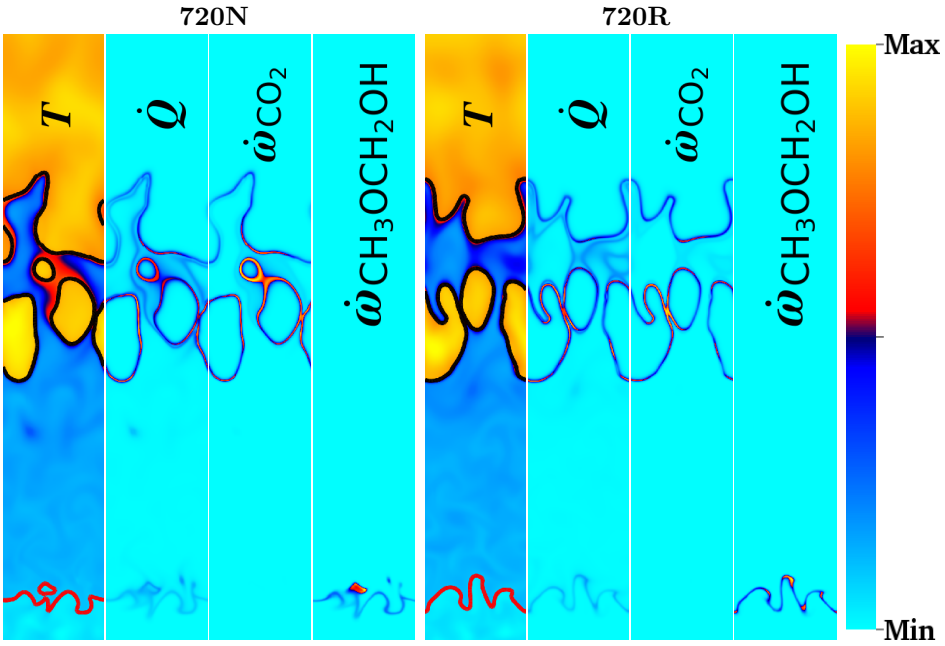

a) Maximum A'_{hot}

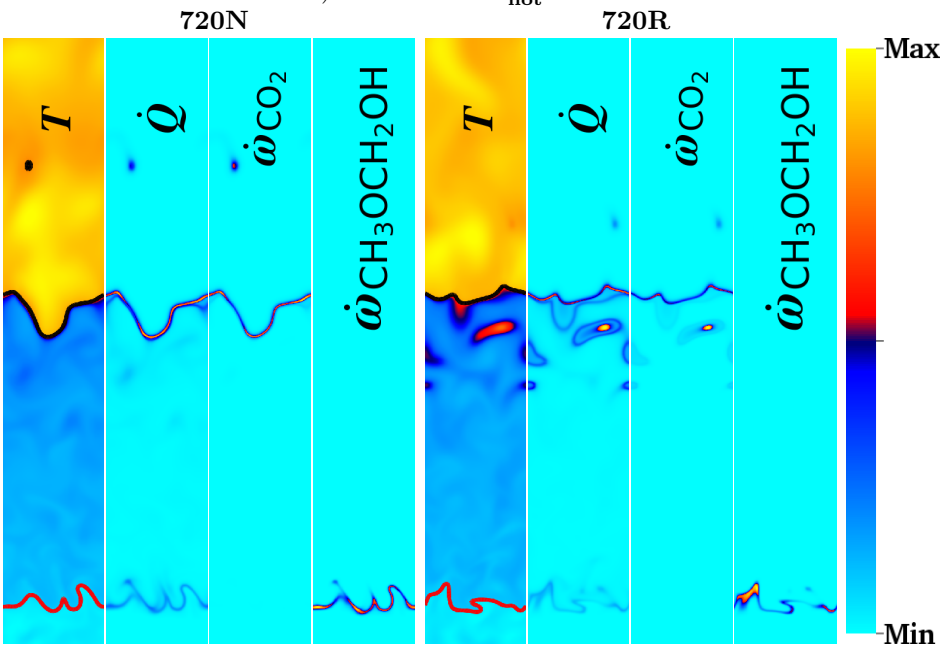

b) Minimum A'_{hot}

Figure 5.6: Instantaneous temperature (T) with iso-contours c = 0.05 (red) and c = 0.85 (black) superimposed, heat release rate ($\dot{Q}$), reaction rate of CO_2 ($\dot{\omega}_{CO_2}$) and reaction rate of CH_3OCH_2OH ($\dot{\omega}_{CH_3OCH_2OH}$) in cases 720N and 720R at instances of a) Maximum A'_{hot}, b) Minimum A'_{hot}. The range of values for the respective quantities is provided in Table 5.2.

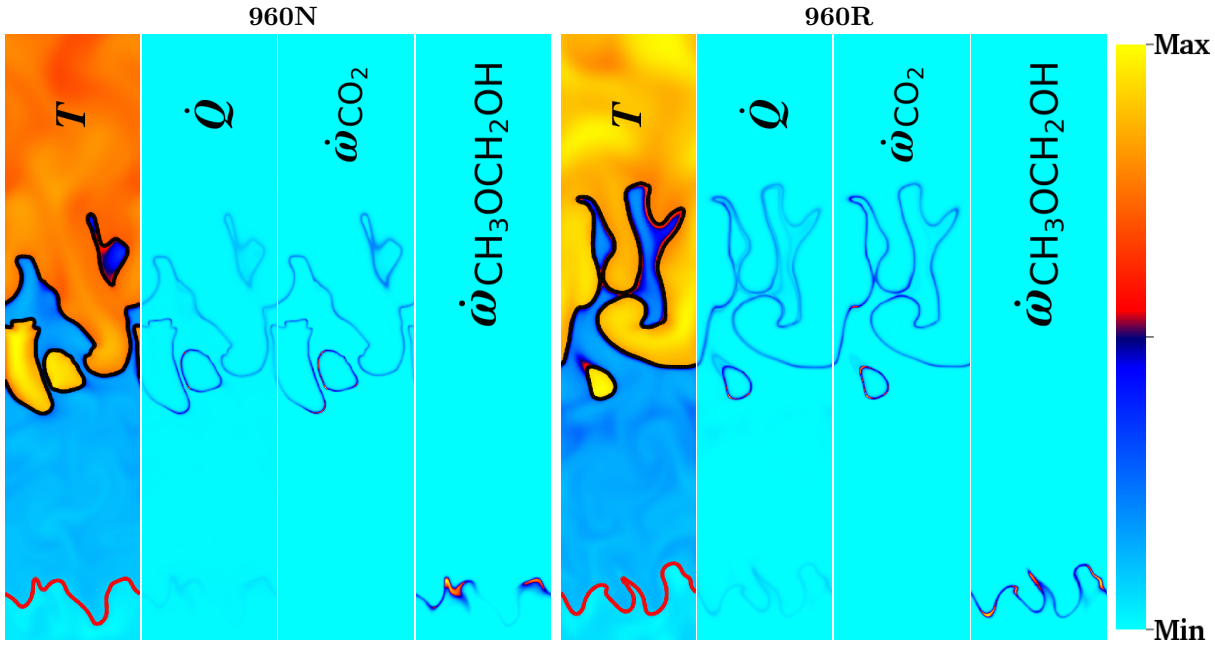

a) Maximum A'_{hot}

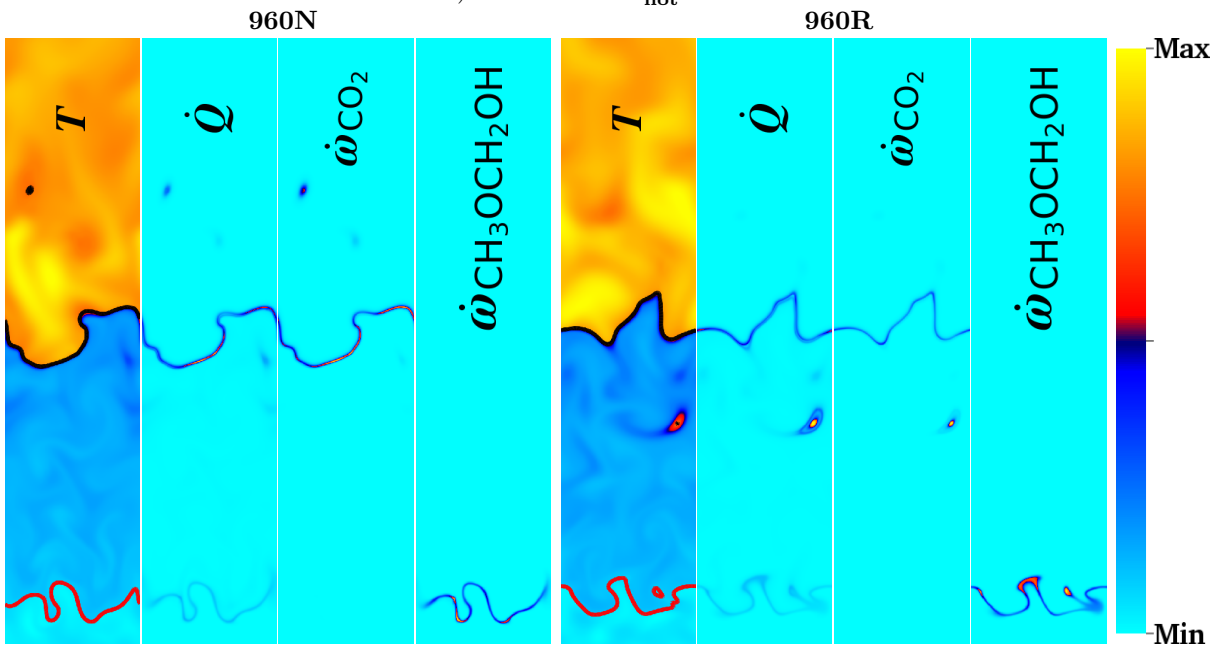

b) Minimum A'_{hot}

Figure 5.7: Instantaneous temperature (T) with iso-contours c = 0.05 (red) and c = 0.85 (black) superimposed, heat release rate ($\dot{Q}$), reaction rate of CO_2 ($\dot{\omega}_{CO_2}$) and reaction rate of CH_3OCH_2OH ($\dot{\omega}_{CH_3OCH_2OH}$) in cases 960N and 960R at instances of a) Maximum A'_{hot}, b) Minimum A'_{hot}. The range of values for the respective quantities is provided in Table 5.2.

Table 5.2: Range ([Min, Max]) of values for the respective quantities shown in Figures 5.5, 5.6 and 5.7.

Maximum A'_{hot}						
Case	**480N**	**480R**	**720N**	**720R**	**960N**	**960R**
T (K)	[768, 1861]	[766, 1843]	[757, 1906]	[755, 1936]	[761, 2102]	[757, 1925]
$\dot{Q}$ (GW m^{-3})	[0, 71.23]	[0, 83.9]	[0, 91.49]	[0, 86.06]	[0, 392.2]	[0, 186.2]
$\dot{\omega}_{CO_2}$ (kg m^{-3} s^{-1})	[0, 9143.2]	[0, 9706.4]	[0, 9908.8]	[0, 9600.8]	[0, 28252.4]	[0, 15642]
$\dot{\omega}_{CH_3OCH_2OH}$ (kg m^{-3} s^{-1})	[0, 15.32]	[0, 8.11]	[0, 19.08]	[0, 12.16]	[0, 16.4]	[0, 10.92]
Minimum A'_{hot}						
Case	**480N**	**480R**	**720N**	**720R**	**960N**	**960R**
T (K)	[771, 1846]	[757, 1822]	[770, 1889]	[770, 1893]	[763, 1989]	[764, 1933]
$\dot{Q}$ (GW m^{-3})	[0, 53.98]	[0, 44.52]	[0, 51.77]	[0, 78.34]	[0, 100.7]	[0, 126.5]
$\dot{\omega}_{CO_2}$ (kg m^{-3} s^{-1})	[0, 7317.2]	[0, 6529.6]	[0, 6384.4]	[0, 12408]	[0, 7673.6]	[0, 18383.2]
$\dot{\omega}_{CH_3OCH_2OH}$ (kg m^{-3} s^{-1})	[0, 13.5]	[0, 11.25]	[0, 8.73]	[0, 10.77]	[0, 11.65]	[0, 13.37]

and HTC as observed in the laminar flames (Figure 5.4) is maintained in the presence of turbulence. At both the chosen time instances, the amount of wrinkling experienced by the cool ignition front (represented by a solid red line overlaid on instantaneous temperature) in cases 480N/480R, 720N/720R and 960N/960R is comparable. No pre-ignition is observed ahead of the cool ignition front in either of the cases. Nonetheless, due to the close proximity of the cool ignition front to the inlet, pinch off is observed to occur in specific cases.

In comparison, at the instance of maximum A'_{hot} (Figures 5.5(a), 5.6(a) and 5.7(a)), single/multiple hot-spots are observed to auto-ignite ahead of the hot reaction front. Consequently, there is a substantial increase in the cumulative wrinkled length of the hot ignition front (represented by a solid black line overlaid on instantaneous temperature). The existing hot reaction front is pushed further downstream due to these auto-igniting hot-spots. Moreover, the different auto-igniting hot-spots give rise to multiple reaction zones that are surrounded by cold-pockets of fuel/air mixture that are yet to burn. These unburned cold-pockets are later consumed when the auto-igniting hot-spots merge with the existing hot reaction front. On the other hand, at the instance of minimum A'_{hot} (Figures 5.5(b), 5.6(b) and 5.7(b)), unlike the cool ignition front, the hot ignition front is noticed to experience only a marginal amount of turbulence wrinkling with a substantially lower cumulative wrinkled length. At the same time, there is an absence of pre-ignition in the upstream mixture in either of the cases. These results indicate that wrinkling and unsteadiness of the hot reaction front is primarily due to pre-ignition in the upstream mixture whereas that of the cool reaction front is mainly due to the imposed turbulence at the inlet.

5.4 Turbulence characteristics

The turbulence scales continue to evolve downstream since no external forcing of the turbulence has been used in the present study. In an unstratified, non-auto-ignitive fuel/air mixture such as the one used in [61], the turbulence intensity (in the absence of external forcing) has been found to quickly decay from the imposed inflow conditions close to the inlet and vary less drastically at further downstream locations. However, under stratified auto-ignitive conditions, intermittent changes in the bulk flow quantities are expected to occur due to the interaction of density fluctuations caused by stratification as well as heat release due to pre-ignition (as shown in figures 5.5, 5.6 and 5.7). To illustrate this, the evolution of the cumulative heat release rate, $\dot{Q}_{\text{total}}$, as well as the mean flow velocity at the domain outlet, V_{outlet} in case 480N over one flow-through time is presented in Figure 5.8 as a representative case. Similar observations were made in the other cases. The time axis is normalized by τ_{f}. It is clearly seen that the temporal phasing as well as increase/attenuation of V_{outlet} coincides with that of $\dot{Q}_{\text{total}}$. This observation suggests that there are large fluctuations in the bulk-flow velocity at locations downstream of the hot reaction front. It is caused by the action of auto-igniting hot-spots and not by the imposed turbulence at the inlet. As a result, the RMS fluctuation of the individual quantities in the present study is evaluated as:

$$\langle f' \rangle_{\text{y,time}} = \sqrt{\langle \langle f^2 \rangle_{\text{y}} - \langle f \rangle_{\text{y}}^2 \rangle_{\text{time}}} \tag{5.4}$$

$\langle f' \rangle_{\text{y,time}}$ in equation 5.4 represents the RMS fluctuation of a given quantity f. The symbol $\langle .... \rangle_{\text{p}}$ in equation 5.4 indicates average of a given quantity over a parameter p (i.e. either y-direction, time or both). Similarly, the mean variance in bulk flow quantities, $\langle f'' \rangle_{\text{y,time}}$, was evaluated separately as:

$$\langle f'' \rangle_{\text{y,time}} = \sqrt{\langle \langle f \rangle_{\text{y}}^2 \rangle_{\text{time}} - \langle f \rangle_{\text{y,time}}^2} \tag{5.5}$$

In the absence of stratification and pre-ignition (as observed in Figure 5.5, 5.6 and 5.7), the values of $\langle u' \rangle_{\text{y,time}}$ and $\langle u'' \rangle_{\text{y,time}}$ as well as $\langle T' \rangle_{\text{y,time}}$ and $\langle T'' \rangle_{\text{y,time}}$ would be equal. However,

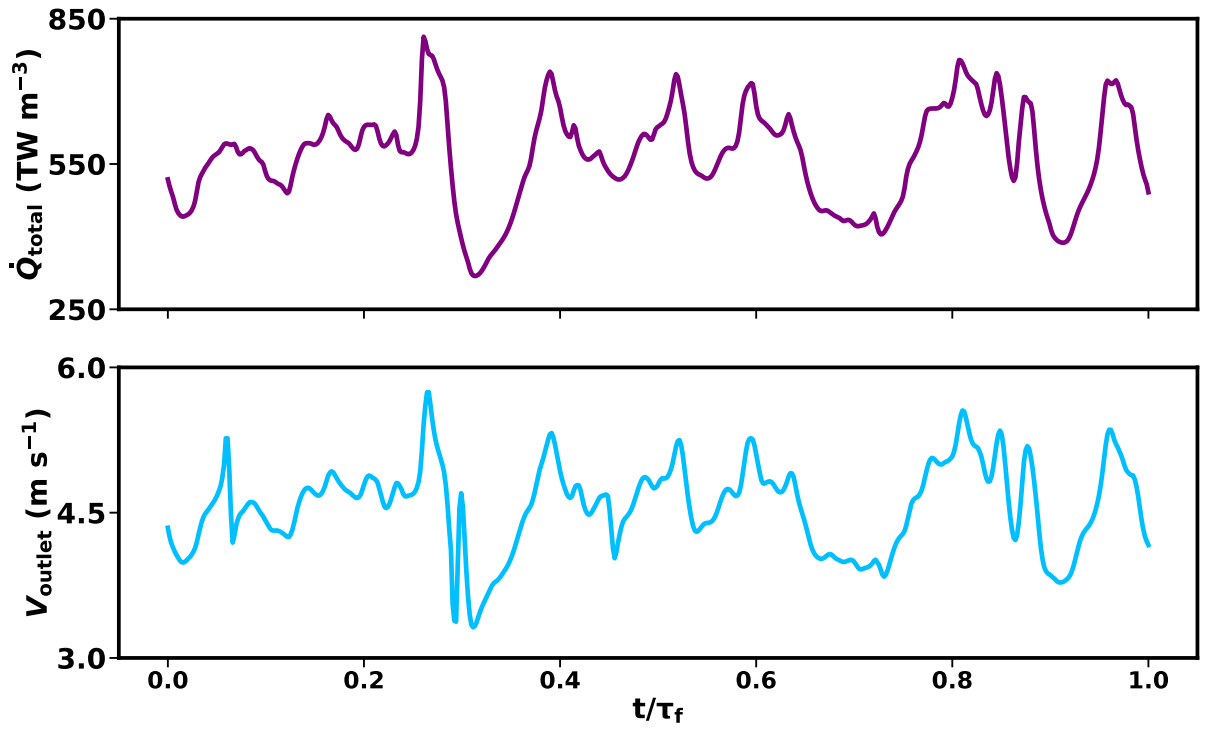

Figure 5.8: Evolution of cumulative heat release rate, $\dot{Q}_{\text{total}}$, and the mean velocity at the domain outlet, V_{outlet} in case 480N over one flow-through time

as shown in Figure 5.9, it is clearly not the case in the present study. u' and T$'$ are evaluated as per equation 5.4 whereas u'' and T$''$ are evaluated as per equation 5.5. For evaluating ϕ' and ϕ'', the equivalence ratio, ϕ, is evaluated at every grid point. This is accomplished by first computing the mixture fraction, ξ as:

$$\xi = \frac{\frac{1}{2}\left(\frac{Z_{\text{H}}-Z_{\text{H,air}}}{M_{\text{H}}}\right) + 2\left(\frac{Z_{\text{C}}-Z_{\text{C,air}}}{M_{\text{C}}}\right) - \left(\frac{Z_{\text{O}}-Z_{\text{O,air}}}{M_{\text{O}}}\right)}{\frac{1}{2}\left(\frac{Z_{\text{H,fuel}}-Z_{\text{H,air}}}{M_{\text{H}}}\right) + 2\left(\frac{Z_{\text{C,fuel}}-Z_{\text{C,air}}}{M_{\text{C}}}\right) - \left(\frac{Z_{\text{O,fuel}}-Z_{\text{O,air}}}{M_{\text{O}}}\right)} \tag{5.6}$$

In equation 5.6, Z_{H}, Z_{C} and Z_{O} are the elemental mass fractions of hydrogen, carbon and oxygen at a given grid point, respectively. Similarly, $Z_{\text{H,fuel}}$, $Z_{\text{C,fuel}}$ and $Z_{\text{O,fuel}}$ are the elemental mass fractions of hydrogen, carbon and oxygen in the fuel whereas $Z_{\text{H,air}}$, $Z_{\text{C,air}}$ and $Z_{\text{O,air}}$ are the elemental mass fractions of hydrogen, carbon and oxygen in air. M_{H}, M_{C} and M_{O} are the atomic weights of hydrogen, carbon and oxygen, respectively. Once ξ is

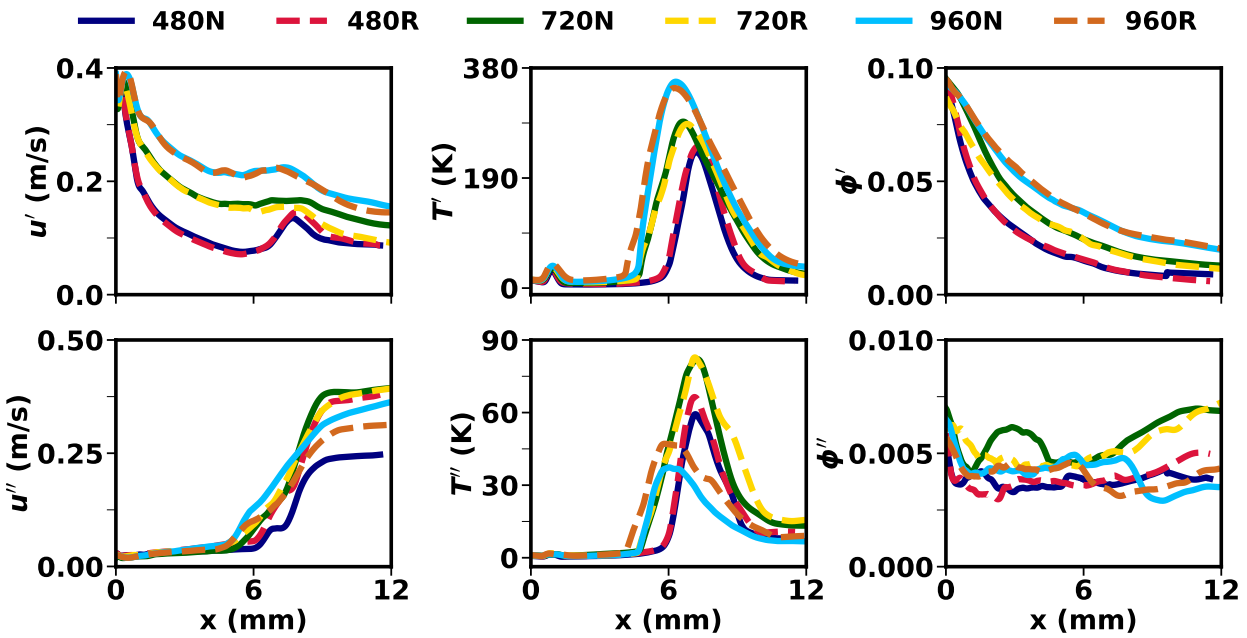

Figure 5.9: Spatial development of velocity fluctuation RMS, u', temperature fluctuation RMS, T′, composition fluctuation RMS, ϕ' and the mean variance in bulk flow quantities, u'', T'' and ϕ'' in the respective cases. Note that only a part of the domain is shown to highlight the reaction zone.

evaluated, the equivalence ratio, ϕ, is then determined as:

$$\phi = \frac{1/\xi_{\text{st}} - 1}{1/\xi - 1}, \text{ where} \tag{5.7}$$

$$\xi_{\text{st}} = \frac{\frac{Z_{\text{O,air}}}{M_{\text{O}}} - \frac{1}{2}\left(\frac{Z_{\text{H,air}}}{M_{\text{H}}}\right) - 2\left(\frac{Z_{\text{C,air}}}{M_{\text{C}}}\right)}{\frac{1}{2}\left(\frac{Z_{\text{H,fuel}} - Z_{\text{H,air}}}{M_{\text{H}}}\right) + 2\left(\frac{Z_{\text{C,fuel}} - Z_{\text{C,air}}}{M_{\text{C}}}\right) - \left(\frac{Z_{\text{O,fuel}} - Z_{\text{O,air}}}{M_{\text{O}}}\right)} \tag{5.8}$$

ξ_{st} in equation 5.7 is the stoichiometric mixture fraction. As depicted in Figure 5.9, at all the imposed turbulence length scales, there is a gradual decay of u' from its imposed value at the inlet. The rate of spatial decay of u' is found to decrease with an increase in the turbulence length scale. However, in each case, a marginal increase in u' can be noticed across the cool as well as the hot reaction front, irrespective of the different turbulence length scales imposed at the inlet. The observed rise in u' is a consequence of flame-generated turbulence which has been demonstrated previously [123, 124]. Similarly, ϕ' decays continuously from its imposed value at the inlet in all the cases. The rate of spatial decay of ϕ' is also observed to decrease with an increase in the turbulence length scale. On the other hand, the spatial

evolution of T' significantly differs from that of u' and ϕ'. In all the cases, an increase in T' is noticed across both the cool and the hot reaction front. Moreover, the increase in T' across the hot reaction front is significantly higher than the imposed value, and its magnitude increases with an increase in the imposed stratification length scale. As discussed in section 5.3, auto-igniting pockets of varying sizes ahead of the hot reaction front lead to multiple reaction zones that are surrounded by cold pockets of fuel/air mixture which are yet to burn. As a consequence, a large deviation in temperature in the vicinity of the hot reaction front is observed. Note that the T-ϕ correlation doesn't seem to have any effect on the spatial evolution of either of the quantities.

With regards to the mean variance in the bulk flow quantities, a significant increase in u'' as well as T'' across the hot reaction front can be noticed. While u'' increases almost to the imposed value of u' (= 0.4 m/s) at the inlet, T'' exceeds the imposed value of T' (= 15 K) at the inlet. As stated earlier, this is primarily caused by the action of auto-igniting pockets and not by the imposed turbulence/stratification at the inlet. On the other hand, ϕ'' is observed to undergo negligible transformation across the cool as well as the hot reaction front. Therefore, neither stratification nor density fluctuations caused by heat release due to pre-ignition affects the mean variance in equivalence ratio. It should be noted that pre-ignition is a stochastic event [111]. Such pre-ignition events drive the evolution of u'', T'' and ϕ''. As such, there is no change in shape in the spatial variation of either u'', T'' or ϕ'' and only a change in magnitude among the different cases.

5.5 Mean flame structure

Figure 5.10 presents the mean heat release rate ($\dot{Q}$), the reaction rates of key species as well as temperature (T) conditioned on the horizontal spatial location (x). Note that these results have been obtained by performing averaging in y-direction as well as time. Compared to the initial laminar profiles, the respective peaks of $\dot{Q}$ and the reaction rates of key species are drastically reduced under stratified conditions. The imposed stratification/turbulence length scales predominantly affect the profiles of the mean turbulent cool as well as hot reaction fronts. On the other hand, the imposed T-ϕ correlation seems to have only a marginal

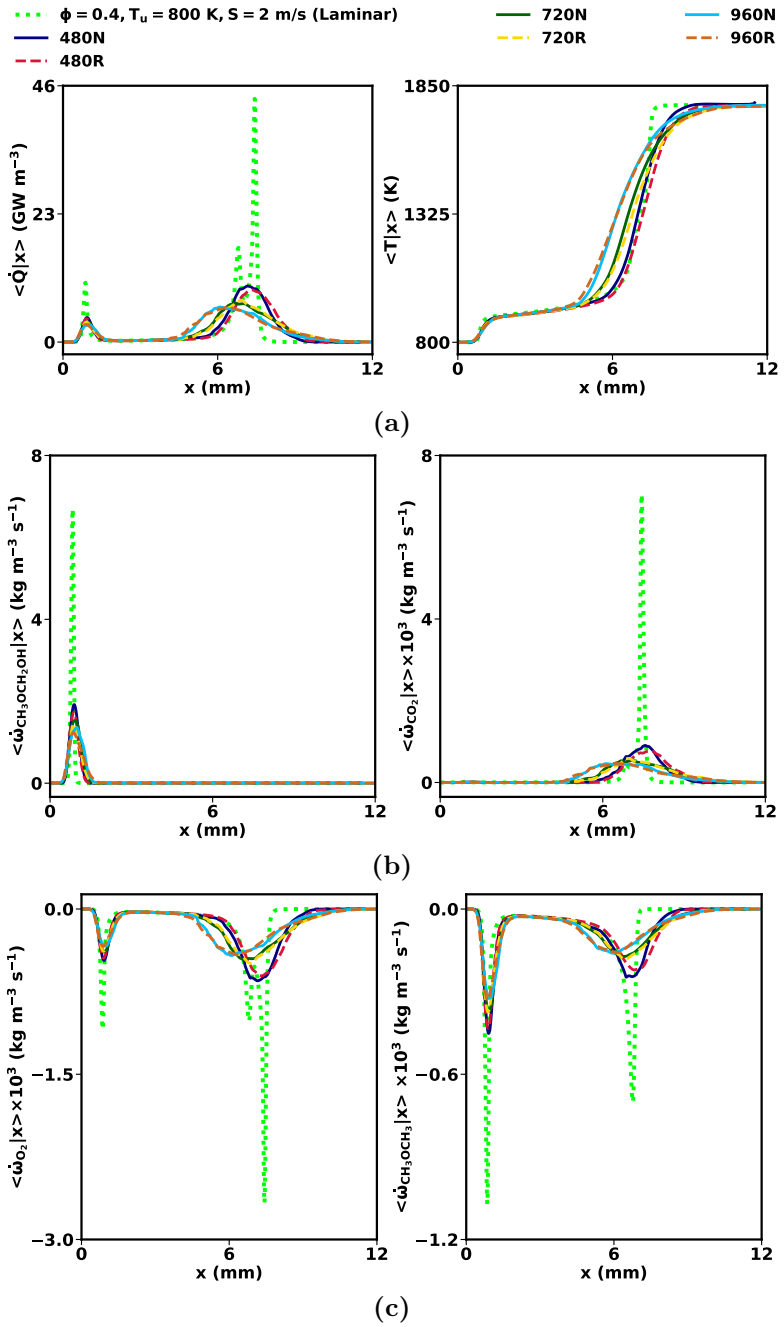

Figure 5.10: Mean a) heat release rate and temperature, b) reaction rates of CH_3OCH_2OH and CO_2 and c) reaction rates of O_2 and CH_3OCH_3 conditional on the horizontal spatial location (x) compared to the initial laminar profiles. Results of cases with negatively correlated T-ϕ are shown by solid lines, those of uncorrelated T-ϕ are shown by dashed lines and the respective initial laminar profiles are shown by a dotted line. Note that only a part of the domain is shown to highlight the reaction zone.

effect on their respective mean profiles. Larger stratification length scales weaken the low temperature chemistry as observed from the reduction as well as a minor shift in the peak magnitude of $\dot{\omega}_{CH_3OCH_2OH}$ away from the inlet. At the same time, the high temperature chemistry is found to be enhanced by larger stratification length scales as evidenced by wider $\dot{Q}$, $\dot{\omega}_{CO_2}$ and T profiles that can be noticed to approach the outflow. In addition, the location of peak $\dot{Q}$ can also be noticed to be shifted upstream closer to the inlet, thereby indicating a reduction in the contribution of upstream reactivity to the overall burning rate as well as transition of propagation mode of the hot reaction front, from ignition-controlled to deflagration.

Figure 5.11 presents the mean heat release rate ($\dot{Q}$) as well as the reaction rates of key species conditioned on temperature. Note that these results have been obtained by performing averaging only in time. First, it is seen that with an increase in stratification/turbulence length scales, the profiles of $\dot{Q}$, $\dot{\omega}_{O_2}$, $\dot{\omega}_{CO_2}$ and $\dot{\omega}_{CH_3OCH_2OH}$ are lowered in magnitude, narrowed in temperature space, and their corresponding peaks are shifted to lower temperatures. Similar trend is observed in the first peak of $\dot{\omega}_{CH_3O_CH_3}$ and $\dot{\omega}_{CH_2O}$ profiles. However, the second peak of $\dot{\omega}_{CH_3O_CH_3}$ and $\dot{\omega}_{CH_2O}$ profiles appears to have broadened in temperature space with increased peak magnitude and a longer tail towards higher temperature. Second, the profiles in each case are found to be different from the initial laminar profiles. At the shortest stratification/turbulence length scale (cases 480N/480R), it is seen that the profiles closely match the laminar profile of a reaction front propagating at a much lower speed $S = 0.7$ m/s under identical unburned mixture conditions. Based on $S_T = 2$ m/s, the turbulent cool as well as the hot reaction front was a priori expected to be controlled by ignition in each case. But, the profiles of $\dot{\omega}_{CH_3OCH_2OH}$ (product of LTC) and $\dot{\omega}_{CO_2}$ (product of HTC) are seen to resemble more to that of a self-propagating flame. This is consistent with the observations in a recent study by Savard et al. [80] wherein the reaction zone structure of steady-state turbulent flames was found to approach that of self-propagating laminar flames which was significantly different than the initial ignition fronts. As the stratification/turbulence length scales are increased, unlike $\dot{\omega}_{CH_3OCH_2OH}$, the profiles of $\dot{\omega}_{CO_2}$ further shift towards that of a laminar flame propagating even slower at $S = 0.4$ m/s under identical unburned mixture temperature but leaner conditions. This observation

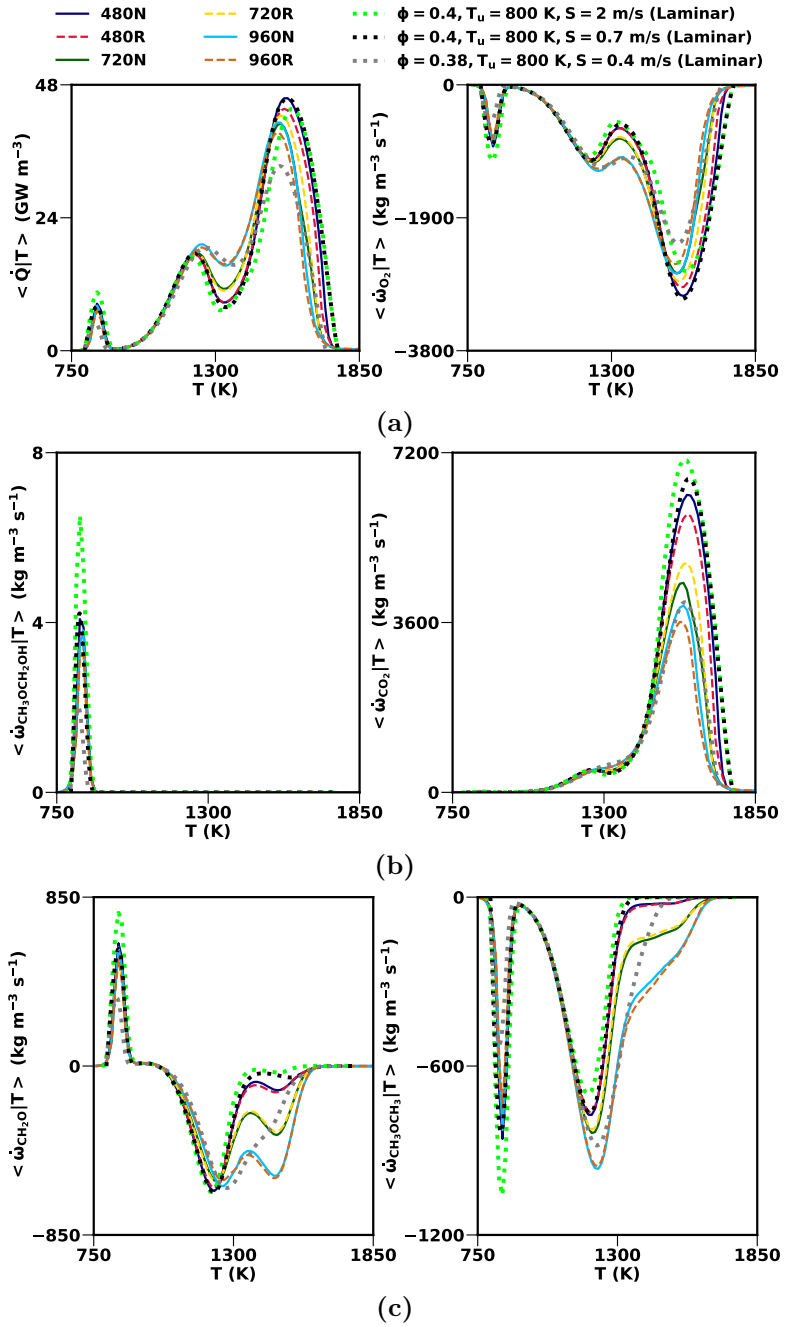

Figure 5.11: Mean a) heat release rate and reaction rate of O_2, b) reaction rate of CH_3OCH_2OH and CO_2 and c) reaction rate of CH_3OCH_3 and CH_2O conditional on temperature compared to the laminar cases at different mean unburned mixture conditions. Results of cases with negatively correlated T-ϕ are shown by solid lines, those of uncorrelated T-ϕ are shown by dashed lines and the respective laminar profiles are shown by a dotted line.

indicates that between the mean turbulent cool and the hot reaction front, the latter is more deflagrative in nature. Finally, at a given stratification/turbulence length scale, the effect of T-ϕ correlation on the flame structure is found to be marginal.

The transition in combustion mode from ignition controlled to deflagration in each case is also studied using a transport budget analysis [93] based on oxygen (O_2) and is presented in Figure 5.12. Compared to the initial ignition front with $S = 2$ m/s, there is a substantial increase in the contribution of diffusion to the propagation of the hot reaction front. The contribution of diffusion to hot front propagation is found to increase with an increase in stratification length scale. At the same time, there is a reduction in the contribution of reaction to the hot front propagation with an increase in stratification length scale. There is comparatively less change in the contribution of either diffusion or reaction to the cool front propagation with an increase in stratification length scale. As before, the diffusion-reaction profiles at smaller stratification length scales match reasonably well with that of a laminar reaction front propagating at a much lower speed $S = 0.7$ m/s under identical unburned mixture conditions. Whereas at larger stratification length scales, the diffusion-reaction

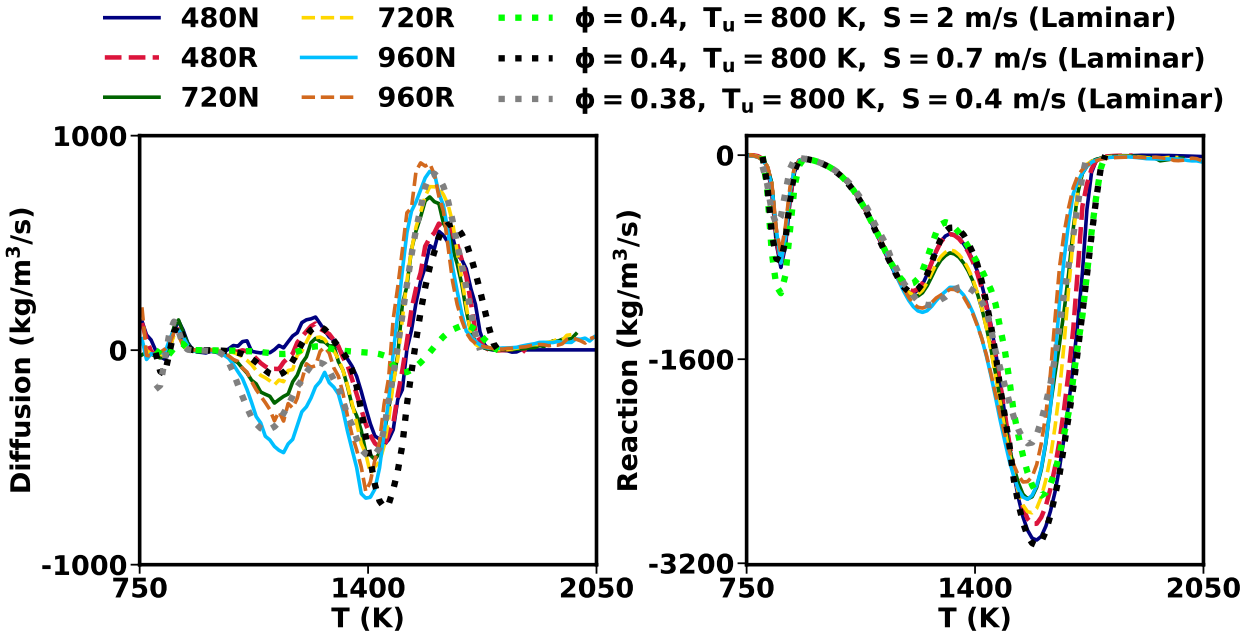

Figure 5.12: Mean diffusion and reaction terms conditional on temperature compared to the laminar cases at different mean unburned mixture conditions. Results of cases with negatively correlated T-ϕ are shown by solid lines, those of uncorrelated T-ϕ are shown by dashed lines and the respective laminar profiles are shown by a dotted line.

profiles shift toward that of a laminar flame propagating even slower at $S = 0.4$ m/s under identical unburned mixture temperature but leaner conditions.

5.6 Global burning velocity

The individual contributions from the increase in length (A'), the increase in burning rate per unit length of the flame (I_0) as well as the upstream reactivity (I_R) to the overall burning rate of the cool as well as the hot ignition front (determined as per equations 5.2 and 5.3) is presented here. In each case, the mean turbulent flame speed, $S_T = 2$ m/s. As discussed earlier, the iso-surface $c = 0.05$ represents the mean turbulent cool reaction front while the iso-surface $c = 0.85$ represents the mean hot reaction front. The two different one-dimensional propagation speeds, $S_{1D,cool}$ and $S_{1D,hot}$ are determined by relating the locations of peak $\dot{Q}$ in the mean turbulent cool (i.e. $\lambda_{1,mean}$) and hot reaction front (i.e. $\lambda_{2,mean}$), denoted by cross marks in Figure 5.13, to the corresponding values in a steady 1D laminar flame solution obtained from Cantera as shown in Figure 5.2. Note that averaging is performed in both y-direction and time for obtaining $\lambda_{1,mean}$ and $\lambda_{2,mean}$. From the values provided in Table 5.3, it is found that stratification/turbulence length scales are increased, $\lambda_{2,mean}$ decreases in magnitude (i.e. the hot reaction front shifts towards the inlet), which results in a decrease in the magnitude of $S_{1D,hot}$ and consequently $I_{R,hot}$. As a result, the contribution of upstream reactivity to the overall burning rate of the hot reaction front gradually diminishes with an increase in the stratification/turbulence length scale. This observation provides further quantitative evidence of the transition of propagation mode of the hot reaction front from ignition-controlled to deflagration. On the other hand, $\lambda_{1,mean}$ increases marginally (i.e. the cool reaction front shifts away from the inlet), which causes a small rise in the magnitude of $S_{1D,cool}$ and consequently $I_{R,cool}$.

Similarly, time-averaged results of A'_{cool} and A'_{hot} are listed in Table. 5.3. While A'_{hot} is noticed to progressively increase, A'_{cool} is found to remain fairly constant. Consequently, there is a decrease in $I_{0,hot}$ whereas there is no significant change in $I_{0,cool}$. As before, the T-ϕ correlation in the respective cases doesn't seem to significantly affect either the amount of wrinkling or the burning rate per unit length.

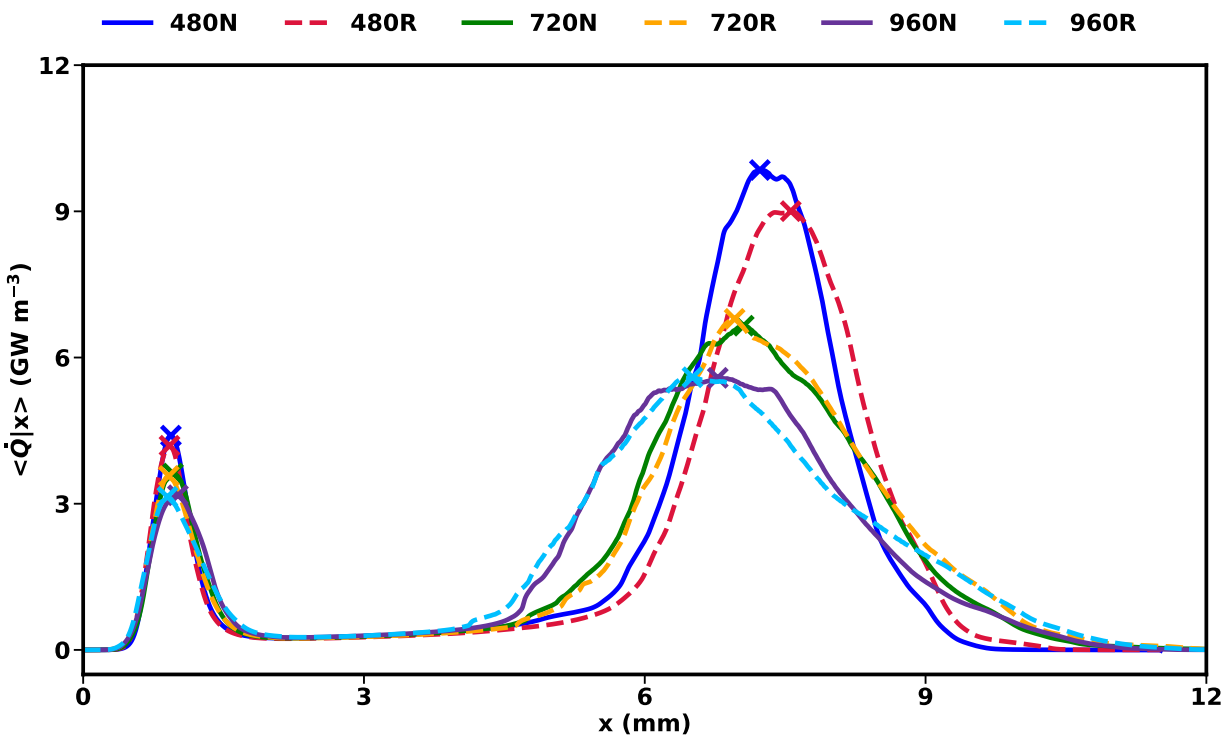

Figure 5.13: Mean heat release rate conditional on the horizontal spatial location. Cross marks indicate the spatial location of peak heat release rate in the respective cases.

Table 5.3: Individual contributions of A′, I_0 and I_R to S_T in the respective cases

Case	$\lambda_{1,\mathrm{mean}}$ (mm)	$\lambda_{2,\mathrm{mean}}$ (mm)	$S_{1D,\mathrm{cool}}$ (m/s)	$S_{1D,\mathrm{hot}}$ (m/s)	A'_{cool}	A'_{hot}	$I_{R,\mathrm{cool}}$	$I_{R,\mathrm{hot}}$	$I_{0,\mathrm{cool}}$	$I_{0,\mathrm{hot}}$
480N	0.94	7.23	2.08	1.94	1.79	2.71	6.50	6.06	0.54	0.38
480R	0.92	7.56	2.05	2.03	1.98	2.98	6.41	6.34	0.49	0.33
720N	0.96	7.06	2.14	1.89	1.80	3.86	6.69	5.91	0.52	0.27
720R	0.92	6.96	2.03	1.86	2.04	3.78	6.34	5.81	0.48	0.28
960N	1.01	6.78	2.26	1.81	1.71	4.42	7.06	5.66	0.52	0.25
960R	0.90	6.51	2.02	1.75	1.87	4.85	6.31	5.47	0.53	0.24

5.7 Displacement speed

In this subsection, the nature of propagation of the steady-state turbulent cool as well as the hot reaction front is examined. Specifically, statistics of density weighted displacement speed of the cool reaction front, $S_{\mathrm{d,cool}}$, and the hot reaction front, $S_{\mathrm{d,hot}}$, in the respective cases are analyzed. The displacement speed, S_{d}, is defined by the movement of a scalar iso-contour that corresponds to the reaction front. For a given iso-contour of a species, the density weighted displacement speed [96] is defined as:

$$S_{\mathrm{d}} = \frac{1}{\rho_{\mathrm{u}}|\nabla Y_{\mathrm{k}}|}(-\dot{\omega}_{\mathrm{k}} - \nabla \cdot (\rho D Y_{\mathrm{k}})) \tag{5.9}$$

where ρ_u is the density of the unburned mixture, $\dot{\omega}_k$ is the reaction rate of species k, Y_k is the mass fraction of species k and D is the species diffusivity. In the present study, oxygen (O_2) is used as the representative species for evaluating both $S_{\mathrm{d,cool}}$ and $S_{\mathrm{d,hot}}$.

A probability distribution function (PDF) of $S_{\mathrm{d,cool}}$ conditioned at the iso-contour representing the cool reaction front (c = 0.05) and $S_{\mathrm{d,hot}}$ conditioned at the iso-contour representing the hot reaction front (c = 0.85) in the respective cases is shown in Figure 5.14. It is seen that, in all the cases, the distribution of neither $S_{\mathrm{d,cool}}$ nor $S_{\mathrm{d,hot}}$ is symmetrical around the initial mean displacement speed of 2 m/s. The $S_{\mathrm{d,cool}}$ distribution is broader and has a longer tail towards higher values than the $S_{\mathrm{d,hot}}$ distribution. This shows that cool

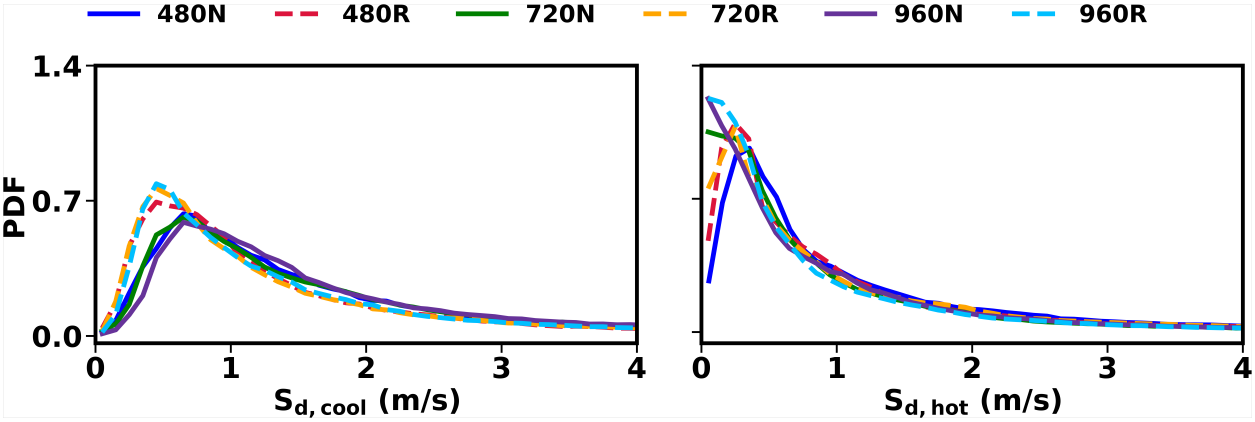

Figure 5.14: Distribution of displacement speeds, $S_{\mathrm{d,cool}}$ and $S_{\mathrm{d,hot}}$, conditioned at the iso-contours representing the cool reaction front (i.e. c = 0.05) and the hot reaction front (i.e. c = 0.85)

reaction fronts with higher displacement speeds are more likely than hot reaction fronts with higher propagation speeds. This is also reflected from the time-averaged values of $S_{d,cool}$ and $S_{d,hot}$ listed in Table 5.4. It also confirms the observations made in section 5.5 that the hot reaction front is more deflagrative in nature than the cool reaction front, especially in cases with larger turbulence/stratification length scales. From the $S_{d,cool}$ distribution in the respective cases, it is found that the likelihood of encountering slower cool reaction fronts in the cases with uncorrelated T-ϕ is higher than that in the cases with negatively related T-ϕ. On the other hand, from the $S_{d,hot}$ distribution in the respective cases, it can be noticed that the probability of encountering progressively slower hot reaction fronts increases with an increase in the turbulence/stratification length scale, irrespective of the T-ϕ correlation. Results depicted in Table 5.4 also support this observation.

5.8 Concluding remarks

A 2D statistically stationary turbulent premixed flame propagating in a stratified DME/air mixture exhibiting multi-staged ignition was simulated. Results obtained using different stratification/turbulent length scales and T-ϕ correlation showed that unlike the latter, the former parameter predominantly affects the turbulent flame dynamics. At shorter length scales, the mean flame structure in temperature space was found to approach that of the self-propagating laminar flames under identical unburned mixture conditions. At larger length scales, however, the mean flame structure was seen to approach that of the self-propagating laminar flames at identical unburned temperature but leaner equivalence ratio conditions.

Table 5.4: Mean $S_{d,cool}$ and $S_{d,hot}$ in the respective cases

Case	Mean $S_{d,cool}$ (m/s)	Mean $S_{d,hot}$ (m/s)
480N	1.76	1.34
480R	1.53	1.22
720N	1.80	1.05
720R	1.55	1.23
960N	1.89	1.06
960R	1.59	0.99

A global analysis of the flame burning velocity indicated that the mean turbulent hot reaction front shifts towards the inlet with an increase in the stratification/turbulence length scale. Consequently, there was a decrease in the contribution of upstream reactivity to the overall burning rate of the hot reaction front. Meanwhile, the variation in the position of the mean turbulent cool reaction with respect to the imposed length scales was found to be marginal. As such, no significant change was observed in the contribution of upstream reactivity to the overall burning rate of the cool reaction front. Additionally, the hot ignition front was found to undergo considerably higher amount of wrinkling than the cool ignition front, primarily due to pre-ignition in the upstream mixture. As a result, there was a marginal decrease in the burning efficiency factor of the hot reaction front whereas there was no noticeable change in the burning efficiency factor of the cool reaction front.

Displacement speed statistics showed that, in each case, the mean turbulent hot reaction front is more deflagrative in nature than the mean cool reaction front. The displacement speed distribution for the cool reaction front showed that the likelihood of encountering slower cool reaction fronts in the cases with uncorrelated T-ϕ is higher than that in the cases with negatively related T-ϕ. At the same time, the displacement speed distribution for the hot reaction front indicated that the probability of encountering progressively slower hot reaction fronts increases with an increase in the turbulence/stratification length scale, irrespective of the T-ϕ correlation.

Chapter 6

Conclusions and future work

6.1 Conclusions

This dissertation focused on the systematic investigation of the controlling mechanisms affecting propagation speeds of flame fronts relevant to modern combustion strategies employed in advanced gas turbines and IC engines. Unlike the periodic box setup that has been used in majority of the previous DNS studies, a statistically stationary reaction front using an inflow-outflow configuration was employed to understand the unsteady flame dynamics at auto-ignitive conditions. To the best of author's knowledge, it was demonstrated for the first time that the combustion behavior under modern IC engine conditions may exhibit intricate interplay between deflagration, auto-ignition, and spontaneous propagation modes, and the level of complexity depends on the length/time scales of fluctuations in temperature and composition within the reactant mixture, which affects the time scales of the flame-ignition interaction. In addition, the implementation methodology, effectiveness and fine-tuning of shock-capturing schemes such as the Weighted Essentially Non-Oscillatory (WENO) schemes in performing DNS of turbulent reacting flows was also demonstrated with various model problems. The major findings of this research are listed below:

- **Chapter 2:** It was demonstrated that, under auto-ignitive conditions, the propagation speed of a steady flame front scales proportionally to the level of upstream reactivity, in the presence as well as absence of low-temperature chemistry. As the characteristic

residence time approaches the auto-ignition time scale, the deflagration front transitions to a spontaneous combustion regime with higher speeds. It was also shown that the rise in propagation speed is faster for fuel/air mixtures with a smaller ignition delay. Moreover, a parametric mapping of front propagation speeds in the presence of monochromatic thermal inhomogeneities imposed at the inlet was presented. The displacement speed analysis together with the temporal evolution of temperature provided evidence of cyclical transition of the combustion mode from deflagration to spontaneous propagation. There was significant variation in instantaneous propagation speed of flame front under the influence of imposed thermal stratification, especially at the time scales corresponding to the homogeneous ignition delay times. Analysis of reaction rates of key radical species indicated that unlike low-temperature chemistry, high-temperature chemistry was mainly responsible for the observed variation in propagation speeds.

- **Chapter 3:** Results obtained above provided a platform for the subsequent investigations. Consequently, a parametric mapping of propagation speeds of a dual-fuel (DME + CH_4) flame front under the influence of monochromatic inhomogeneities in DME concentration and varying blending ratios in a binary fuel blend was provided. The flame front responded to all the imposed stratification time scales except the smallest, which was contrary to that observed under thermal stratification. Increasing the blending ratio suppressed the dynamic response of a reaction front involving low-temperature chemistry at smaller time scales. Addition of CH_4 made the binary fuel blend more resistant to auto-ignition. This led to the high-temperature chemistry remaining mostly unaffected. At larger time scales, however, increasing the level of CH_4 concentration in the binary fuel blend caused a noticeable increase in the dynamic response of a reaction front, irrespective of the presence/absence of low-temperature chemistry. It was shown that this behavior was mainly due to a more responsive high-temperature chemistry. Low-temperature chemistry, on the other hand, had a similar dynamic response at smaller time scales, irrespective of the level of CH_4 concentration

in the binary fuel blend. At larger time scales, however, it became increasingly non-responsive as the level of CH_4 concentration in the binary fuel blend was increased. The displacement speed analysis together with the temporal evolution of temperature provided evidence of cyclical transition of the combustion mode from deflagration to spontaneous propagation. The induction time available for the upstream mixture to pre-ignite increased with an increase in the CH_4 concentration in the binary fuel blend. As such, multiple reaction fronts developed ahead of the main flame front, irrespective of either the amplitude or the time scale of stratification. These reaction fronts propagated at much higher speeds than the main flame front itself and predominantly lead to a substantial rise in the overall propagation speed.

- **Chapter 4:** 1-D investigations in chapters 2 and 3 demonstrated the existence of sharp spatial variation in temperature and density, resulting due to premature ignition, embedded within relatively smooth regions. These phenomena might have rendered the standard eighth-order finite central difference operator used in KARFS either cost prohibitive due to extremely fine grid size requirement or ineffective in capturing the underlying physics altogether when performing multi-dimensional simulations. As such, the dire need of implementing of shock capturing schemes such as Weighted Essentially Non-oscillatory (WENO) schemes in KARFS was highlighted. To that end, the implementation methodology of several high-order WENO schemes into KARFS on multiple GPU architectures was presented. A thorough validation of the implemented WENO schemes was presented with model problems involving shocks, isotropic turbulence, detonations and flame propagation into a stratified mixture with complex chemical kinetics. In addition, a detailed performance assessment of KARFS was also reported to provide estimates that can be used for an appropriate load-balanced decomposition of future production simulations.

- **Chapter 5:** As a more comprehensive study, direct numerical simulations of a turbulent premixed flame in an auto-ignitive fuel/air mixture were carried out. Different stratification/turbulence length scales and correlations between temperature (T) and equivalence ratio (ϕ) fields with an identical turbulence intensity were

simulated to study the dynamics of turbulent premixed flame propagation at auto-ignitive conditions. Results obtained using different stratification/turbulent length scales and T-ϕ correlation showed that unlike the latter, the former parameter predominantly affects the turbulent flame dynamics. At shorter length scales, the mean flame structure in temperature space approached that of the self-propagating laminar flames under identical unburned mixture conditions. At larger length scales, however, the mean flame structure approached that of the of the self-propagating laminar flames at identical unburned temperature but leaner conditions. A global analysis of the flame burning velocity indicated that the mean turbulent hot reaction front shifts towards the inlet with an increase in the stratification/turbulence length scale. Consequently, there was a decrease in the contribution of upstream reactivity to the overall burning rate of the hot reaction front. Meanwhile, the variation in the position of the mean turbulent cool reaction with respect to the imposed length scales was marginal. As such, there was no significant change in the contribution of upstream reactivity to the overall burning rate of the cool reaction front. Additionally, the hot ignition front underwent considerably higher amount of wrinkling than the cool ignition front, primarily due to pre-ignition in the upstream mixture. As a result, there was a marginal decrease in the burning efficiency factor of the hot reaction front whereas there was no noticeable change in the burning efficiency factor of the cool reaction front. Displacement speed statistics showed that the mean turbulent hot reaction front is more deflagrative in nature than the mean cool reaction front. The displacement speed distribution for the cool reaction front showed that the likelihood of encountering slower cool reaction fronts in the cases with uncorrelated T-ϕ is higher than that in the cases with negatively related T-ϕ. At the same time, the displacement speed distribution for the hot reaction front indicated that the probability of encountering progressively slower hot reaction fronts increases with an increase in the turbulence/stratification length scale, irrespective of the T-ϕ correlation.

6.2 Directions for future work

With regards to the parametric mapping of propagation speeds at auto-ignitive conditions (chapters 2 and 3), there is scope to improve upon and extend the findings of the present work. As of now, propagation speeds of a relatively simple fuel such as dimethyl-ether and its blend with methane at auto-ignitve conditions have been investigated and used to compare the influence flame thermal structure (i.e. single- vis-*á*-vis multi-stage ignition) on the evolving flame dynamics. A similar study with complex hydrocarbon fuels and bio-fuels for both negative temperature coefficient (NTC) and non-NTC conditions would be highly insightful. It will be especially interesting to compare the propagation speeds of fuels exhibiting NTC behavior and multi-stage ignition (e.g. n-heptane) to the ones without (e.g. iso-octane). Since, dimethyl-ether and ethanol have the same chemical formula but different molecular structure, it would be particularly interesting to investigate the propagation speeds of dimethyl-ether/ethanol/air mixtures using the recently developed mechanism [125]. It would help unravel the effects of fuel molecular structure on the unsteady flame dynamics. Secondly, right now, we have conducted DNS studies with 2D turbulence without any vortex stretching and tilting. However, turbulence is inherently a 3D phenomenon. Therefore, computational studies for realistic 3D turbulent reacting flows will provide better insights into flame dynamics at auto-ignitive conditions. Third, in the statistically stationary planar configuration used here, the injected velocity fluctuation RMS (i.e. u') must be less than the mean inlet flow velocity and consequently the mean propagation speed. An alternative choice could be using a V-flame configuration [126] wherein the flame stabilization is mimicked by an ad hoc device. This configuration would potentially allow the use of large inlet velocities and turbulence intensities. It will be intriguing to compare the current results with those obtained using the V-flame configuration. One could also compare the obtained results with unsteady 1D results performed with one dimensional turbulence model (ODT) [127]. Finally, it is important to capture the radical buildup late in the compression stroke (i.e., near TDC) because there is a significant radical buildup during the compression stroke due to the low-temperature chemistry effects of hydrocarbon fuels. As such, the effect of compression heating (caused by piston motion as well as flame propagation) on the evolution

of propagation speeds could be investigated using the methodology presented in chapter 4, section 4.2.4.

Bibliography

[1] D. G. Goodwin, H. K. Moffat, and R. L. Speth. Cantera: An object-oriented software toolkit for chemical kinetics, thermodynamics, and transport processes. *Version 2.4.0*, 2018. (www.cantera.org). xvi, 26, 27, 44, 46, 52, 82, 104, 107, 108, 109, 150

[2] U.S. Energy Information Administration. Annual energy outlook 2018 with projections to 2050. 2018. (https://www.eia.gov/outlooks/aeo/pdf/AEO2018.pdf). 1

[3] R. D. Reitz. Directions in internal combustion engine research. *Combustion and Flame*, 1(160):1–8, 2013. 1

[4] S. L. Kokjohn, R. M. Hanson, D. A. Splitter, and R. D. Reitz. Fuel reactivity controlled compression ignition (RCCI): a pathway to controlled high-efficiency clean combustion. *International Journal of Engine Research*, 12(3):209–226, 2011. 2

[5] C. Strozzi, A. Mura, J. Sotton, and M. Bellenoue. Experimental analysis of propagation regimes during the autoignition of a fully premixed methane−air mixture in the presence of temperature inhomogeneities. *Combustion and Flame*, 159(11):3323 – 3341, 2012. 2

[6] Z. Wang, J. X. Wang, S. J. Shuai, and Q. J. Ma. Effects of spark ignition and stratified charge on gasoline HCCI combustion with direct injection. *SAE Technical Paper (No. 2005-01-0137)*, 2005.

[7] D. Assanis, S. W. Wagnon, and M. S. Wooldridge. An experimental study of flame and autoignition interactions of iso-octane and air mixtures. *Combustion and Flame*, 162(4):1214 – 1224, 2015.

[8] G. Bansal and H. G. Im. Autoignition and front propagation in low temperature combustion engine environments. *Combustion and Flame*, 158(11):2105 – 2112, 2011. 3, 85

[9] A. Bhagatwala, R. Sankaran, S. L. Kokjohn, and J. H. Chen. Numerical investigation of spontaneous flame propagation under RCCI conditions. *Combustion and Flame*, 162(9):3412 – 3426, 2015. 16, 51, 85

[10] J. E. Dec and W. Hwang. Characterizing the development of thermal stratification in an HCCI engine using planar-imaging thermometry. *SAE Int. J. Engines*, 2:421–438, 04 2009.

[11] J. E. Dec, W. Hwang, and M. Sjöberg. An investigation of thermal stratification in HCCI engines using chemiluminescence imaging. *SAE Technical Paper (No. 2006-01-1518)*, 2006. 12

[12] S. L. Kokjohn, R. D. Reitz, D. A. Splitter, and M. Musculus. Investigation of fuel reactivity stratification for controlling PCI heat-release rates using high-speed chemiluminescence imaging and fuel tracer fluorescence. *SAE International Journal of Engines*, 5(2012-01-0375):248–269, 2012. 42, 50

[13] Q. Tang, H. Liu, M. Li, M. Yao, and Z. Li. Study on ignition and flame development in gasoline partially premixed combustion using multiple optical diagnostics. *Combustion and Flame*, 177:98–108, 2017. 2

[14] D. Siebers and B. Higgins. Flame lift-off on direct-injection diesel sprays under quiescent conditions. *SAE Technical Paper (No. 2001-01-0530)*, 2001. 2

[15] A. G. Merzhanov and B. I. Khaikin. Theory of combustion waves in homogeneous media. *Progress in Energy and Combustion Science*, 14(1):1 – 98, 1988. 2

[16] J. Pan, H. Wei, G. Shu, Z. Chen, and P. Zhao. The role of low temperature chemistry in combustion mode development under elevated pressures. *Combustion and Flame*, 174:179 – 193, 2016. 3, 103, 105

[17] Y. B. Zeldovich. Regime classification of an exothermic reaction with nonuniform initial conditions. *Combustion and Flame*, 39(2):211 – 214, 1980. 3

[18] X. J. Gu, D. R. Emerson, and D. Bradley. Modes of reaction front propagation from hot spots. *Combustion and Flame*, 133(1):63 – 74, 2003. 3, 14

[19] R. Sankaran, H. G. Im, E. R. Hawkes, and J. H. Chen. The effects of non-uniform temperature distribution on the ignition of a lean homogeneous hydrogen air mixture. *Proceedings of the Combustion Institute*, 30(1):875 – 882, 2005. 4

[20] S. Gupta, H. G. Im, and M. Valorani. Classification of ignition regimes in HCCI combustion using computational singular perturbation. *Proceedings of the Combustion Institute*, 33(2):2991 – 2999, 2011.

[21] A. Krisman, E. R. Hawkes, and J. H. Chen. The structure and propagation of laminar flames under autoignitive conditions. *Combustion and Flame*, 188:399–411, 2018. 3, 29, 30, 32, 33, 46, 49, 52, 53, 65, 103, 104, 105, 107

[22] L. Vervisch and T. Poinsot. Direct numerical simulation of non-premixed turbulent flames. *Annual Review of Fluid Mechanics*, 30(1):655–691, 1998. 4

[23] A. Bhagatwala, Z. Luo, H. Shen, J. A. Sutton, T. Lu, and J. H. Chen. Numerical and experimental investigation of turbulent DME jet flames. *Proceedings of the Combustion Institute*, 35(2):1157 – 1166, 2015. 4, 12, 25, 42, 50, 84, 91, 104

[24] C. A. Kennedy and M. H. Carpenter. Several new numerical methods for compressible shear-layer simulations. *Applied Numerical Mathematics*, 14(4):397 – 433, 1994. 4, 25, 42, 72, 104

[25] C. A. Kennedy, M. H. Carpenter, and R. M. Lewis. Low-storage, explicit Runge–Kutta schemes for the compressible Navier–Stokes equations. *Applied Numerical Mathematics*, 35(3):177–219, 2000. 4, 25, 42

[26] K. E. Niemeyer and C. J. Sung. Recent progress and challenges in exploiting graphics processors in computational fluid dynamics. *The Journal of Supercomputing*, 67(2):528–564, 2014. 6

[27] K. Spafford, J. Meredith, J. Vetter, J. H. Chen, R. Grout, and R. Sankaran. Accelerating S3D: a GPGPU case study. In *European Conference on Parallel Processing*, pages 122–131. Springer, 2009. 6

[28] Y. Shi, W. H. Green Jr., H. S. Wong, and O. O. Oluwole. Redesigning combustion modeling algorithms for the graphics processing unit (GPU): Chemical kinetic rate evaluation and ordinary differential equation integration. *Combustion and Flame*, 158(5):836–847, 2011. 6

[29] C. Stone and R. Davis. Techniques for solving stiff chemical kinetics on GPUs. In *51st AIAA Aerospace Sciences Meeting including the New Horizons Forum and Aerospace Exposition*, page 369, 2013. 6

[30] K. E. Niemeyer and C. J. Sung. Accelerating moderately stiff chemical kinetics in reactive-flow simulations using GPUs. *Journal of Computational Physics*, 256:854–871, 2014. 6

[31] F. E. H. Pérez, N. Mukhadiyev, X. Xu, A. Sow, B. J. Lee, R. Sankaran, and H. G. Im. Direct numerical simulations of reacting flows with detailed chemistry using many-core/GPU acceleration. *Computers and Fluids*, 173:73–79, 2018. 6, 42, 104, 150

[32] H. C. Edwards, D. Sunderland, V. Porter, C. Amsler, and S. Mish. Manycore performance-portability: Kokkos multidimensional array library. *Scientific Programming*, 20(2):89–114, 2012. 6

[33] H. C. Edwards, C. R. Trott, and D. Sunderland. Kokkos: Enabling manycore performance portability through polymorphic memory access patterns. *Journal of Parallel and Distributed Computing*, 74(12):3202–3216, 2014. 6

[34] J. B. Heywood. Automotive engines and fuels: A review of future options. *Progress in Energy and Combustion Science*, 7(3):155 – 184, 1981. 7

[35] C. Bae and J. Kim. Alternative fuels for internal combustion engines. *Proceedings of the Combustion Institute*, 36(3):3389 – 3413, 2017. 9

[36] C. Arcoumanis, C. Bae, R. Crookes, and E. Kinoshita. The potential of di-methyl ether (DME) as an alternative fuel for compression-ignition engines: A review. *Fuel*, 87(7):1014–1030, 2008. 9, 10

[37] J. Yu and C. Bae. Dimethyl ether (DME) spray characteristics in a common-rail fuel injection system. *Proceedings of the Institution of Mechanical Engineers, Part D: Journal of Automobile Engineering*, 217(12):1135–1144, 2003. 10

[38] S. H. Park and C. S. Lee. Combustion performance and emission reduction characteristics of automotive DME engine system. *Progress in Energy and Combustion Science*, 39(1):147–168, 2013. 10

[39] S. C. Sorenson and S. E. Mikkelsen. Performance and emissions of a 0.273 liter direct injection diesel engine fuelled with neat dimethyl ether. *SAE Technical Paper (No. 950064)*, 1995. 10

[40] S. H. Park and C. S. Lee. Applicability of dimethyl ether (DME) in a compression ignition engine as an alternative fuel. *Energy Conversion and Management*, 86:848–863, 2014. 10

[41] P. Kapus and H. Ofner. Development of fuel injection equipment and combustion system for DI diesels operated on dimethyl ether. *SAE Technical Paper (No. 950062)*, 1995. 10

[42] H. Yamada, K. Suzaki, H. Sakanashi, N. Choi, and A. Tezaki. Kinetic measurements in homogeneous charge compression of dimethyl ether: role of intermediate formaldehyde controlling chain branching in the low-temperature oxidation mechanism. *Combustion and Flame*, 140(1-2):24–33, 2005. 11, 55

[43] H. J. Curran, S. L. Fischer, and F. L. Dryer. The reaction kinetics of dimethyl ether. ii: Low-temperature oxidation in flow reactors. *International Journal of Chemical Kinetics*, 32(12):741–759, 2000. 11, 15

[44] Z. Zhao, M. Chaos, A. Kazakov, and F. L. Dryer. Thermal decomposition reaction and a comprehensive kinetic model of dimethyl ether. *International Journal of Chemical Kinetics*, 40(1):1–18, 2008. 11, 12, 23, 42, 55, 104

[45] H. Yamada, K. Suzaki, A. Tezaki, and Y. Goto. Transition from cool flame to thermal flame in compression ignition process. *Combustion and Flame*, 154(1-2):248–258, 2008. 11

[46] H. Oshibe, H. Nakamura, T. Tezuka, S. Hasegawa, and K. Maruta. Stabilized three-stage oxidation of DME/air mixture in a micro flow reactor with a controlled temperature profile. *Combustion and Flame*, 157(8):1572–1580, 2010. 11, 43, 109

[47] Z. Chen, X. Qin, Y. Ju, Z. Zhao, M. Chaos, and F. L. Dryer. High temperature ignition and combustion enhancement by dimethyl ether addition to methane–air mixtures. *Proceedings of the Combustion Institute*, 31(1):1215–1222, 2007. 12, 42

[48] H. Yu, E. Hu, Y. Cheng, X. Zhang, and Z. Huang. Experimental and numerical study of laminar premixed dimethyl ether/methane–air flame. *Fuel*, 136:37–45, 2014.

[49] P. Dai, Z. Chen, and S. Chen. Ignition of methane with hydrogen and dimethyl ether addition. *Fuel*, 118:1–8, 2014. 12, 42

[50] N. Dronniou and J. E. Dec. Investigating the development of thermal stratification from the near-wall regions to the bulk-gas in an HCCI engine with planar imaging thermometry. *SAE International Journal of Engines*, 5(3):1046–1074, 2012. 14

[51] A. Babajimopoulos, G. A. Lavoie, and D. N. Assanis. Modeling HCCI combustion with high levels of residual gas fraction-a comparison of two vva strategies. *SAE Technical paper (No. 2003-01-3220)*, 2003. 14

[52] B. Lawler, D. A. Splitter, J. P. Szybist, and B. Kaul. Thermally stratified compression ignition: A new advanced low temperature combustion mode with load flexibility. *Applied Energy*, 189:122 – 132, 2017. 14

[53] W. Sun, S. H. Won, X. Gou, and Y. Ju. Multi-scale modeling of dynamics and ignition to flame transitions of high pressure stratified n-heptane/toluene mixtures. *Proceedings of the Combustion Institute*, 35(1):1049 – 1056, 2015. 14

[54] Y. Ju, W. Sun, M. P. Burke, X. Gou, and Z. Chen. Multi-timescale modeling of ignition and flame regimes of n-heptane-air mixtures near spark assisted homogeneous charge compression ignition conditions. *Proceedings of the Combustion Institute*, 33(1):1245 – 1251, 2011. 14, 17, 18

[55] P. Dai, C. Qi, and Z. Chen. Effects of initial temperature on autoignition and detonation development in dimethyl ether/air mixtures with temperature gradient. *Proceedings of the Combustion Institute*, 36(3):3643–3650, 2017. 14

[56] S. Deng, P. Zhao, M. E. Mueller, and C. K. Law. Flame dynamics in oscillating flows under autoignitive conditions. *Combustion and Flame*, 168:75–82, 2016. 14, 31, 32, 40, 53, 55, 65

[57] J. E. Dec. Advanced compression-ignition engines - understanding the in-cylinder processes. *Proceedings of the Combustion Institute*, 32(2):2727 – 2742, 2009. 14

[58] D. A. Splitter, M. L. Wissink, T. L. Hendricks, J. B. Ghandhi, and R. D. Reitz. Comparison of rcci, HCCI, and cdc operation from low to full load. In *THIESEL 2012 conference on thermo-and fluid dynamic processes in direct injection engines*, 2012. 15

[59] R. D. Reitz and G. Duraisamy. Review of high efficiency and clean reactivity controlled compression ignition (RCCI) combustion in internal combustion engines. *Progress in Energy and Combustion Science*, 46:12–71, 2015. 16

[60] A. Paykani, A. H. Kakaee, P. Rahnama, and R. D. Reitz. Progress and recent trends in reactivity-controlled compression ignition engines. *International Journal of Engine Research*, 17(5):481–524, 2016. 16

[61] R. Sankaran, E. R. Hawkes, C. S. Yoo, and J. H. Chen. Response of flame thickness and propagation speed under intense turbulence in spatially developing lean premixed methane–air jet flames. *Combustion and Flame*, 162(9):3294–3306, 2015. 17, 115

[62] S. Lapointe, B. Savard, and G. Blanquart. Differential diffusion effects, distributed burning, and local extinctions in high karlovitz premixed flames. *Combustion and Flame*, 162(9):3341–3355, 2015. 17

[63] S. Lapointe and G. Blanquart. Fuel and chemistry effects in high karlovitz premixed turbulent flames. *Combustion and Flame*, 167:294–307, 2016.

[64] N. Fogla, F. Creta, and M. Matalon. The turbulent flame speed for low-to-moderate turbulence intensities: Hydrodynamic theory vs. experiments. *Combustion and Flame*, 175:155–169, 2017.

[65] T. Nilsson, H. Carlsson, R. Yu, and X. S. Bai. Structures of turbulent premixed flames in the high karlovitz number regime–dns analysis. *Fuel*, 216:627–638, 2018.

[66] J. Rosell, X. S. Bai, J. Sjoholm, B. Zhou, Z. Li, Z. Wang, P. Pettersson, Z. Li, M. Richter, and M. Alden. Multi-species plif study of the structures of turbulent premixed methane/air jet flames in the flamelet and thin-reaction zones regimes. *Combustion and Flame*, 182:324–338, 2017.

[67] T. M. Wabel, A. W. Skiba, J. E. Temme, and J. F. Driscoll. Measurements to determine the regimes of premixed flames in extreme turbulence. *Proceedings of the Combustion Institute*, 36(2):1809–1816, 2017.

[68] T. M. Wabel, A. W. Skiba, and J. F. Driscoll. Turbulent burning velocity measurements: Extended to extreme levels of turbulence. *Proceedings of the Combustion Institute*, 36(2):1801–1808, 2017. 17

[69] H. Kobayashi, T. Nakashima, T. Tamura, K. Maruta, and T. Niioka. Turbulence measurements and observations of turbulent premixed flames at elevated pressures up to 3.0 mpa. *Combustion and Flame*, 108(1-2):104–117, 1997. 17

[70] B. Savard, S. Lapointe, and Andrzej Teodorczyk. Numerical investigation of the effect of pressure on heat release rate in iso-octane premixed turbulent flames under conditions relevant to si engines. *Proceedings of the Combustion Institute*, 36(3):3543–3549, 2017. 17

[71] C. J. Rutland and A. Trouvé. Direct simulations of premixed turbulent flames with nonunity lewis numbers. *Combustion and Flame*, 94(1-2):41–57, 1993. 17

[72] M. J. Dunn and R. S. Barlow. Effects of preferential transport and strain in bluff body stabilized lean and rich premixed ch4/air flames. *Proceedings of the Combustion Institute*, 34(1):1411–1419, 2013. 17

[73] G. J. Smallwood, Ö. L. Gülder, D. R. Snelling, B. M. Deschamps, and I. Gökalp. Characterization of flame front surfaces in turbulent premixed methane/air combustion. *Combustion and Flame*, 101(4):461–470, 1995. 17

[74] Z. Wang, E. Motheau, and J. Abraham. Effects of equivalence ratio variations on turbulent flame speed in lean methane/air mixtures under lean-burn natural gas engine operating conditions. *Proceedings of the Combustion Institute*, 36(3):3423–3430, 2017. 17

[75] N. Peters. *Turbulent combustion*. Cambridge university press, 2000. 17

[76] M. P. B. Musculus, P. C. Miles, and L. M. Pickett. Conceptual models for partially premixed low-temperature diesel combustion. *Progress in Energy and Combustion Science*, 39(2-3):246–283, 2013. 17

[77] S. Desai, R. Sankaran, and H. G. Im. Unsteady deflagration speed of an auto-ignitive dimethyl-ether (DME)/air mixture at stratified conditions. *Proceedings of the Combustion Institute*, 37(4):4717 – 4727, 2019. 17, 22, 52, 55, 57, 85, 103, 105, 107

[78] S. H. Won, B. Windom, B. Jiang, and Y. Ju. The role of low temperature fuel chemistry on turbulent flame propagation. *Combustion and Flame*, 161(2):475–483, 2014. 17

[79] B. Windom, S. H. Won, C. B. Reuter, B. Jiang, Y. Ju, S. Hammack, T. Ombrello, and C. Carter. Study of ignition chemistry on turbulent premixed flames of n-heptane/air by using a reactor assisted turbulent slot burner. *Combustion and Flame*, 169:19–29, 2016. 17

[80] B. Savard, H. Wang, A. Teodorczyk, and E. R. Hawkes. Low-temperature chemistry in n-heptane/air premixed turbulent flames. *Combustion and Flame*, 196:71–84, 2018. 17, 120

[81] S. Deng, P. Zhao, M. E Mueller, and C. K. Law. Stabilization of laminar nonpremixed DME/air coflow flames at elevated temperatures and pressures. *Combustion and Flame*, 162(12):4471–4478, 2015. 18, 65

[82] A. Krisman, E. R. Hawkes, M. Talei, A. Bhagatwala, and J. H. Chen. Polybrachial structures in dimethyl ether edge-flames at negative temperature coefficient conditions. *Proceedings of the Combustion Institute*, 35(1):999–1006, 2015. 18

[83] R. Samtaney, D. I. Pullin, and B. Kosović. Direct numerical simulation of decaying compressible turbulence and shocklet statistics. *Physics of Fluids*, 13(5):1415–1430, 2001. 18

[84] X. D. Liu, S. Osher, and T. Chan. Weighted essentially non-oscillatory schemes. *Journal of Computational Physics*, 115(1):200–212, 1994. 18

[85] S. Pirozzoli. Numerical methods for high-speed flows. *Annual Review of Fluid Mechanics*, 43:163–194, 2011. 19

[86] S. Desai, R. Sankaran, and H. G. Im. Auto-ignitive deflagration speed of methane (CH_4) blended dimethyl-ether (DME)/air mixtures at stratified conditions. *Combustion and Flame*, 211:377 – 391, 2020. 22

[87] A. Bhagatwala, J. H. Chen, and T. Lu. Direct numerical simulations of HCCI/SACI with ethanol. *Combustion and Flame*, 161(7):1826–1841, 2014. 23, 85

[88] T. J. Poinsot and S. K. Lele. Boundary conditions for direct simulations of compressible viscous flows. *Journal of Computational Physics*, 101(1):104–129, 1992. 23, 25, 49, 85, 105

[89] C. S. Yoo and H. G. Im. Characteristic boundary conditions for simulations of compressible reacting flows with multi-dimensional, viscous and reaction effects. *Combustion Theory and Modelling*, 11:259–286, 2007. 23, 105

[90] P. G. Aleiferis, M. K. Behringer, and J. S. Malcolm. Integral length scales and time scales of turbulence in an optical spark-ignition engine. *Flow, Turbulence and Combustion*, 98(2):523–577, 2017. 26, 51, 105

[91] H. Zhang, E. R. Hawkes, J. H. Chen, and S. Kook. A numerical study of the autoignition of dimethyl ether with temperature inhomogeneities. *Proceedings of the Combustion Institute*, 34(1):803–812, 2013. 27

[92] S. O. Kim, M. B. Luong, J. H. Chen, and C. S. Yoo. A dns study of the ignition of lean PRF/air mixtures with temperature inhomogeneities under high pressure and intermediate temperature. *Combustion and Flame*, 162(3):717–726, 2015. 27

[93] R. L. Gordon, A. R. Masri, S. B. Pope, and G. M. Goldin. Transport budgets in turbulent lifted flames of methane autoigniting in a vitiated co-flow. *Combustion and Flame*, 151(3):495–511, 2007. 28, 107, 122

[94] M. B. Luong, R. Sankaran, G. H. Yu, S. H. Chung, and C. S. Yoo. On the effect of injection timing on the ignition of lean PRF/air/EGR mixtures under direct dual fuel stratification conditions. *Combustion and Flame*, 183:309–321, 2017. 28, 53, 85, 105

[95] R. Sankaran and H. G. Im. Dynamic flammability limits of methane/air premixed flames with mixture composition fluctuations. *Proceedings of the Combustion Institute*, 29(1):77–84, 2002. 31, 55

[96] T. Echekki and J. H. Chen. Analysis of the contribution of curvature to premixed flame propagation. *Combustion and Flame*, 118(1):308–311, 1999. 34, 59, 125

[97] D. E. Nieman, A. B. Dempsey, and R. D. Reitz. Heavy-duty RCCI operation using natural gas and diesel. *SAE International Journal of Engines*, 5(2012-01-0379):270–285, 2012. 42

[98] S. M. Sarathy, E. A. Tingas, E. F. Nasir, A. Detogni, Z. Wang, A. Farooq, and H. G. Im. Three-stage heat release in n-heptane auto-ignition. *Proceedings of the Combustion Institute*, 37(1):485–492, 2019. 44, 109

[99] J. B. Martz, H. Kwak, H. G. Im, G. A. Lavoie, and D. N. Assanis. Combustion regime of a reacting front propagating into an auto-igniting mixture. *Proceedings of the Combustion Institute*, 33(2):3001 – 3006, 2011. 44

[100] C. K. Law. *Combustion physics*. Cambridge University Press, 2010. 50, 53

[101] P. Habisreuther, F. C. C. Galeazzo, C. Prathap, and N. Zarzalis. Structure of laminar premixed flames of methane near the auto-ignition limit. *Combustion and Flame*, 160(12):2770–2782, 2013. 52

[102] V. V. Lissianski, V. M. Zamansky, and W. C. Gardiner. Combustion chemistry modeling. In *Gas-Phase Combustion Chemistry*, pages 1–123. Springer, 2000. 55

[103] M. P. Martín, E. M. Taylor, M. Wu, and V. G. Weirs. A bandwidth-optimized WENO scheme for the effective direct numerical simulation of compressible turbulence. *Journal of Computational Physics*, 220(1):270–289, 2006. 73, 81, 151, 153

[104] M. Castro, B. Costa, and W. S. Don. High order weighted essentially non-oscillatory WENO-Z schemes for hyperbolic conservation laws. *Journal of Computational Physics*, 230(5):1766–1792, 2011. 73, 81, 100, 153, 154

[105] O. San and K. Kara. Evaluation of Riemann flux solvers for WENO reconstruction schemes: Kelvin–Helmholtz instability. *Computers & Fluids*, 117:24–41, 2015. 74

[106] A. K. Henrick, T. D. Aslam, and J. M. Powers. Mapped weighted essentially non-oscillatory schemes: achieving optimal order near critical points. *Journal of Computational Physics*, 207(2):542–567, 2005. 75, 77, 81, 104

[107] G. S. Jiang and C. W. Shu. Efficient implementation of weighted ENO schemes. *Journal of Computational Physics*, 126(1):202–228, 1996. 75, 76, 79, 152

[108] A. K. Henrick, T. D. Aslam, and J. M. Powers. Simulations of pulsating one-dimensional detonations with true fifth order accuracy. *Journal of Computational Physics*, 213(1):311–329, 2006. 76, 77, 151

[109] G. A. Sod. A survey of several finite difference methods for systems of nonlinear hyperbolic conservation laws. *Journal of Computational Physics*, 27(1):1–31, 1978. 78

[110] T. Passot and A. Pouquet. Numerical simulation of compressible homogeneous flows in the turbulent regime. *Journal of Fluid Mechanics*, 181:441–466, 1987. 80, 105

[111] A. Sow, B. J. Lee, F. E. H. Pérez, and H. G. Im. Detonation onset in a thermally stratified constant volume reactor. *Proceedings of the Combustion Institute*, 37(3):3529–3536, 2019. 82, 118

[112] M. P. Burke, M. Chaos, Y. Ju, F. L. Dryer, and S. J. Klippenstein. Comprehensive H_2/O_2 kinetic model for high-pressure combustion. *International Journal of Chemical Kinetics*, 44(7):444–474, 2012. 82

[113] X. Ma, Z. Wang, C. Jiang, Y. Jiang, H. Xu, and J. Wang. An optical study of in-cylinder CH_2O and OH chemiluminescence in flame-induced reaction front propagation using high speed imaging. *Fuel*, 134(Supplement C):603 – 610, 2014. 84

[114] T. Urushihara, K. Yamaguchi, K. Yoshizawa, and T. Itoh. A study of a gasoline-fueled compression ignition engine - expansion of HCCI operation range using SI combustion as a trigger of compression ignition˜. *SAE transactions*, pages 419–425, 2005.

[115] D. L. Reuss, T. W. Kuo, G. Silvas, V. Natarajan, and V. Sick. Experimental metrics for identifying origins of combustion variability during spark-assisted compression ignition. *International Journal of Engine Research*, 9(5):409–434, 2008. 84

[116] P. Domingo and L. Vervisch. Triple flames and partially premixed combustion in autoignition of non-premixed turbulent mixtures. In *Symposium (International) on Combustion*, volume 26, pages 233–240. Elsevier, 1996. 85

[117] A. K. Agarwal, A. P. Singh, and R. K. Maurya. Evolution, challenges and path forward for low temperature combustion engines. *Progress in Energy and Combustion Science*, 61:1–56, 2017. 86

[118] G. M. Amdahl. Validity of the single processor approach to achieving large scale computing capabilities. In *Proceedings of the April 18-20, 1967, Spring Joint Computer Conference*, pages 483–485. ACM, 1967. 97

[119] K. N. C. Bray. Studies of the turbulent burning velocity. *Proceedings of the Royal Society of London A*, 431(1882):315–335, 1990. 103

[120] S. M. Candel and T. J. Poinsot. Flame stretch and the balance equation for the flame area. *Combustion Science and Technology*, 70(1-3):1–15, 1990. 103

[121] J. H. Chen, E. R. Hawkes, R. Sankaran, S. D. Mason, and H. G. Im. Direct numerical simulation of ignition front propagation in a constant volume with temperature inhomogeneities: I. fundamental analysis and diagnostics. *Combustion and Flame*, 145(1-2):128–144, 2006. 106

[122] Y. Wang and C. J. Rutland. Effects of temperature and equivalence ratio on the ignition of n-heptane fuel spray in turbulent flow. *Proceedings of the Combustion Institute*, 30(1):893–900, 2005. 107

[123] S. Zhang and C. J. Rutland. Premixed flame effects on turbulence and pressure-related terms. *Combustion and Flame*, 102(4):447 – 461, 1995. 117

[124] J. F. Driscoll and A. Gulati. Measurement of various terms in the turbulent kinetic energy balance within a flame and comparison with theory. *Combustion and Flame*, 72(2):131–152, 1988. 117

[125] Y. Zhang, H. El-Merhubi, B. Lefort, L. Le Moyne, H.J. Curran, and A. Kéromnès. Probing the low-temperature chemistry of ethanol via the addition of dimethyl ether. *Combustion and Flame*, 190:74–86, 2018. 132

[126] L. Vervisch, R. Hauguel, P. Domingo, and M. Rullaud. Three facets of turbulent combustion modelling: DNS of premixed v-flame, LES of lifted nonpremixed flame and RANS of jet-flame. *Journal of Turbulence*, 5(4):1–8, 2004. 132

[127] T. Echekki, A. R. Kerstein, T. D. Dreeben, and J. Y. Chen. 'One-dimensional turbulence' simulation of turbulent jet diffusion flames: model formulation and illustrative applications. *Combustion and Flame*, 125(3):1083 – 1105, 2001. 132

Appendices

A Governing equations

The DNS code KARFS [31] solves the fully compressible continuity, momentum, total energy, and species equations in conservative form with detailed chemistry for a mixture of ideal gases on structured, Cartesian grids

$$\frac{\partial \rho}{\partial t} = -\frac{\partial \left(\rho u_i\right)}{\partial x_i} \tag{1a}$$

$$\frac{\partial \left(\rho u_i\right)}{\partial t} = -\frac{\partial \left(\rho u_i u_j\right)}{\partial x_j} - \frac{\partial P}{\partial x_i} + \frac{\partial \tau_{ij}}{\partial x_j} \tag{1b}$$

$$\frac{\partial \left(\rho e_\mathrm{t}\right)}{\partial t} = -\frac{\partial \left(\rho e_\mathrm{t} u_j\right)}{\partial x_j} - \frac{\partial \left(P u_j\right)}{\partial x_j} + \frac{\partial \left(\tau_{ij} u_i\right)}{\partial x_j} - \frac{\partial q_j}{\partial x_j} \tag{1c}$$

$$\frac{\partial \left(\rho Y_k\right)}{\partial t} = -\frac{\partial \left(\rho Y_k u_j\right)}{\partial x_j} - \frac{\partial J_{k,j}}{\partial x_j} + \dot{\omega}_k \tag{1d}$$

where the Einstein summation convention is implied, ρ is the density, u_i is the Cartesian velocity component in the i^{th} coordinate direction ($i = 1, 2, 3$), P is the pressure, Y_k is the mass fraction of the k^{th} species and $\dot{\omega}_k$ is its reaction rate, τ_{ij} is the viscous stress tensor given by $\tau_{ij} = \mu(\frac{\partial u_i}{\partial x_j} + \frac{\partial u_j}{\partial x_i} - \frac{2}{3}\delta_{ij}\frac{\partial u_l}{\partial x_l})$, where μ is the molecular viscosity. The total specific energy is given by $e_\mathrm{t} = u_i u_i/2 + h - P/\rho$ and the heat flux vector is given by $q_i = -\alpha\frac{\partial T}{\partial x_i} + \sum_k h_k J_{k,i}$, with h, α, and T being the enthalpy, thermal conductivity and temperature, respectively. The species diffusive flux is computed through a mixture-averaged formulation based on Fick's law, $J_{k,i} = -\rho\mathcal{D}_k\frac{\partial Y_k}{\partial x_i} - \rho\mathcal{D}_k\frac{Y_k}{M_k}\frac{\partial M}{\partial x_i}$ where M_k is the species molecular weight, M is the mixture-averaged molecular weight and $\mathcal{D}_k$ is a mixture-averaged diffusion coefficient computed using Cantera [1]. Nitrogen is used as the bath gas, i.e. the diffusion flux of nitrogen is computed as negative of the sum of the diffusion fluxes for the other species in order to ensure that the net diffusion flux is zero.

B Other WENO schemes

Implementation details of several high order WENO schemes apart from the WENO7M scheme [108] in KARFS are presented below.

B.1 WENO8

The WENO8 scheme [103] is implemented in KARFS by defining a new WENO8 interpolator and replacing the WENO7M interpolator in Equations (4.6a) to (4.6d) as follows:

$$\left.\frac{\partial \hat{C}^+}{\partial x}\right|_{i+1/2} = \frac{\mathrm{WENO8}(C^+_{i-3}, C^+_{i-2}, C^+_{i-1}, C^+_i, C^+_{i+1}, C^+_{i+2}, C^+_{i+3}, C^+_{i+4})}{\Delta x} \tag{2a}$$

$$\left.\frac{\partial \hat{C}^+}{\partial x}\right|_{i-1/2} = \frac{\mathrm{WENO8}(C^+_{i-4}, C^+_{i-3}, C^+_{i-2}, C^+_{i-1}, C^+_i, C^+_{i+1}, C^+_{i+2}, C^+_{i+3})}{\Delta x} \tag{2b}$$

$$\left.\frac{\partial \hat{C}^-}{\partial x}\right|_{i+1/2} = \frac{\mathrm{WENO8}(C^-_{i+4}, C^-_{i+3}, C^-_{i+2}, C^-_{i+1}, C^-_i, C^-_{i-1}, C^-_{i-2}, C^+_{i-3})}{\Delta x} \tag{2c}$$

$$\left.\frac{\partial \hat{C}^-}{\partial x}\right|_{i-1/2} = \frac{\mathrm{WENO8}(C^-_{i+3}, C^-_{i+2}, C^-_{i+1}, C^-_i, C^-_{i-1}, C^-_{i-2}, C^-_{i-3}, C^+_{i-4})}{\Delta x} \tag{2d}$$

The functional form of the WENO8 interpolator in equation (2a) is given by

$$\mathrm{WENO8}(C^+_{i-3}, C^+_{i-2}, C^+_{i-1}, C^+_i, C^+_{i+1}, C^+_{i+2}, C^+_{i+3}, C^+_{i+4}) = \sum_{k=0}^{4} w_k a_k \,, \tag{3}$$

where w_k are the WENO8 weights and the component stencils a_k are

$$a_0 = \frac{1}{24}(-6C^+_{i-3} + 26C^+_{i-2} - 46C^+_{i-1} + 50C^+_i) \,, \tag{4a}$$

$$a_1 = \frac{1}{24}(2C^+_{i-2} - 10C^+_{i-1} + 26C^+_i + 6C^+_{i+1}) \,, \tag{4b}$$

$$a_2 = \frac{1}{24}(-2C^+_{i-1} + 14C^+_i + 14C^+_{i+1} - 2C^+_{i+2})\,, \tag{4c}$$
$$a_3 = \frac{1}{24}(6C^+_i + 26C^+_{i+1} - 10C^+_{i+2} + 2C^+_{i+3})\,, \tag{4d}$$
$$a_4 = \frac{1}{24}(50C^+_{i-1} - 46C^+_i + 26C^+_{i+1} - 6C^+_{i+2})\,. \tag{4e}$$

The weights w_k are approximated following the procedure described in [107] as

$$w^*_k = \frac{\gamma_k}{\sum_{i=0}^{4}\gamma_i},\ \text{where}\ \gamma_k = \frac{\bar{w}_k}{(\epsilon + \beta_k)^p}\,. \tag{5}$$

The ideal weights (used to construct nonlinear weights and subsequently an essentially non-oscillatory interpolant), $\bar{w}_k$, are constants given by

$$\bar{w}_0 = 0.040195483373,\ \bar{w}_1 = 0.249380000671,\ \bar{w}_2 = 0.480268625626,$$
$$\bar{w}_3 = 0.200977547673,\ \bar{w}_4 = 0.029178342658\,, \tag{6}$$

and the smoothness indicators β_k are defined as

$$\begin{aligned}
\beta_0 =& \frac{1}{36}(-2C^+_{i-3} + 9C^+_{i-2} - 18C^+_{i-1} + 11C^+_i)^2 \\
&+ \frac{13}{12}(-1C^+_{i-3} + 4C^+_{i-2} - 5C^+_{i-1} + 2C^+_i)^2 \\
&+ \frac{781}{720}(-C^+_{i-3} + 3C^+_{i-2} - 3C^+_{i-1} + C^+_i)^2\,, \qquad (7a)\\
\beta_1 =& \frac{1}{36}(C^+_{i-2} - 6C^+_{i-1} + 3C^+_i + 2C^+_{i+1})^2 \\
&+ \frac{13}{12}(C^+_{i-1} - 2C^+_i + C^+_{i+1})^2 \\
&+ \frac{781}{720}(-C^+_{i-2} + 3C^+_{i-1} - 3C^+_i + C^+_{i+1})^2\,, \qquad (7b)\\
\beta_2 =& \frac{1}{36}(-2C^+_{i-1} - 3C^+_i + 6C^+_{i+1} - C^+_{i+2})^2 \\
&+ \frac{13}{12}(C^+_{i-1} - 2C^+_i + C^+_{i+1})^2 \\
&+ \frac{781}{720}(-C^+_{i-1} + 3C^+_i - 3C^+_{i+1} + C^+_{i+2})^2\,, \qquad (7c)\\
\beta_3 =& \frac{1}{36}(-11C^+_i + 18C^+_{i+1} - 9C^+_{i+2} + 2C^+_{i+3})^2 \\
&+ \frac{13}{12}(2C^+_i - 5C^+_{i+1} + 4C^+_{i+2} - C^+_{i+3})^2
\end{aligned}$$

$$+\frac{781}{720}(-C_i^+ + 3C_{i+1}^+ - 3C_{i+2}^+ + C_{i+3}^+)^2\,, \tag{7d}$$

$$\begin{aligned}\beta_4 =& \frac{1}{36}(-26C_{i+1}^+ + 57C_{i+2}^+ - 42C_{i+3}^+ + 11C_{i+4}^+)^2 \\ &+\frac{13}{12}(3C_{i+1}^+ - 8C_{i+2}^+ + 7C_{i+3}^+ - 2C_{i+4}^+)^2 \\ &+\frac{781}{720}(-C_{i+1}^+ + 3C_{i+2}^+ - 3C_{i+3}^+ + C_{i+4}^+)^2\,.\end{aligned} \tag{7e}$$

The smoothness indicator β_4 is further constrained to satisfy

$$\beta_4 = \max_{0\leq k\leq 4}(\beta_k) \tag{8}$$

In Equation 5, $\epsilon = 10^{-10}$ is a small number that prevents division by zero errors and p=1 as suggested in [103].

B.2 WENO-Z

The WENO-Z scheme [104] is implemented in KARFS by defining a new WENO7Z interpolator and replacing the WENO7M interpolator in Equations (4.6a) to (4.6d) as follows:

$$\frac{\partial \hat{C}^+}{\partial x}\Big|_{i+1/2} = \frac{\text{WENO7Z}(C_{i-3}^+, C_{i-2}^+, C_{i-1}^+, C_i^+, C_{i+1}^+, C_{i+2}^+, C_{i+3}^+)}{\Delta x} \tag{9a}$$

$$\frac{\partial \hat{C}^+}{\partial x}\Big|_{i-1/2} = \frac{\text{WENO7Z}(C_{i-4}^+, C_{i-3}^+, C_{i-2}^+, C_{i-1}^+, C_i^+, C_{i+1}^+, C_{i+2}^+)}{\Delta x} \tag{9b}$$

$$\frac{\partial \hat{C}^-}{\partial x}\Big|_{i+1/2} = \frac{\text{WENO7Z}(C_{i+4}^-, C_{i+3}^-, C_{i+2}^-, C_{i+1}^-, C_i^-, C_{i-1}^-, C_{i-2}^-)}{\Delta x} \tag{9c}$$

$$\frac{\partial \hat{C}^-}{\partial x}\Big|_{i-1/2} = \frac{\text{WENO7Z}(C_{i+3}^-, C_{i+2}^-, C_{i+1}^-, C_i^-, C_{i-1}^-, C_{i-2}^-, C_{i-3}^-)}{\Delta x} \tag{9d}$$

The functional form of the WENO7Z interpolator in equation (9a) is given by

$$\text{WENO7Z}(C^+_{i-3}, C^+_{i-2}, C^+_{i-1}, C^+_i, C^+_{i+1}, C^+_{i+2}, C^+_{i+3}) = \sum_{k=0}^{3} w_k a_k \,, \tag{10}$$

where w_k are the WENO7Z weights and the component stencils a_k are

$$a_0 = \frac{1}{24}(-6C^+_{i-3} + 26C^+_{i-2} - 46C^+_{i-1} + 50C^+_i) \,, \tag{11a}$$
$$a_1 = \frac{1}{24}(2C^+_{i-2} - 10C^+_{i-1} + 26C^+_i + 6C^+_{i+1}) \,, \tag{11b}$$
$$a_2 = \frac{1}{24}(-2C^+_{i-1} + 14C^+_i + 14C^+_{i+1} - 2C^+_{i+2}) \,, \tag{11c}$$
$$a_3 = \frac{1}{24}(6C^+_i + 26C^+_{i+1} - 10C^+_{i+2} + 2C^+_{i+3}) \,. \tag{11d}$$

The weights w_k are approximated following the procedure described in [104] as

$$w^*_k = \frac{\gamma_k}{\sum_{i=0}^{3} \gamma_i}, \text{ where } \gamma_k = \bar{w}_k[1 + (\frac{\tau}{\epsilon + \beta_k})^p] \text{ and } k = 0, 1, 2, 3 \,. \tag{12}$$

The ideal weights (used to construct nonlinear weights and subsequently an essentially non-oscillatory interpolant), $\bar{w}_k$, are constants given by

$$\bar{w}_0 = \frac{1}{35}, \ \bar{w}_1 = \frac{12}{35}, \ \bar{w}_2 = \frac{18}{35}, \ \bar{w}_3 = \frac{4}{35} \,, \tag{13}$$

and the smoothness indicators β_k are defined as

$$\begin{aligned}
\beta_0 =& \frac{1}{36}(-2C^+_{i-3} + 9C^+_{i-2} - 18C^+_{i-1} + 11C^+_i)^2 \\
&+ \frac{13}{12}(-1C^+_{i-3} + 4C^+_{i-2} - 5C^+_{i-1} + 2C^+_i)^2 \\
&+ \frac{781}{720}(-C^+_{i-3} + 3C^+_{i-2} - 3C^+_{i-1} + C^+_i)^2 \,,
\end{aligned} \tag{14a}$$

$$\begin{aligned}
\beta_1 =& \frac{1}{36}(C^+_{i-2} - 6C^+_{i-1} + 3C^+_i + 2C^+_{i+1})^2 \\
&+ \frac{13}{12}(C^+_{i-1} - 2C^+_i + C^+_{i+1})^2 \\
&+ \frac{781}{720}(-C^+_{i-2} + 3C^+_{i-1} - 3C^+_i + C^+_{i+1})^2 \,,
\end{aligned} \tag{14b}$$

$$\begin{aligned}\beta_2 =& \frac{1}{36}(-2C_{i-1}^{+} - 3C_i^{+} + 6C_{i+1}^{+} - C_{i+2}^{+})^2 \\ &+ \frac{13}{12}(C_{i-1}^{+} - 2C_i^{+} + C_{i+1}^{+})^2 \\ &+ \frac{781}{720}(-C_{i-1}^{+} + 3C_i^{+} - 3C_{i+1}^{+} + C_{i+2}^{+})^2\,, \end{aligned} \tag{14c}$$

$$\begin{aligned}\beta_3 =& \frac{1}{36}(-11C_i^{+} + 18C_{i+1}^{+} - 9C_{i+2}^{+} + 2C_{i+3}^{+})^2 \\ &+ \frac{13}{12}(2C_i^{+} - 5C_{i+1}^{+} + 4C_{i+2}^{+} - C_{i+3}^{+})^2 \\ &+ \frac{781}{720}(-C_i^{+} + 3C_{i+1}^{+} - 3C_{i+2}^{+} + C_{i+3}^{+})^2\,. \end{aligned} \tag{14d}$$

τ in equation 12 is defined as:

$$\tau = |-\beta_0 - 3\beta_1 + 3\beta_2 + \beta_3| \tag{15}$$

In Equation 12, $\epsilon = 10^{-40}$ is a small number that prevents division by zero errors and p may be varied to increase or decrease the WENO7Z adaptation sensitivity.

Vita

Swapnil Desai was born in Ahmedabad, Gujarat, India to the parents of Vasantmala and Sanjay Desai. He attended the Vidya Kunj school in Navsari, Gujarat, India for his primary education and continued to the St. Joseph's English Teaching High School in Valsad, Gujarat, India. After graduation, he headed to Birla Vishvakarma Mahavidyalaya, Vallabh Vidyanagar, Gujarat to pursue a Bachelors degree in Mechanical Engineering. Upon his graduation in Summer'11, he was recruited by Larsen & Toubro Ltd. He worked as an executive engineer working in the Supply Chain Management group at their boiler manufacturing plant in Hazira, Gujarat, India for a couple of years. In Fall'13, he moved to Los Angeles, CA to pursue his Masters in Mechanical Engineering at the University of Southern California. He was first introduced to the field of energy and combustion science here. He completed a six month directed research project with Dr. Paul Ronney, which was an exciting and challenging experience and pushed him into continuing his education. After completing his masters in Summer'15, he accepted the Energy Science and Engineering Fellowship at The University of Tennessee, Knoxville in the Bredesen Center. He joined Dr. Ramanan Sankaran's group at the Oak Ridge National Laboratory (ORNL) in Spring'16 where has been investigating multi-stage, mixed-modes of turbulent reacting flows using Direct Numerical Simulations (DNS) and High Performance Computing (HPC). He is currently a Ph.D. Candidate at the Bredesen Center, University of Tennessee. His Ph.D. work focuses on development, application and optimization of massively parallel, performance portable code for large scale simulations of turbulent reacting flows. His research interests include high performance computing, high-order numerical techniques for turbulent reacting flows and physics-based, data-driven modeling of multi-scale, multi-physics systems.